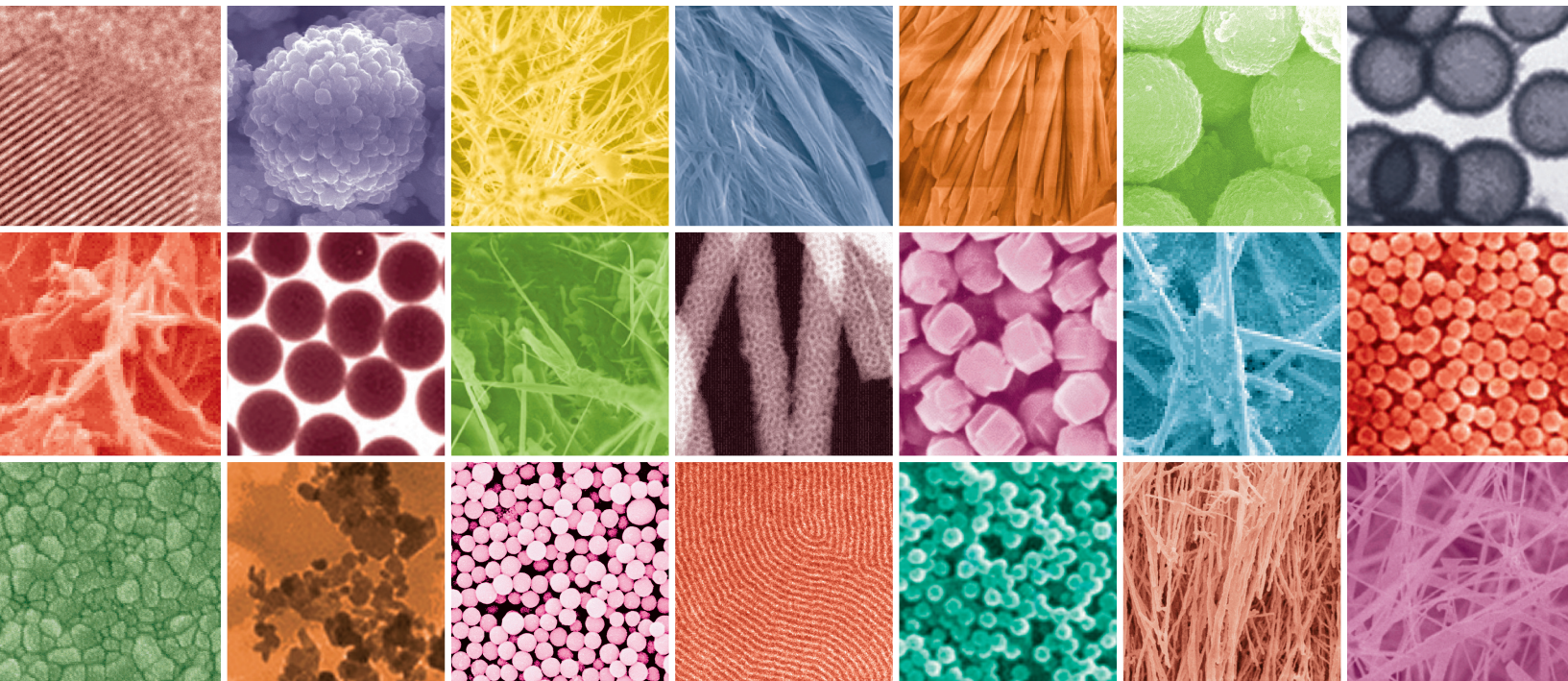


# Nanostructured Materials for Electronics and Photonics

Guest Editors: M. Reza Bayati, Sudhakar Nori, Naeimeh Naseri,  
and Yogendra Mishra





---

# **Nanostructured Materials for Electronics and Photonics**

Journal of Nanomaterials

---

## **Nanostructured Materials for Electronics and Photonics**

Guest Editors: M. Reza Bayati, Sudhakar Nori, Naeimeh Naseri,  
and Yogendra Mishra



---

Copyright © 2014 Hindawi Publishing Corporation. All rights reserved.

This is a special issue published in "Journal of Nanomaterials." All articles are open access articles distributed under the Creative Commons Attribution License, which permits unrestricted use, distribution, and reproduction in any medium, provided the original work is properly cited.

## Editorial Board

Katerina E. Aifantis, USA  
Nageh K. Allam, USA  
Margarida Amaral, Portugal  
Xuedong Bai, China  
Lavinia Balan, France  
Enrico Bergamaschi, Italy  
Theodorian Borca-Tasciuc, USA  
C. Jeffrey Brinker, USA  
Christian Brosseau, France  
Xuebo Cao, China  
Shafiq Chowdhury, USA  
Kwang-Leong Choy, UK  
Cui ChunXiang, China  
Miguel A. Correa-Duarte, Spain  
Shadi A. Dayeh, USA  
Ali Eftekhari, USA  
Claude Estournés, France  
Alan Fuchs, USA  
Lian Gao, China  
Russell E. Gorga, USA  
Hongchen Chen Gu, China  
Mustafa O. Guler, Turkey  
John Z. Guo, USA  
Smrati Gupta, Germany  
Michael Harris, USA  
Zhongkui Hong, China  
Michael Z. Hu, USA  
David Hui, USA  
Y.-K. Jeong, Republic of Korea  
Sheng-Rui Jian, Taiwan  
Wanqin Jin, China  
Rakesh K. Joshi, UK  
Zhenhui Kang, China  
Fathallah Karimzadeh, Iran  
Alireza Khataee, Iran

Do K. Kim, Korea  
Alan K. T. Lau, Hong Kong  
Burtrand Lee, USA  
Jun Li, Singapore  
Benxia Li, China  
Xing-Jie Liang, China  
Shijun Liao, China  
Gong-Ru Lin, Taiwan  
Tianxi Liu, China  
Jun Liu, USA  
Songwei Lu, USA  
Daniel Lu, China  
Jue Lu, USA  
Ed Ma, USA  
Gaurav Mago, USA  
Santanu K. Maiti, India  
Sanjay R. Mathur, Germany  
Vikas Mittal, UAE  
Weihai Ni, Germany  
Sherine Obare, USA  
Atsuto Okamoto, Japan  
Abdelwahab Omri, Canada  
Edward A. Payzant, USA  
Kui-Qing Peng, China  
Anukorn Phuruangrat, Thailand  
Mahendra Rai, India  
Suprakas Sinha Ray, South Africa  
Ugur Serincan, Turkey  
Huaiyu Shao, Japan  
Donglu Shi, USA  
Vladimir Sivakov, Germany  
Marinella Striccoli, Italy  
Bohua Sun, South Africa  
Saikat Talapatra, USA  
Nairong Tao, China

Titipun Thongtem, Thailand  
Somchai Thongtem, Thailand  
Alexander Tolmachev, Ukraine  
Valeri P. Tolstoy, Russia  
Tsung-Yen Tsai, Taiwan  
Takuya Tsuzuki, Australia  
Raquel Verdejo, Spain  
Mat U. Wahit, Malaysia  
Zhenbo Wang, China  
Ruiping Wang, Canada  
Shiren Wang, USA  
Cheng Wang, China  
Yong Wang, USA  
Jinquan Wei, China  
Ching-Ping Wong, Hong Kong  
Xingcai Wu, China  
Guodong Xia, Hong Kong  
Ping Xiao, UK  
Zhi Li Xiao, USA  
Yangchuan Xing, USA  
Shuangxi Xing, China  
Nanping Xu, China  
Doron Yadlovker, Israel  
Yingkui Yang, China  
Khaled Youssef, USA  
Kui Yu, Canada  
William W. Yu, USA  
Haibo Zeng, China  
Tianyou Zhai, China  
Renyun Zhang, Sweden  
Bin Zhang, China  
Yanbao Zhao, China  
Lianxi Zheng, Singapore  
Chunyi Zhi, Hong Kong

## Contents

**Nanostructured Materials for Electronics and Photonics**, R. Bayati, Y. K. Mishra, N. Naseri, and S. Nori  
Volume 2014, Article ID 725764, 2 pages

**Nonlinear Optical Properties of a MMA-Silica Nanohybrid Material Doped with Rhodamine 6G**,  
J. Lima-Gutiérrez, R. Palomino-Merino, M. L. Arroyo Carrasco, E. Rubio-Rosas, and V. M. Castaño  
Volume 2013, Article ID 374185, 5 pages

**Influences of InGaP Conical Frustum Nanostructures on the Characteristics of GaAs Solar Cells**,  
Nguyen Dinh Lam, Youngjo Kim, Kangho Kim, and Jaejin Lee  
Volume 2013, Article ID 785359, 6 pages

**Hydrogenic-Donor Impurity Binding Energy Dependence of the Electric Field in GaAs/Al<sub>x</sub>Ga<sub>1-x</sub>As  
Quantum Rings**, Guangxin Wang, Xiuzhi Duan, and Wei Chen  
Volume 2013, Article ID 240563, 7 pages

**Light Output Enhancement of InGaN/GaN Light-Emitting Diodes with Contrasting Indium Tin-Oxide  
Nanopatterned Structures**, Sang Hyun Jung, Keun Man Song, Young Su Choi, Hyeong-Ho Park,  
Hyun-Beom Shin, Ho Kwan Kang, and Jaejin Lee  
Volume 2013, Article ID 832170, 6 pages

**Low-Temperature Rapid Fabrication of ZnO Nanowire UV Sensor Array by Laser-Induced Local  
Hydrothermal Growth**, Sukjoon Hong, Junyeob Yeo, Wanit Manorotkul, Gunho Kim, Jinhyeong Kwon,  
Kunsik An, and Seung Hwan Ko  
Volume 2013, Article ID 246328, 7 pages

**Simulation of an Improved Design for n-Electrode with Holes for Thin-GaN Light-Emitting Diodes**,  
Farn-Shiun Hwu  
Volume 2013, Article ID 805361, 6 pages

**InGaAs Quantum Dots on Cross-Hatch Patterns as a Host for Diluted Magnetic Semiconductor  
Medium**, Teeravat Limwongse, Supachok Thainoi, Somsak Panyakeow, and Songphol Kanjanachuchai  
Volume 2013, Article ID 791782, 5 pages

**Nanocrystallization of Coarse Primary Phases in Al- and Mg-Based Alloys Induced by HCPEB  
Treatment**, Gao Bo, He Jidong, Tu Ganfeng, and Hu Liang  
Volume 2013, Article ID 815384, 6 pages

## Editorial

# Nanostructured Materials for Electronics and Photonics

**R. Bayati,<sup>1</sup> Y. K. Mishra,<sup>2</sup> N. Naseri,<sup>3</sup> and S. Nori<sup>4</sup>**

<sup>1</sup> Intel Corporation, IMO-SC, Santa Clara, CA 95054, USA

<sup>2</sup> Functional Nanomaterials, Institute for Materials Science, University of Kiel, 24143 Kiel, Germany

<sup>3</sup> Department of Physics, Sharif University of Technology, Tehran 11155-9161, Iran

<sup>4</sup> Department of Materials Science and Engineering, North Carolina State University, Raleigh, NC 27695, USA

Correspondence should be addressed to R. Bayati; [mbayati@ncsu.edu](mailto:mbayati@ncsu.edu)

Received 23 February 2014; Accepted 23 February 2014; Published 2 April 2014

Copyright © 2014 R. Bayati et al. This is an open access article distributed under the Creative Commons Attribution License, which permits unrestricted use, distribution, and reproduction in any medium, provided the original work is properly cited.

This special issue addresses both experimental and theoretical research works in the areas of nanoscale electronic, optoelectronic, and magneto-optical materials. It aims to facilitate the dissemination of interdisciplinary research results in the interrelated and rapidly converging fields of nanoelectronics and photonics. The main focus of this issue is placed on enhancing the performance of electronic devices using nanoscience and nanotechnology. The following aspects were considered as particular interests for this special issue:

- (i) electronic, optical, and magneto-optical properties of semiconductor oxides and inorganic, organic, and hybrid nanostructures,
- (ii) electronic applications of superlattices, quantum structures, and other nanostructures,
- (iii) optoelectronic and photonic applications of novel materials and nanostructures,
- (iv) oxide based nanoelectronic circuits and device integration,
- (v) molecular electronics,
- (vi) nanobioelectronics,
- (vii) nanofabrication, processing, and characterization techniques,
- (viii) thin film epitaxy of oxides and nitrides.

In the paper entitled “*Nonlinear optical properties of a MMA-silica nanohybrid material doped with Rhodamine 6G,*” a simple and inexpensive optically nonlinear nanohybrid

material is developed, based on a TEOS:MMA nanoporous matrix. The potential applications for this material include lasers, photochromic coatings, and photoluminescent materials for organic devices and biomedical imaging. Nanoparticles of the hybrid material doped with an organic dye show optical nonlinear response due to the dopant. Optical response control depends on the thin film thickness or on the amount of dopant. However, the absorbance and PL spectra taken on the TEOS:MMA hybrid matrix after doping was essentially unaltered, since the organic dopants are transparent over the visible spectral region.

In the paper entitled “*Influences of InGaP conical frustum nanostructures on the characteristics of GaAs solar cells,*” InGaP conical frustum nanostructures are fabricated on top of the GaAs solar cells and the optical and photovoltaic characteristics of the conical frustum nanostructured solar cells are studied. The most striking finding in this research work is that an increase of 15.2% in the conversion efficiency is achieved at the optimal geometry with a 100 nm height and 300 nm top diameter of the InGaP conical frustum nanostructure. The improvements are attributed to the gradual change in the refractive index, resulting in the Fresnel reflection suppression and light scattering effect by the InGaP conical frustum nanostructures.

The fabrication of InAs quantum dots (QDs) on InGaAs/GaAs is addressed in the paper entitled “*InGaAs quantum dots on cross-hatch patterns as a host for diluted magnetic semiconductor medium.*” In this research publication, the authors have demonstrated clearly how to grow InAs

QDs on InGaAs/GaAs using molecular beam epitaxy (MBE). The results are important due to the fact that the lattice-mismatched heteroepitaxy can be used to form laterally aligned, high-density semiconducting host in a single growth run without any use of lithography or etching. Lattice-mismatched epitaxy results in the formation of quantum dots (QDs), cross-hatch patterns (CHPs), stripes, and smooth films in decreasing order of misfit. For low-misfit InGaAs/GaAs, the dislocation lines making up the CHPs are widely spaced, resulting in stripes or cross-hatch patterns. For intermediate-misfit InGaAs/GaAs, surface CHPs are characterized by narrowly spaced dislocation lines along the two orthogonal directions with a different line density. The unidirectionally aligned QDs result in QD chains with electronic and optical coupling between dots while the bidirectionally aligned ones result in QD matrices. With appropriate alloying of a transition element and careful control of average dislocation spacings, these QD matrices can exhibit spin coupling and may serve as a high-density DMS medium/read heads. Such magnetic regions have the ultimate capability to store one bit of information each.

In the paper entitled “*Hydrogenic-donor impurity binding energy dependence of the electric field in GaAs/Al<sub>x</sub>Ga<sub>1-x</sub>As quantum rings*,” authors report a variational method with two-parameter trial wave function and the effective mass approximation for calculation of the binding energy of a donor impurity in GaAs/Al<sub>x</sub>Ga<sub>1-x</sub>As cylindrical quantum ring (QR) subjected to an external field. The authors have clarified that donor impurity binding energy is highly dependent on the QR structure parameters (radial thickness and height), impurity position, and external electric field. Based on their accurate investigations, the binding energy increases in a manner as the QR parameters (radial thickness and height) decrease until a maximum value for a central impurity and then begins to drop quickly. The applied electric field can significantly modify the spread of electronic wave function in the QR and shift electronic wave function from the donor position and then leads to binding energy changes. In addition, they demonstrated the results for the binding energies of a hydrogenic donor impurity as functions of the impurity position and applied electric field.

In the research article entitled “*Light output enhancement of InGaN/GaN light-emitting diodes with contrasting indium tin-oxide nanopatterned structures*,” various nanopatterns on the transparent conducting indium tin-oxide (ITO) layer to enhance the light extraction efficiency of the InGaN/GaN light-emitting diodes (LEDs) are fabricated and a structure-property correlation is established. Triangular, square, and circular nanohole patterns with the square and hexagonal lattices are fabricated on the ITO layer by an electron beam lithography and inductively coupled plasma dry etching processes. They found the circular hole pattern with a hexagonal geometry as the most effective among the studied structures. Light output intensity measurements resulted in that the circular hole nanopatterned ITO LEDs with a hexagonal lattice show up to 35.6% enhancement of output intensity compared to the sample without nanopatterns.

Subsequently, the paper entitled “*Low-temperature rapid fabrication of ZnO nanowire UV sensor array by laser-induced local hydrothermal growth*” focuses on ZnO nanowire based UV sensor synthesized by laser-induced hydrothermal growth of ZnO nanowire. In this regard, it is shown that, by inducing a localized temperature rise using focused laser, ZnO nanowire array at ~15 μm size that consists of individual nanowires with ~8 μm length and 200 ~ 400 nm diameter can be fabricated on gold electrode within 30 min at the desired position. The laser-induced growth process is consecutively applied on two different points to bridge the micron gap between the electrodes. The resultant photoconductive ZnO NW interconnections display 2 ~ 3 orders increase in the current upon the UV exposure at a fixed voltage bias. It is also confirmed that the amount of photocurrent can be easily adjusted by changing the number of ZnO NW array junctions. The device exhibits clear response to the repeated UV illumination, suggesting that this process can be usefully applied for the facile fabrication of low-cost UV sensor array.

In the paper entitled “*Simulation of an improved design for n-electrode with holes for thin-GaN light-emitting diodes*,” a novel design for n-electrode with holes to be applied in thin-GaN light-emitting diodes (LEDs) is discussed. Based on their deep investigations on the influence of the n-electrode with holes on the thermal and electrical characteristics of a thin-GaN LED chip, the variations in current density and temperature distributions in the active layer of n-electrodes both with and without holes are very tiny. The percentages of light output from these holes are 29.8% and 38.5% for cases with 5 μm holes and 10 μm holes, respectively; the side length of the n-electrode (L) is 200 μm. Furthermore, the percentage increases with the size of the n-electrode. They demonstrated that the light output can be increased 2.45 times using the n-electrode with holes design. The wall-plug efficiency (WPE) can also be improved from 2.3% to 5.7% while the most appropriate n-electrode and hole sizes are determined by WPE analysis.

In the last paper entitled “*Nanocrystallization of coarse primary phases in Al- and Mg-based alloys induced by HCPEB treatment*,” the authors report a phenomenon associated with high-current pulsed electron beam (HCPEB) treatment: surface nanocrystallization of coarse primary phase in hypereutectic Al17.5Si and quasicrystal alloys after multiple pulses of HCPEB irradiation. They stated that the HCPEB treatment induces superfast heating and diffusion of alloying elements and heterogeneous nucleation in a melting solution, followed by rapid solidification and cooling of the material surfaces. Consequently, nanostructured surface layers can be achieved easily. Nano-Si phase and nanoquasicrystal phase formation on the modified surface layer of hypereutectic Al17.5Si alloy and quasicrystal alloy (Mg<sub>37</sub>Zn<sub>60</sub>Y<sub>3</sub>) show a potential for surface nanocrystallization of materials with enhanced properties by HCPEB treatment.

R. Bayati  
Y. K. Mishra  
N. Naseri  
S. Nori

## Research Article

# Nonlinear Optical Properties of a MMA-Silica Nanohybrid Material Doped with Rhodamine 6G

**J. Lima-Gutiérrez,<sup>1,2,3</sup> R. Palomino-Merino,<sup>1,2</sup> M. L. Arroyo Carrasco,<sup>1,2</sup>  
E. Rubio-Rosas,<sup>2,4</sup> and V. M. Castaño<sup>5</sup>**

<sup>1</sup> *Facultad de Ciencias Físico Matemáticas, Avenida San Claudio y 18 Sur, Colonia San Manuel, 72570 Puebla, PUE, Mexico*

<sup>2</sup> *Benemérita Universidad Autónoma de Puebla Ciudad Universitaria, Colonia San Manuel, 72570 Puebla, PUE, Mexico*

<sup>3</sup> *Departamento de Ciencias e Ingenierías, Universidad Iberoamericana Puebla, Boulevard del Niño Poblano No. 2901, Unidad Territorial Atlixcáyotl, 72197 Puebla, PUE, Mexico*

<sup>4</sup> *Centro Universitario de Vinculación y Transferencia de Tecnología, Prolongación de la 24 Sur y Avenida San Claudio, Ciudad Universitaria, Colonia San Manuel, 72570 Puebla, PUE, Mexico*

<sup>5</sup> *Centro de Física Aplicada y Tecnología Avanzada, UNAM, A.P. 1-1010, 76000 Querétaro, QRO, Mexico*

Correspondence should be addressed to V. M. Castaño; [meneses@unam.mx](mailto:meneses@unam.mx)

Received 4 June 2013; Accepted 28 November 2013

Academic Editor: Sudhakar Nori

Copyright © 2013 J. Lima-Gutiérrez et al. This is an open access article distributed under the Creative Commons Attribution License, which permits unrestricted use, distribution, and reproduction in any medium, provided the original work is properly cited.

A novel nanohybrid material based on MMA-Silica has been synthesized with an organic dye dopant (R6G) to tailor the optical properties. This novel material can be used on several devices such as active laser media for an organic solid state laser, OLEDs, or as a characterization media for new organic dye molecules. Thin films were deposited by dip-coating and characterized by absorption and reflection UV-VIS, photoluminescence, SEM, and Z-scan technique to verify their nonlinear behavior. R6G dye dopant has been used to verify that the nanohybrid matrix does not inhibit its optical properties.

## 1. Introduction

There is a need for developing new economical and simple materials suitable for different applications, in particular those related to nonlinear optical behavior, for applications ranging from nanomedicine to nanoelectronics. For instance, when a nonlinear material is doped with an organic dye it can be used as a laser medium for solid-state organic dye lasers. Nowadays solid-state polymeric dye lasers are of interest [1–3]; they can be used in medicine and cosmetology [4–6], optics [7, 8], electronics [9, 10], and other disciplines. New ways to generate laser light have been developed; tunable solid-state lasers can be obtained by the incorporation of guest dyes in solid host materials and this is one of the ideas that motivates this work. So far, several light-emitting solid systems based on the inclusion of laser dyes inside organic and inorganic solid matrix and hybrid and nanohybrid materials have been developed [11]. The use of

sol-gel technique [12] allows incorporating dyes in a solid material at the nanoscale; this technique is based on the hydrolysis of a precursor, forming a gel, and in this part of the process a dopant can be added. When solvents are volatilized a nanoporous glass with the inclusion of the dopant is obtained. So this technique is important because it can change optical, mechanical, thermal, and electrical properties of the matrix formed by the precursor by adding different kinds of dopants like powders, liquids, organic and inorganic materials, nanoparticles, and so forth. The dopants chosen depends on the required material properties and the changes on the amount of dopant inside the matrix. For example, it is possible to add an organic dye to have specific optical properties and some polymer to change its mechanical properties, like flexibility, or to protect the organic dye; PMMA (polymethylmethacrylate) decreases organic dyes degradation on solid-state dye lasers. OLEDs [13, 14] are another technology where organic dyes are used

and can be created with sol-gel technique adding dopants like R6G (rhodamine 6G), an element of a family of dye molecules used in a variety of applications. As a dye it can be used in staining materials or as a tracer in flow and speed determinations of water or other solvents. It possesses a characteristic absorbance spectrum which can be easily detected. In addition R6G fluoresces with high efficiency making it an invaluable component of a dye laser which can be pumped by the second harmonic of a Nd:YAG laser ( $\lambda = 532$  nm); for this purpose its very important to study its photobleaching features in order to know how it degrades under the incident pump laser; this is achieved by doping PMMA with R6G [15]. The optical properties of a hybrid material can be tailored doping it with several dyes in order to obtain a variety of emission lines; this could be of interest in the manufacture of dye lasers [16].

## 2. Experimental

The sol-gel technique is characterized by many of its advantages such as simplicity of the synthesis, facility to be prepared at room temperature, and convenience to be doped with different materials like powders or liquids. This is important because dopant can change the optical or mechanical properties of the material, at the nanoscale, for example, by adding PMMA to a nanoporous silica matrix improving a more flexible material in comparison to a pure nanoporous silica matrix that is hard. We choose silica and PMMA as precursors because both are transparent materials at visible region so they do not change the optical properties of organic dyes and R6G was chosen for its well-known UV-Vis spectra, so R6G:ethanol spectrum can be compared with Hyb:R6G to check for changes. Deep-coating technique is used to grow thin films on glass substrates.

For the synthesis of this nanohybrid material [17], by sol-gel technique two steps are required; reaction was initiated with MMA and some pills of NaOH in a clean flask; the reaction was allowed to proceed for 15 min. In a second glass MMA, TEOS (tetraethyl orthosilicate), TMSPM, ethanol, and water are poured with molar ratio MMA:TEOS:TMSPM:ethanol:water of 3:1:1:15:15. Finally both containers are poured into one glass and drops of HCl are added to obtain a pH 4. It was stirred for 24 hours. All reactions occurred at room temperature. R6G was used as dopant with a molar ratio TEOS:R6G of 1:0.001; that is, the molar amount ( $\nu$ ) of R6G added to the hybrid matrix is given by  $\nu = 0.001\nu_{\text{TEOS}}N$ , where  $\nu_{\text{TEOS}}$  are the moles of TEOS and  $N$  the concentration number of R6G which goes from  $N = 0$  not dopant,  $N = 1$  the first concentration of R6G, and so on until saturation.

Thin films were deposited using deep-coating technique on glass substrates previously cleaned in piranha solution, rinsed in ethanol, and dried at room temperature. Thin film thickness is controlled by fixing the substrate deposition extraction rate and speed.

A Spectronic Unicam UV 300 spectrometer was used to measure absorption and reflectance UV-Vis; photoluminescence was obtained using a B&W TEK 407 nm violet solid state laser 3.04 eV, 60  $\mu$ W, Sciencetech 9040 monochromator

of 0.5 m optical path. For the Z-scan technique was used a He:Ne laser as light source,  $\lambda = 633$  nm of 10 mW of power; SEM micrographs were taken in a JEOL JSM-6610.

## 3. Results and Discussion

Figure 1 contains the IR-transmission spectrum of nanohybrid matrix and nanohybrid matrix doped with R6G; no mayor differences were found because R6G does not change the nanohybrid matrix. We can find bands representing the nanoporous silica matrix at 1194 and 939  $\text{cm}^{-1}$  for Si-O-Si and Si-OH asymmetric stretching vibrations, respectively, also among those bands can find one related to Si-O-CH<sub>3</sub>; and a peak at 787  $\text{cm}^{-1}$  related to Si-O-Si symmetrical vibrations. Some other bands related to PMMA are found at 2351  $\text{cm}^{-1}$  and 2912  $\text{cm}^{-1}$ . This indicates that the nanoporous silica matrix and the polymeric matrix are independent of each other; they are related only by a bending vibration at 1457  $\text{cm}^{-1}$  due to TMSPM. The aliphatic chain -CH- is revealed through a stretching band at 2959  $\text{cm}^{-1}$ . Absorbed water band is at 3350  $\text{cm}^{-1}$ . A weak C=C peak at 1700  $\text{cm}^{-1}$  is due to unpolymerized MMA; CH<sub>2</sub> band is at 2926  $\text{cm}^{-1}$  and an aliphatic chain -CH- at 2840  $\text{cm}^{-1}$ .

Beer-Lambert law ( $A = mct$ ,  $m$  molar absorbance coefficient) shows that absorbance  $A$  increases when dopant concentration  $c$  or sample thickness  $t$  is increased. That behavior is observed in Figure 2, where we plot thin films absorption spectra of the nanohybrid material at different concentrations of R6G, without R6G ( $N = 0$ ), with a first concentration of R6G ( $N = 1$ ), and so forth. When R6G concentration is increased the absorbance increases. Another way to change the absorbance is by changing the film thickness; however, in all the samples used here thickness remains constant because the speed of immersion and extraction of the substrates were fixed.

R6G is absorbed in the visible spectrum between 440 nm and 580 nm, corresponding to frequencies between the end of violet and half yellow having a maximum absorption for the green at 532 nm (Figure 2); a secondary maximum is shown at 490 nm, so R6G absorption spectrum profile is the convolution of two absorptions. The same profile is generated with ethanol:R6G. The authors Lu and Penzkofer [18] determine the optical properties of R6G dissolved in methanol and of a solid R6G film finding deviations from Beer's law due to the mutual interactions of neighbouring molecules and explain what the main and secondary peak are due for the generation of monomers and dimmers of R6G. R6G dissolved in methanol shows a peak at 530 nm, due to monomers and a secondary peak at 490 nm due to dimmers or multimers; monomers population is higher than dimmers. In the case of the hybrid material ethanol is part of the medium and during the hydrolysis reaction ethanol is produced so R6G immersed in the hybrid matrix has the same behavior as in methanol. This is the reason why the absorbance spectrum is maintained; on the other hand PMMA and SiO<sub>2</sub> are transparent at visible region of the spectrum so they do not have any optical contribution to the dye absorbance.

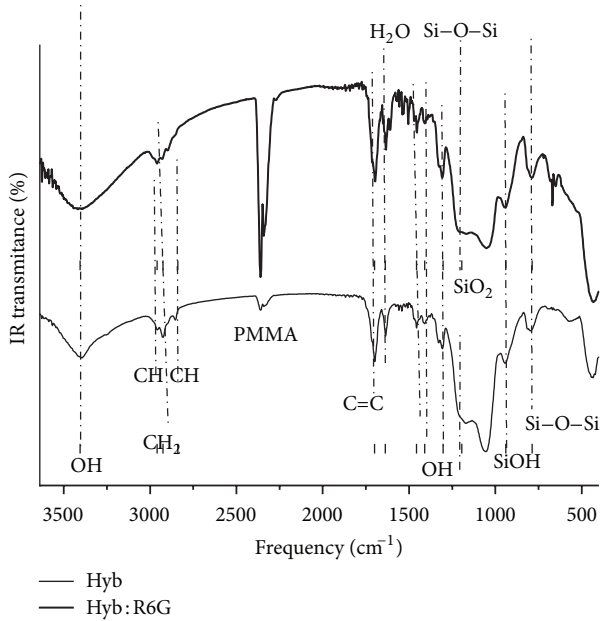


FIGURE 1: IR transmittance for hybrid material and Hybrid:R6G. Silica matrix is represented by Si-O-Si, SiO<sub>2</sub> bounds; polymeric matrix peak is at 2351 cm<sup>-1</sup> and 2912 cm<sup>-1</sup>.

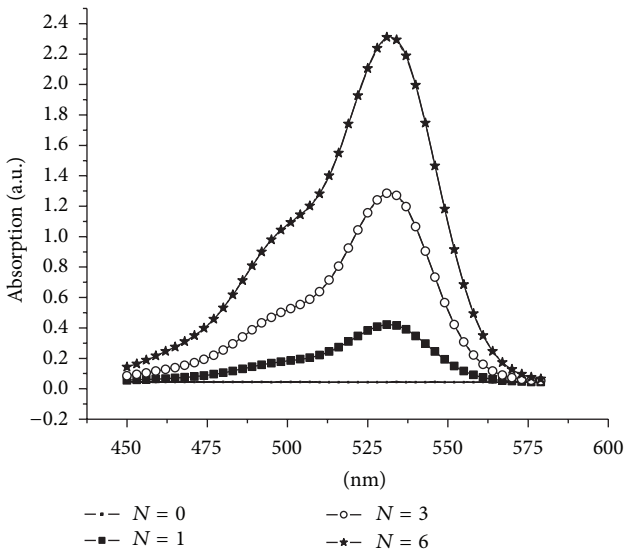


FIGURE 2: Hybrid material does not present absorption at visible spectra; when dopant of R6G is increased absorption response is increased according to Beer-Lambert law; this spectrum is characteristic for the R6G where the principal peak is around 532 nm.

Figure 3 shows the reflectance spectrum of thin films with different concentrations at 30°; when the R6G concentration increases the reflectance of the samples between 450 nm and 590 nm decreases and broadens; it is due to the absorbance at 532 nm; this behavior is useful for a device in which we need to have a filter for those frequencies; the control is generated through the concentration of R6G.

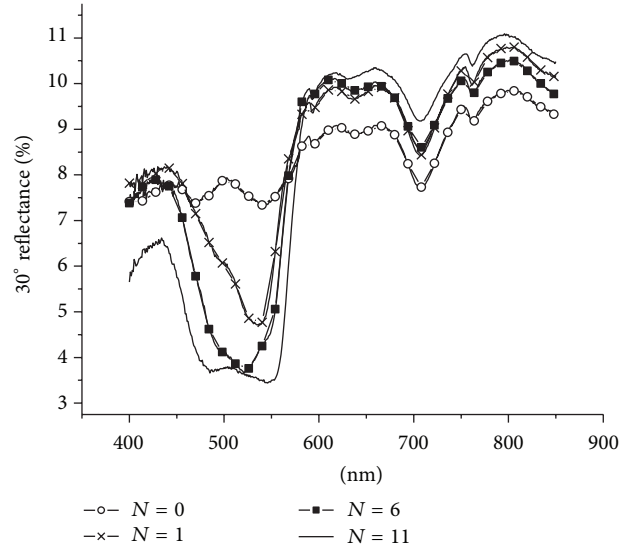


FIGURE 3: Reflectance spectra of the samples without dopant, first concentration of rhodamine 6G, and sixth and eleventh concentration measured at 30 degrees; the higher concentration decreases the reflectance between 450 nm and 590 nm.

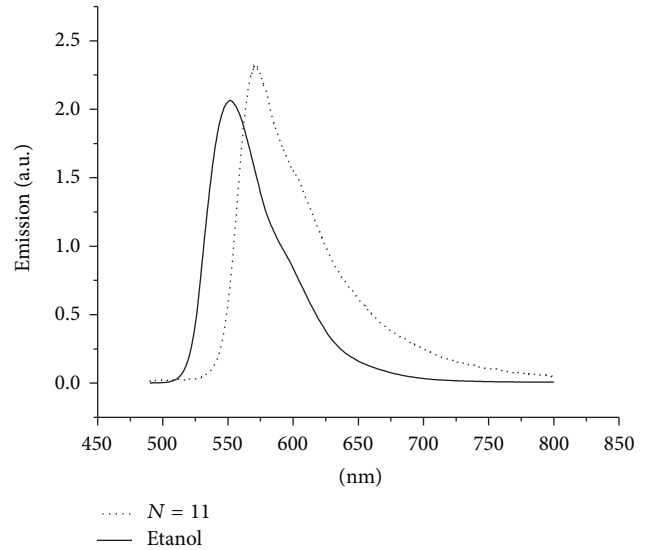


FIGURE 4: Photoluminescence spectra of Hyb:R6G for the eleventh concentration compared to the emission of R6G dissolved in ethanol; both spectra are similar.

Photoluminescence is the emission of light from a material if their atoms were excited by absorption of incident light; when they decay into lower energy states part of the absorbed energy is emitted as photons of less energy than the incidents. Luminescence can be emitted by organic or inorganic compounds. Figure 4 shows the photoluminescence spectrum of the hybrid material doped with R6G showing a maximum luminescence at 571.8 nm, and a secondary at 600 nm; these correspond to the emissions for the absorbed photons at 532 nm and 590 nm, respectively, which is very close to that reported when R6G is immersed in ethylene

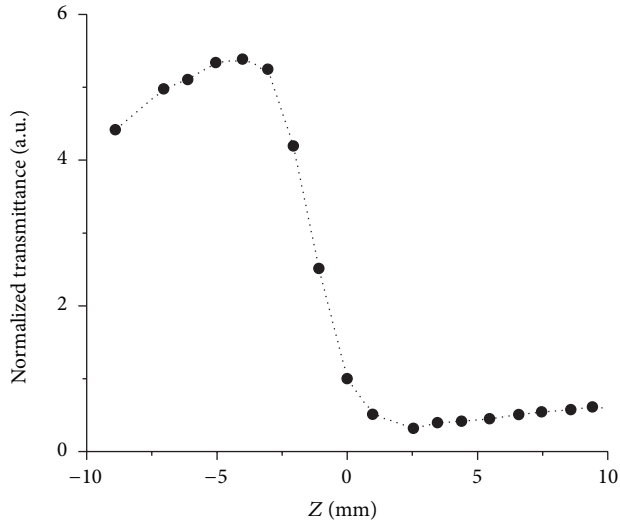


FIGURE 5: Z-scan curve of R6G dissolved in ethanol immersed in the nanohybrid material. Nonlinear behavior is due to the rhodamine 6G molecule. Hybrid material does not inhibit the nonlinear behavior.

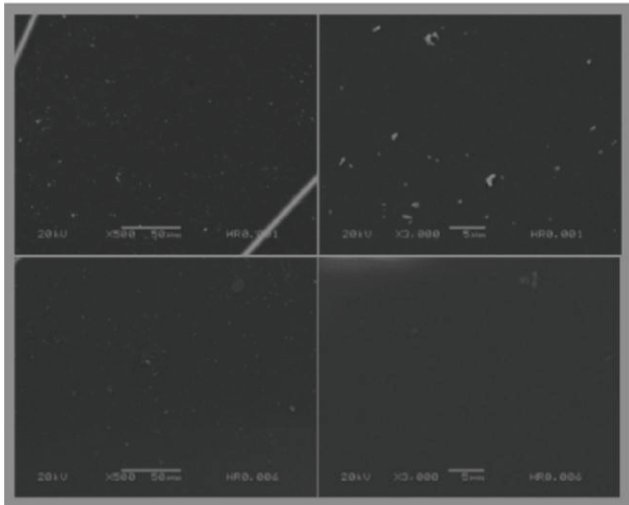


FIGURE 6: Micrographs of thin films with the first (first row) and sixth (second row) concentrations of R6G, at 500x (first column) and 3000x (second column); none of the films show fractures.

glycol [19], where a fluorescence peak is at 578.2 nm and when R6G is immersed in ethanol where the maximum photoluminescence is at 551 nm. So we can argue that the hybrid matrix does not radically change the wavelength of fluorescence of R6G; it is important to notice that hybrid matrix does not present photoluminescence so the observed spectrum is due solely to R6G photoluminescence spectra; the reason that the hybrid matrix does not show emission is because  $\text{SiO}_2$  and MMA were not absorbed at visible region. To know photoluminescence spectra can be of interest to develop a solid-state dye laser [20]. A scintillator is a material used for detection and monitoring of accelerated particles like cosmic rays, among others; R6G is a dye used for scintillators due to its fluorescence emission properties [21].

Not only with R6G optical absorption and fluorescence properties are maintained but also with any organic dye dissolved in ethanol, so the same hybrid matrix can be doped with several organic dyes at the same time maintaining their optical properties. For many years it has been known that some kinds of organic materials exhibit extremely large nonlinear optical and electrooptical responses. The electronic nonlinearities in the most efficient organic materials are essentially based on molecular units containing highly delocalized  $\pi$ -electrons and additional electron-donor and electron-acceptor groups on opposite sides of the molecules. The highly active molecules tend to be highly polarized. The most polar molecules have a tendency to crystallize in a centrosymmetric structure which does not show nonlinear optical effects of second order. The choice of special molecules and the crystal growth methods used are of main importance for obtaining electrooptically active single crystals of good quality and large size. A main advantage of the organic materials is the possibility of altering the molecular structure for optimizing the electrooptical or nonlinear optical properties.

Figure 5 shows the Z-scan curve for a sample of R6G dissolved in ethanol immersed in the nanohybrid material, using as light source a He:Ne laser, with an intensity of  $790 \text{ W/cm}^2$  in the material,  $\lambda = 633 \text{ nm}$ . The sample exhibits a negative nonlinear optical response. This nonlinear behavior is due to the presence of R6G in the hybrid material which does not show a nonlinear optical response so nonlinear curve shown in Figure 5 is only due to R6G dissolved in ethanol, hybrid matrix does not inhibit its nonlinear response which can be modified by increasing dopant quantity or adding different organic dyes.

Different samples were observed by SEM showing that during the drying process of thin films solvents are volatilized breaking the films, but these films do not have fractures (Figure 6) because the polymer matrix is flexible so that the fractures are reduced owing to the matrix by which is opened allowing the passage of solvents.

## 4. Conclusions

A simple and inexpensive optically nonlinear nanohybrid material, based on a TEOS:MMA nanoporous matrix, was developed. Optical response control depends on the thin film thickness or on the amount of dopant; these results can be seen using R6G as reference. The TEOS:MMA hybrid matrix does not change the absorbance and photoluminescence spectra of the organic dopant because TEOS and PMMA are transparent at visible spectra. Sol nanoparticles of the hybrid material doped with an organic dye show optical nonlinear response due to the dopant. Some potential applications for this material include lasers, photochromic coatings, and photoluminescent materials for organic devices and biomedical imaging.

## References

- [1] Y. Li, M. Sasaki, and K. Hane, "Fabrication and testing of solid polymer dye microcavity lasers based on PMMA

- micromolding,” *Journal of Micromechanics and Microengineering*, vol. 11, no. 3, p. 234, 2001.
- [2] S. Singh, V. R. Kanetkar, G. Sridhar, V. Muthuswamy, and K. Raja, “Solid-state polymeric dye lasers,” *Journal of Luminescence*, vol. 101, no. 4, pp. 285–291, 2003.
- [3] D. Schneider, S. Hartmann, T. Benstem et al., “Wavelength-tunable organic solid-state distributed-feedback laser,” *Applied Physics B*, vol. 77, no. 4, pp. 399–402, 2003.
- [4] B. R. Moody, J. E. McCarthy, G. J. Hruza, and M. Alam, “Collagen remodeling after 585-nm pulsed dye laser irradiation: an ultrasonographic analysis,” *Dermatologic Surgery*, vol. 29, no. 10, pp. 997–1000, 2003.
- [5] M. R. Alexiades-Armenakas, J. S. Dover, and K. A. Arndt, “The spectrum of laser skin resurfacing: nonablative, fractional, and ablative laser resurfacing,” *Journal of the American Academy of Dermatology*, vol. 58, no. 5, pp. 719–737, 2008.
- [6] M. Lapidoth, M. E. Y. Odo, and L. M. Odo, “Novel use of erbium: YAG (2,940-nm) laser for fractional ablative photothermolysis in the treatment of photodamaged facial skin: a pilot study,” *Dermatologic Surgery*, vol. 34, no. 8, pp. 1048–1053, 2008.
- [7] R. Bornemann, U. Lemmer, and E. Thiel, “Continuous-wave solid-state dye laser,” *Optics Letters*, vol. 31, no. 11, pp. 1669–1671, 2006.
- [8] T. Li, Z. Zhuo, X. Li, H. Yang, and Y. Zhang, “Study on optical characteristics of Nd:YVO<sub>4</sub>/YVO<sub>4</sub> composite crystal laser,” *Chinese Optics Letters*, vol. 5, no. 3, pp. 175–177, 2007.
- [9] A. Costela, I. García-Moreno, and R. Sastre, “Polymeric solid-state dye laser: recent developments,” *Physical Chemistry Chemical Physics*, vol. 5, no. 21, pp. 4745–4763, 2003.
- [10] G. Wu, C. Li, Y. Liu, N. Dai, and J. Wang, “Study on high resolution time interval measurement module in pulsed laser ranging system,” *Journal of Infrared and Millimeter Waves*, vol. 26, no. 3, pp. 213–221, 2007.
- [11] C. Sanchez, B. Julián, P. Belleville, and M. Popall, “Applications of hybrid organic-inorganic nanocomposites,” *Journal of Materials Chemistry*, vol. 15, no. 35–36, pp. 3559–3592, 2005.
- [12] C. J. Brinker and G. W. Scherer, *Sol-Gel Science: The Physics and Chemistry of Sol-Gel Processing*, Academic Press, 1990.
- [13] B. Choudhury, R. Shinar, and J. Shinar, “Glucose biosensors based on organic light-emitting devices structurally integrated with a luminescent sensing element,” *Journal of Applied Physics*, vol. 96, no. 5, pp. 2949–2954, 2004.
- [14] A. Pais, A. Banerjee, D. Klotzkin, and I. Papautsky, “High-sensitivity, disposable lab-on-a-chip with thin-film organic electronics for fluorescence detection,” *Lab on a Chip*, vol. 8, no. 5, pp. 794–800, 2008.
- [15] N. A. George, B. Aneeshkumar, P. Radhakrishnan, and C. P. G. Vallabhan, “Photoacoustic study on photobleaching of Rhodamine 6G doped in poly(methyl methacrylate),” *Journal of Physics D*, vol. 32, no. 14, pp. 1745–1749, 1999.
- [16] D. Moses, “High quantum efficiency luminescence from a conducting polymer in solution: a polymer laser dye,” *Synthetic Metals*, vol. 55, no. 1, pp. 22–27, 1993.
- [17] E. Rubio, J. Almaral, R. Ramirez-Bon, V. Castaño, and V. Rodríguez, “Organic-inorganic hybrid coating (poly(methyl methacrylate)/monodisperse silica),” *Optical Materials*, vol. 27, pp. 1266–1269, 2005.
- [18] Y. Lu and A. Penzkofer, “Absorption behaviour of methanolic rhodamine 6G solutions at high concentration,” *Chemical Physics*, vol. 107, no. 2–3, pp. 175–184, 1986.
- [19] N. Sharma, N. Singh, H. S. Vora, and S. L. Goyal, “Influence of the medium on the fluorescence of copper vapor laser pumped rhodamine 6G dye: addendum,” *Optics Journal*, vol. 1, pp. 18–22, 2007.
- [20] R. Sasai, N. Iyi, T. Fujita et al., “Luminescence properties of rhodamine 6G intercalated in surfactant/clay hybrid thin solid films,” *Langmuir*, vol. 20, no. 11, pp. 4715–4719, 2004.
- [21] M. Nikl, N. Solovieva, K. Apperson, D. J. S. Birch, and A. Voloshinovskii, “Scintillators based on aromatic dye molecules doped in a sol-gel glass host,” *Applied Physics Letters*, vol. 86, no. 10, Article ID 101914, 3 pages, 2005.

## Research Article

# Influences of InGaP Conical Frustum Nanostructures on the Characteristics of GaAs Solar Cells

Nguyen Dinh Lam, Youngjo Kim, Kangho Kim, and Jaejin Lee

Department of Electrical and Computer Engineering, Ajou University, Suwon 443-749, Republic of Korea

Correspondence should be addressed to Jaejin Lee; [jaejin@ajou.ac.kr](mailto:jaejin@ajou.ac.kr)

Received 12 April 2013; Revised 8 July 2013; Accepted 22 July 2013

Academic Editor: Sudhakar Nori

Copyright © 2013 Nguyen Dinh Lam et al. This is an open access article distributed under the Creative Commons Attribution License, which permits unrestricted use, distribution, and reproduction in any medium, provided the original work is properly cited.

Conical frustums with quasihexagonal nanostructures are fabricated on an InGaP window layer of single junction GaAs solar cells using a polystyrene nanosphere lithography technique followed by anisotropic etching processes. The optical and photovoltaic characteristics of the conical frustum nanostructured solar cells are investigated. Reflectance of the conical frustum nanostructured solar cells is significantly reduced in a wide range of wavelengths compared to that of the planar sample. The measured reflectance reduction is attributed to the gradual change in the refractive index of the InGaP conical frustum window layer. An increase of 15.2% in the power conversion efficiency has been achieved in the fabricated cell with an optimized conical frustum nanostructure compared to that of the planar cell.

## 1. Introduction

Fresnel reflection of incident light comes from the large difference of refractive indexes at the interface between the two materials, especially for air and semiconductor materials. The high refractive index of III-V compound semiconductors such as InGaP and AlGaInP, materials which are utilized for the window layers in III-V solar cell applications, results in optical reflection loss up to 36% for the incident light. This severely limits the performance of solar cells based on III-V materials. Therefore, to suppress the Fresnel reflection at the surface of the solar cells, effective antireflection coating (ARC) is introduced. The conventional multilayer ARCs are usually composed of a quarter wavelength stack of dielectrics with different refractive indices, such as  $\text{SiN}_x$ ,  $\text{SiO}_2$ ,  $\text{TiO}_x$ ,  $\text{MgF}_2$ , and ZnS materials [1–4]. ARCs are usually fabricated by expensive processes such as plasma-enhanced chemical vapor deposition, electron beam evaporator, or sputtering. Under strong illumination in space or concentration applications, ARC has several problems such as mechanical and thermal stability, adhesion, and thermal mismatch. To overcome these issues, surface patterning with subwavelength structures is introduced as an alternative technique for reduction of incident light reflectance [5, 6].

Subwavelength structures can exhibit polarization insensitive, broadband, and omnidirectional antireflective characteristics [7–9]. That is due to the spatially graded structural profile in a single layer. In addition, the subwavelength structure can be robust and mechanically durable, making it particularly desirable for concentrator and space photovoltaic applications. Therefore, various cost-effective self-assembly techniques were employed to fabricate subwavelength nanostructures on different materials such as Si, GaAs, Ge, and AlGaInP [10–13]. Cost-effective subwavelength structures may be fabricated by thermally dewetted Au, Ag, Pt/Pd, and Ni nanotemplates and thereafter pattern-transfer processes. However, their high dewetting temperature makes it difficult to apply this technique for the subwavelength structure fabrication on top of the III-V solar cells, and fabricated nanostructures tend to be in disorder. As has been well known, to form ohmic contacts, samples are usually heated by a rapid thermal annealing (RTA) process in range of 350 to 400°C for 30 s. Performance of the solar cell devices will also be degraded by a deep diffusion of metal into the epitaxial layers at higher annealing temperature of 400°C. Surface oxidation is also another issue when the samples are heated at high temperature for a long time. Increased surface recombination probability will result in the reduction

p-contact	Ti/Pt/Au	500 nm
p-ohmic	p <sup>+</sup> -GaAs	300 nm
Window	p <sup>+</sup> -In <sub>0.5</sub> Ga <sub>0.5</sub> P	200 nm
Emitter	p-GaAs	500 nm
Base	n-GaAs	3,500 nm
BSF	n <sup>+</sup> -In <sub>0.5</sub> Ga <sub>0.5</sub> P	50 nm
Buffer	n-GaAs	200 nm
Substrate	n <sup>+</sup> -GaAs	350 μm
n-contact	AuGe/Ni/Au	500 nm

FIGURE 1: Schematic of the fabricated single junction GaAs solar cell.

of photocurrent in solar cell devices. These issues may be overcome by antireflective disordered subwavelength nanostructures fabricated by using spin-coated Ag ink etched mask [14]. This technique is simple, low cost, and large-scale fabrication with a low sintered temperature (below 300°C) that may avoid the metal diffusion and surface oxidation issues. The nanosphere lithography technique is also introduced and has attracted lots of attentions as one of the promising cost-effective subwavelength structure fabrication methods for the solar cell applications. In this technique, polystyrene and silica nanoparticles are usually utilized, and a shadow mask can be formed on the surface of the substrates with a hexagonal geometry without any annealing process [15, 16].

Many researchers have investigated the optical properties of the subwavelength structures for solar cell applications so far [11–13], but only a few publications report directly on the solar cell devices [15, 17]. Although subwavelength structures are suitable for suppression of optical reflection loss in solar cell applications, direct influences of subwavelength structures and fabricated parameters on the performances of solar cell still need to be further investigated. In this work, conical frustums with the quasihexagonal nanostructures are fabricated on the InGaP window layer of the single junction GaAs solar cells using a polystyrene nanosphere lithography technique followed by anisotropic etching processes. The conical frustum nanostructures are varied by diameter and height of the nanoconical frustums. The optical and photovoltaic characteristics of the conical frustum nanostructured solar cells are investigated.

## 2. Experiments

The single junction GaAs solar cell structure is grown on n-type GaAs substrates in a low-pressure metalorganic chemical vapor deposition (MOCVD) reactor. The structure consists of a 0.2 μm-thick GaAs buffer, a 0.05 μm-thick InGaP back surface field (BSF), a 3.5 μm-thick GaAs base, a 0.5 μm-thick GaAs emitter, a 0.2 μm-thick InGaP window, and a 0.3 μm-thick GaAs cap layers, as shown in Figure 1. Photolithography, metal deposition, rapid thermal annealing,

and wet chemical etch processes are applied for the solar cell fabrication. The metal structures are deposited by an e-beam evaporator and annealed by a rapid thermal annealing system. The p<sup>+</sup>-GaAs cap layer is selectively etched in a citric acid solution (CA : H<sub>2</sub>O<sub>2</sub> : H<sub>2</sub>O = 25 : 1 : 75). The solar cells are separated by a dicing saw system. The aperture area of the fabricated solar cell is 0.25 cm<sup>2</sup>.

The InGaP conical frustum nanostructures are fabricated using a nanosphere lithography technique. A monolayer of self-assembled polystyrene (PS) nanospheres with 2 wt% dispersion in isopropanol (IPA) is spin-cast onto the surface of solar cells. By tuning the degree of hydrophilicity, spinning speed, and the mixture concentration, a nearly-close-packed PS nanosphere monolayer is obtained on the surface of the solar cell (Figure 2(a)). In this work, PS nanospheres (Sigma Aldrich) with a diameter of 500 nm are chosen. After steady air drying for 15 minutes, the samples as shown in Figure 2(a) are short baked at 80°C for 10 minutes to increase the adhesion of PS nanospheres to the solar cell surfaces. The diameter of PS nanospheres can be tuned by oxygen reactive ion etching (RIE) plasma process, where a reactive gas O<sub>2</sub> of 30 sccm is introduced with an RF power of 100 W, under a 10 mTorr pressure. Therefore, the diameter of the PS nanospheres is varied from 230 to 500 nm. The conical frustum nanostructures are formed on the InGaP window layer of the solar cells by an inductively coupled plasma reaction ion etching (ICP-RIE) system. The ICP-RIE system is operated with a 200 W ICP and 50 W RF power at a chamber pressure of 10 mTorr. The samples are etched in a gas mixture of 5 sccm BCl<sub>3</sub> and 30 sccm Cl<sub>2</sub> plasma. The gas mixture is controlled through the individual electronic mass flow controllers. After dry etching, residuals of the PS nanospheres are lifted-off by dipping into the pure toluene solution for 20 minutes at room temperature and then cleaned by acetone, isopropanol, and deionized water in succession. The sample without the InGaP conical frustum nanostructure is used as a reference solar cell for comparison purpose. The InGaP conical frustum nanostructure geometry is investigated using a field emission scanning electron microscopy (FE-SEM). The loss of incident light is evaluated by reflectance spectra from 300 to 900 nm which are measured using an UV-Vis-NIR Cary 5000 Spectrometer. The photovoltaic current density-voltage (*J-V*) characteristics of the GaAs solar cells are determined by a solar simulator under 1 sun air mass 1.5G at room temperature. The photocurrent response of the fabricated cells is also investigated at room temperature using a quantum efficiency measurement system (PV Measurements: QEX7).

## 3. Results and Discussions

The SEM images of the fabricated InGaP conical frustum nanostructures on the window layer of the single junction GaAs solar cells are shown in Figures 2(b), 2(c), 2(d), 2(e), and 2(f). The InGaP conical frustum nanostructures can be formed in the quasihexagonal geometry. The height and shape of the InGaP conical frustum nanostructures can be controlled by varying the etching duration and the

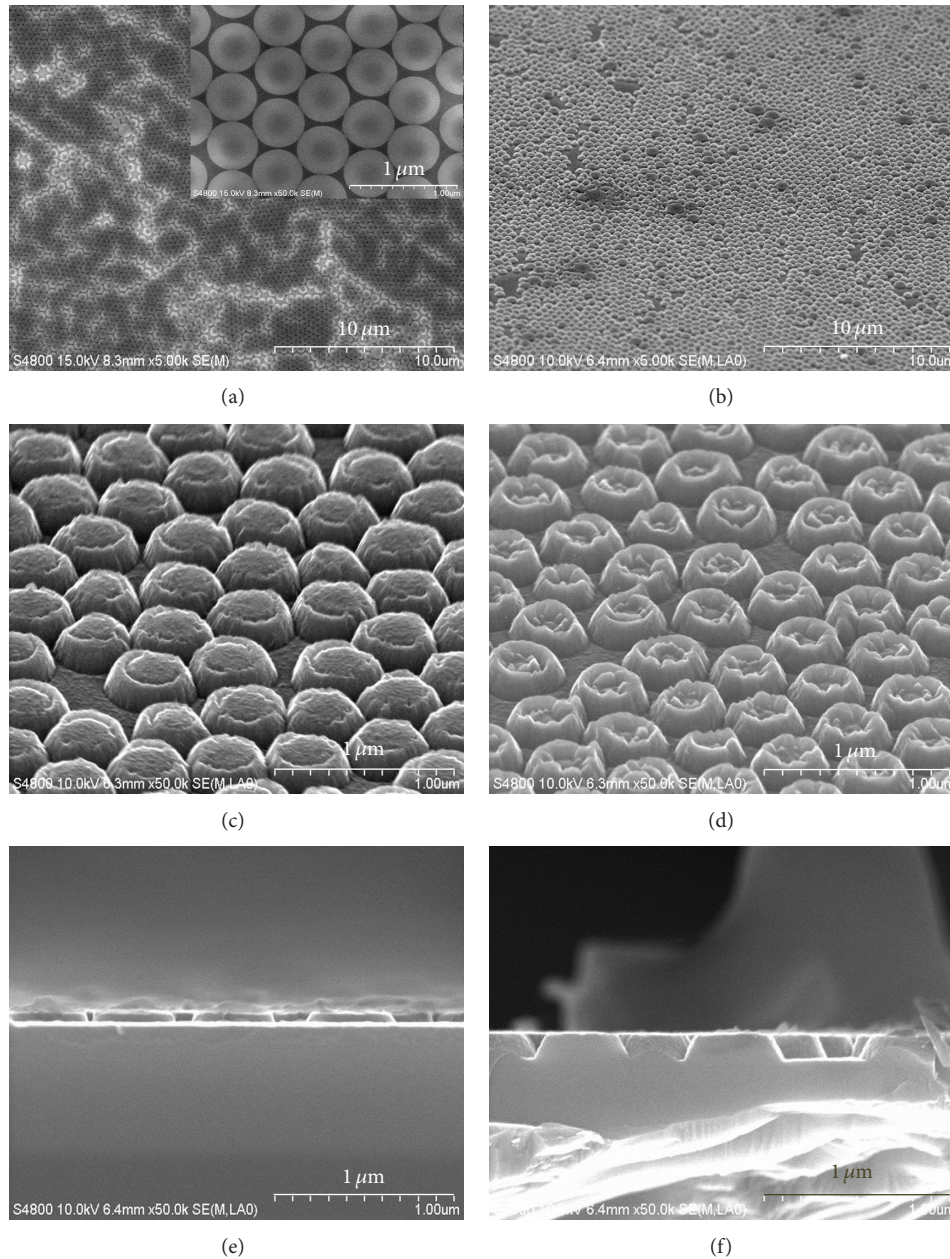


FIGURE 2: (a) SEM images of polystyrene nanospheres coated on the surface of the sample; (b) the conical frustum nanostructure fabricated on the InGaP window layer; (c) and (d) the conical frustum nanostructures fabricated by nanosphere particles with a top diameter of 380 and 300 nm, respectively. SEM images of the 380 nm top diameter conical frustum nanostructures with height of (e) 60 nm and (f) 140 nm.

PS nanosphere thinning process. Conical frustum nanostructures with four different top diameter, that is, 450 nm, 300 nm (Figure 2(c)), 300 nm (Figure 2(d)), and 200 nm, are fabricated on the InGaP window layer. To investigate the influence of the height of the conical frustum on the performances of the GaAs solar cells, the top diameter of the conical frustum is kept at a constant value of 380 nm while the height of the conical frustum is varied from 60 nm (Figure 2(e)) to 140 nm (Figure 2(f)). Figure 3 shows the total reflectance spectra and external quantum efficiency (EQE) of the GaAs solar cells with and without the InGaP conical

frustum nanostructures. The optical reflection loss can be reduced in the whole measured wavelength range as the height of conical frustum nanostructure increases. Two main reasons have been applied to explain the suppression of surface reflectance by the fabricated nanostructure. Firstly, incident light will be redistributed when the spacing of the protuberances is larger than the wavelengths of incident light. Secondly, there is a gradual change in the refractive index, resulting in the Fresnel reflection suppression, when wavelengths of incident light are larger than the spacing of the protuberances [18]. The external quantum efficiency (EQE),

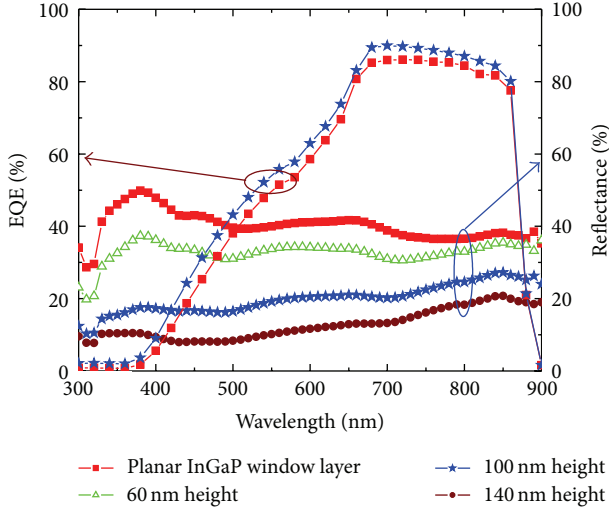


FIGURE 3: Reflectance and external quantum efficiency spectra of the fabricated samples. The height of the conical frustum nanostructures is varied from 60 to 140 nm while the top diameter is kept as a constant value of 380 nm.

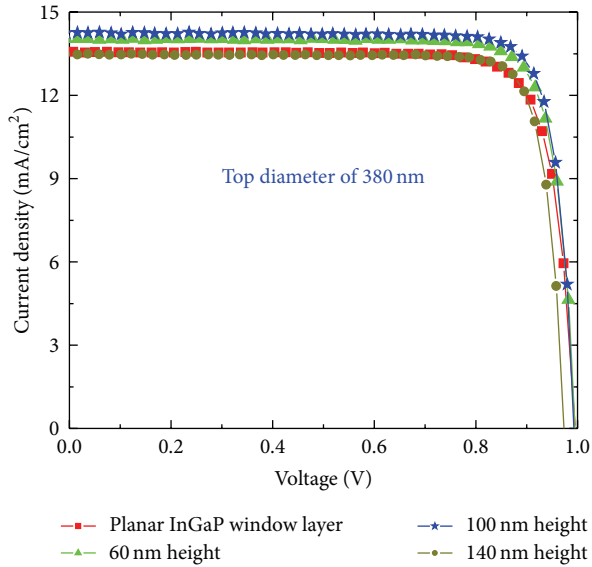


FIGURE 4:  $J$ - $V$  curves of the planar and the patterned GaAs solar cells with a variation of the nanoconical frustum height.

defined as the number of elementary charges collected at the contacts divided by the number of photons impinging on the device, is also characterized for both devices, the planar sample and the conical frustum nanostructured sample with a height of 100 nm. The suppression of the Fresnel reflection contributes to the enhanced optical absorption, which is also reflected in the EQE characteristics. The improvement of the photocurrent response is caused by an excess carrier generation in the p-n junction of the single junction GaAs solar cells resulting from improved light absorption. However, the EQEs of both fabricated samples in the shorter wavelength range of 680 nm are lower than those of the conventional

TABLE 1: Current density-voltage characteristics of the GaAs solar cells with various heights of the InGaP conical frustum nanostructure. The top diameter is kept as a constant value of 380 nm.

Sample	$V_{oc}$ (V)	$J_{sc}$ (mA/cm <sup>2</sup> )	FF (%)	Eff. (%)
Planar cell	0.996	13.558	83.04	11.08
60 nm	0.995	14.030	83.46	11.66
100 nm	0.993	14.242	84.52	11.95
140 nm	0.973	13.477	84.84	11.13

GaAs solar cells with a thin InGaP window layer [19]. It indicated that the absorbed light in the thick InGaP window layer in the fabricated solar cell structure does not contribute to the collected photocurrent. To overcome this issue, higher bandgap materials such as AlInP should be used as a window layer material.

The photovoltaic characteristics of the GaAs solar cell are dependent on the height of the conical frustum nanostructures, as can be seen in Figure 4. The short circuit current density ( $J_{sc}$ ) changes a lot compared to the other parameters such as open circuit voltage ( $V_{oc}$ ) and fill factor (FF). The highest short circuit current density can be obtained when the height of the conical frustum is 100 nm (Table 1). When the height of conical frustum is more than 100 nm, in spite of the lower optical reflectance, the short circuit current density is degraded. Besides that,  $V_{oc}$  is slightly decreased as the height of conical frustum increases. It means that p-n junction of the GaAs solar cell will be further degraded if the etching time is too long. That may be caused by the plasma induced damage in the anisotropic etching process [20]. The nature of this damage is a complex function of many plasma characteristics such as the chemistry of plasma gas, plasma energy, temperature, and pressure. Furthermore, surface damage causes significant enhancement of carrier recombination, resulting in the reduction of the photocurrent response. Therefore, there is a trade-off between the optical reflection loss reduction and the plasma induced damage in the conical frustum nanostructures fabricated on the InGaP window layer of the GaAs solar cells. In addition, as the height of the conical frustum increases, the surface area of the GaAs solar cell will become larger. This will result in a higher probability of surface oxidation and recombination. To relieve the effect of the surface recombination, geometrical designs of nanostructures have to be optimized in the first place to take advantage of the optical reflection loss reduction and carrier collection enhancement without significant increase of the surface recombination. And, on the other hand, surface passivation technique can be applied on nanostructures to reduce the surface recombination.

In order to investigate the influence of top diameter of the conical frustum on the characteristics of the GaAs solar cells, the height of the conical frustum is kept at a value of 100 nm while the top diameter of the conical frustum is varied from 200 to 450 nm.  $J$ - $V$  curves and EQEs of the fabricated samples with the variation in the top diameter of the conical frustum are shown in Figures 5(a) and 5(b), respectively. The corresponding electrical parameters are summarized in Table 2. The characteristics of the GaAs solar cells are also

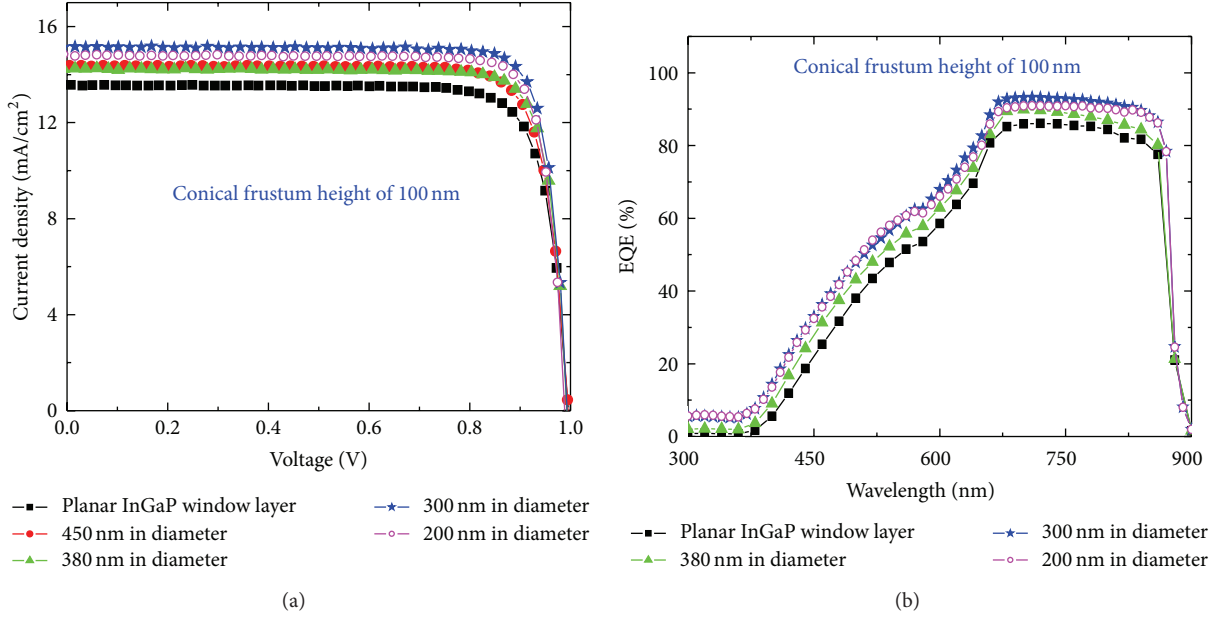


FIGURE 5: (a)  $J$ - $V$  curves and (b) EQEs of the fabricated samples with the height of conical frustum of 100 nm and various top diameters of the InGaP conical frustum nanostructure.

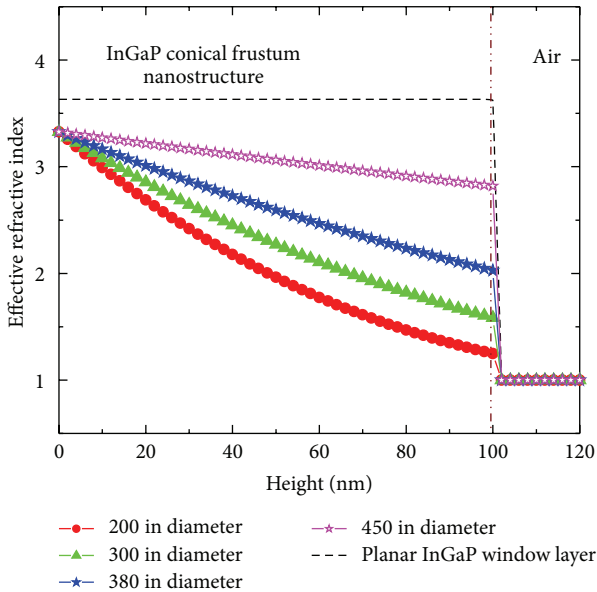


FIGURE 6: Change of the calculated effective refractive index at  $\lambda = 600$  nm from the bottom of nanoconical frustum (height equals zero) to the solar cells with height of 100 nm with a variation in the top diameter of InGaP conical frustum nanostructures. The dashed line indicates the refractive index of bulk InGaP at the same wavelength.

dependent upon the top diameter of the conical frustum. The highest power conversion efficiency can be obtained when the top diameter of the conical frustum is 300 nm, resulting in an increase of 15.2% in the power conversion efficiency of the sample with the InGaP conical frustum nanostructure compared to that of the planar InGaP window layer. The

TABLE 2: Current density-voltage characteristics of the GaAs solar cells with a height of conical frustum of 100 nm and various top diameters of the InGaP conical frustum nanostructure.

Sample	$V_{oc}$ (V)	$J_{sc}$ (mA/cm <sup>2</sup> )	FF (%)	Eff. (%)
Planar cell	0.996	13.558	83.04	11.08
450 nm	0.995	14.370	83.60	11.81
380 nm	0.993	14.242	84.52	11.95
300 nm	0.993	15.149	84.89	12.77
200 nm	0.988	14.828	84.85	12.44

degradation of the current density and EQE, when the top diameter of the conical frustum is 200 nm, may be caused by the oxidation of the InGaP window layer because it is exposed to the high temperature in oxygen gas environment during the PS nanoparticle thinning process. Furthermore, open circuit voltage is further degraded when the top diameter of the conical frustum is reduced.

The broadband antireflection properties of the InGaP conical frustum nanostructures can be further understood by mapping the calculated effective refractive index at a wavelength of 600 nm across the height of 100 nm conical frustum [21], as shown in Figure 6. For the planar InGaP window layer, the refractive index changes sharply from air ( $n_{air} = 1$ ) to InGaP ( $n_{InGaP} = 3.62$ ). While, for the InGaP conical frustum nanostructures, the refractive index changes gradually as the top diameter of conical frustum gets smaller. The refractive index gradient exhibited by the InGaP conical frustum nanostructures thus leads to a very low reflection over wide range of wavelengths.

## 4. Conclusions

InGaP conical frustum nanostructures have been fabricated on top of the GaAs solar cells. The height and the top diameter of the InGaP conical frustum nanostructure variation effect on the solar cell characteristics, including the reflectance, external quantum efficiency, and current density-voltage curves, were measured and compared with those of the planar sample. An increase of 15.2% in the conversion efficiency is obtained at the optimal geometry with a 100 nm height and 300 nm top diameter of the InGaP conical frustum nanostructure. The improvements may be attributed to the gradual change in the refractive index, resulting in the Fresnel reflection suppression and light scattering effect by the InGaP conical frustum nanostructures.

## Acknowledgments

This work was supported by the Converging Research Center Program through the National Research Foundation (NRF) of Korea funded by the Ministry of Education, Science and Technology (no. 2011K000590). This work was also supported by the New and Renewable Energy of the Korea Institute of Energy Technology Evaluation and Planning (KETEP) grant funded by the Korea in government, Ministry of Knowledge Economy (no. 20123010010110).

## References

- [1] C. H. M. van der Werf, H. D. Goldbach, J. Löffler et al., "Silicon nitride at high deposition rate by Hot Wire Chemical Vapor Deposition as passivating and antireflection layer on multicrystalline silicon solar cells," *Thin Solid Films*, vol. 501, no. 1-2, pp. 51–54, 2006.
- [2] D. Li, F. Huang, and S. Ding, "Sol-gel preparation and characterization of nanoporous ZnO/SiO<sub>2</sub> coatings with broadband antireflection properties," *Applied Surface Science*, vol. 257, no. 23, pp. 9752–9756, 2011.
- [3] G. Zhang, J. Zhao, and M. A. Green, "Effect of substrate heating on the adhesion and humidity resistance of evaporated MgF<sub>2</sub>/ZnS antireflection coatings and on the performance of high-efficiency silicon solar cells," *Solar Energy Materials & Solar Cells*, vol. 51, no. 3-4, pp. 393–400, 1998.
- [4] S.-M. Jung, Y.-H. Kim, S.-I. Kim, and S.-I. Yoo, "Design and fabrication of multi-layer antireflection coating for III-V solar cell," *Current Applied Physics*, vol. 11, no. 3, pp. 538–541, 2011.
- [5] A. R. Parker and H. E. Townley, "Biomimetics of photonic nanostructures," *Nature Nanotechnology*, vol. 2, no. 6, pp. 347–353, 2007.
- [6] Y.-F. Huang, S. Chattopadhyay, Y.-J. Jen et al., "Improved broadband and quasi-omnidirectional anti-reflection properties with biomimetic silicon nanostructures," *Nature Nanotechnology*, vol. 2, no. 12, pp. 770–774, 2007.
- [7] H. Sai, Y. Kanamori, K. Arafune, Y. Ohshita, and M. Yamaguchi, "Light trapping effect of submicron surface textures in crystalline Si solar cells," *Progress in Photovoltaics: Research and Applications*, vol. 15, no. 5, pp. 415–423, 2007.
- [8] C. H. Chiu, P. Yu, H. C. Kuo et al., "Broadband and omnidirectional antireflection employing disordered GaN nanopillars," *Optics Express*, vol. 16, no. 12, pp. 8748–8754, 2008.
- [9] Y. Kanamori, M. Sasaki, and K. Hane, "Broadband antireflection gratings fabricated upon silicon substrates," *Optics Letters*, vol. 24, no. 20, pp. 1422–1424, 1999.
- [10] J. W. Leem and J. S. Yu, "Broadband and wide-angle antireflection subwavelength structures of Si by inductively coupled plasma etching using dewetted nanopatterns of Au thin films as masks," *Thin Solid Films*, vol. 519, no. 11, pp. 3792–3797, 2011.
- [11] R. Y. Zhang, B. Shao, J. R. Dong et al., "Broadband quasi-omnidirectional antireflection AlGaInP window for III-V multi-junction solar cells through thermally dewetted Au nanotemplate," *Optical Materials Express*, vol. 2, pp. 173–182, 2011.
- [12] J. W. Leem, Y. M. Song, and J. S. Yu, "Broadband antireflective germanium surfaces based on subwavelength structures for photovoltaic cell applications," *Optics Express*, vol. 19, no. 27, pp. 26308–26317, 2011.
- [13] J. W. Leem, J. S. Yu, Y. M. Song, and Y. T. Lee, "Antireflective characteristics of disordered GaAs subwavelength structures by thermally dewetted Au nanoparticles," *Solar Energy Materials & Solar Cells*, vol. 95, no. 2, pp. 669–676, 2011.
- [14] C. I. Yeo, J. H. Kwon, S. J. Jang, and Y. T. Lee, "Antireflective disordered subwavelength structure on GaAs using spin-coated Ag ink mask," *Optics Express*, vol. 20, pp. 19554–19562, 2012.
- [15] M.-Y. Chiu, C.-H. Chang, M.-A. Tsai, F.-Y. Chang, and P. Yu, "Improved optical transmission and current matching of a triple-junction solar cell utilizing sub-wavelength structures," *Optics Express*, vol. 18, no. 19, pp. A308–A313, 2010.
- [16] K. Cho, D. J. Ruebusch, M. H. Lee et al., "Molecular monolayers for conformal, nanoscale doping of InP nanopillar photovoltaics," *Applied Physics Letters*, vol. 98, no. 20, Article ID 203101, 2011.
- [17] Y. T. Lee, Y. M. Song, J. H. Jang, J. C. Lee, and E. K. Kang, "Disordered submicron structures integrated on glass substrate for broadband absorption enhancement of thin-film solar cells," *Solar Energy Materials & Solar Cells*, vol. 101, pp. 73–78, 2012.
- [18] Y. Li, J. Zhang, and B. Yang, "Antireflective surfaces based on biomimetic nanopillared arrays," *Nano Today*, vol. 5, no. 2, pp. 117–127, 2010.
- [19] J. Pla, M. Barrera, and F. Rubinelli, "The influence of the InGaP window layer on the optical and electrical performance of GaAs solar cells," *Semiconductor Science and Technology*, vol. 22, no. 10, p. 1122, 2007.
- [20] S. H. Zaidi, D. S. Ruby, and J. M. Gee, "Characterization of random reactive ion etched-textured silicon solar cells," *IEEE Transactions on Electron Devices*, vol. 48, no. 6, pp. 1200–1206, 2001.
- [21] D. G. Stavenga, S. Foletti, G. Palasantzas, and K. Arikawa, "Light on the moth-eye corneal nipple array of butterflies," *Proceedings of the Royal Society B*, vol. 273, no. 1587, pp. 661–667, 2006.

## Research Article

# Hydrogenic-Donor Impurity Binding Energy Dependence of the Electric Field in GaAs/Al<sub>x</sub>Ga<sub>1-x</sub>As Quantum Rings

Guangxin Wang,<sup>1</sup> Xiuzhi Duan,<sup>2</sup> and Wei Chen<sup>1</sup>

<sup>1</sup> College of Science, Hebei United University, Tangshan 063000, China

<sup>2</sup> College of Light Industry, Hebei United University, Tangshan 063000, China

Correspondence should be addressed to Guangxin Wang; [guangxinwang@126.com](mailto:guangxinwang@126.com)

Received 11 June 2013; Revised 2 July 2013; Accepted 2 July 2013

Academic Editor: Yogendra Mishra

Copyright © 2013 Guangxin Wang et al. This is an open access article distributed under the Creative Commons Attribution License, which permits unrestricted use, distribution, and reproduction in any medium, provided the original work is properly cited.

Using a variational method with two-parameter trial wave function and the effective mass approximation, the binding energy of a donor impurity in GaAs/Al<sub>x</sub>Ga<sub>1-x</sub>As cylindrical quantum ring (QR) subjected to an external field is calculated. It is shown that the donor impurity binding energy is highly dependent on the QR structure parameters (radial thickness and height), impurity position, and external electric field. The binding energy increases inchmeal as the QR parameters (radial thickness and height) decrease until a maximum value for a central impurity and then begins to drop quickly. The applied electric field can significantly modify the spread of electronic wave function in the QR and shift electronic wave function from the donor position and then leads to binding energy changes. In addition, results for the binding energies of a hydrogenic donor impurity as functions of the impurity position and applied electric field are also presented.

## 1. Introduction

With rapid advances of modern nanofabrication technology, it has become possible to fabricate novel quantum nanostructures. Many experimental [1–6] and theoretical [7–28] works have triggered strong interest to the study of these semiconductor nanostructures due to their potential applications in electric and optoelectronic devices. The GaAs/Al<sub>x</sub>Ga<sub>1-x</sub>As quantum ring (QR) is a special confined structure. The system is assumed to be the symmetric annulations of GaAs material surrounded by Al<sub>x</sub>Ga<sub>1-x</sub>As material, which exhibit fascinating behavior and interesting electronic and optical properties. The signal QR and double quantum ring (DQR) systems have been grown experimentally by the use of the droplet epitaxial technique and molecular beam epitaxial technique [4–6]. Many works related to the theoretical investigation of the electron structures, the excitonic property, and the optical properties of semiconductor quantum ring have been studied by different groups [7–12]. Li and Xia [7, 8] studied the electronic states of InAs/GaAs QR (GaAs/Al<sub>x</sub>Ga<sub>1-x</sub>As DQR) in the frame of effective mass envelop function theory. The papers show

that the electron energy levels are sensitively dependent on the radial thickness, the height of the QR (DQR), and the applied magnetic field. Except for the energy levels of the carriers, other effects can be obtained in the ring, such as the Aharonov-Bohm oscillation induced by the magnetic field [9, 10] and the Stark effect related to the electric field [11, 12]. For instance Barticevic et al. [9] studied the electronic and optical properties of quantum rings under magnetic fields. Farias et al. [10] calculated the energy spectrum of semiconductor quantum rings taking into account the external magnetic field applied perpendicularly to the structure in the finite confinement potential. On the other hand, the influence of lateral-radial electric field on the electronic and optical properties of a QR in the regime of strong quantization was also studied [11]. Harutyunyan [12] has also investigated the effects of lateral strong electric field on (1D) excitonic states and excitonic electroabsorption spectrum.

Impurity states have played an important role in the semiconductor revolution. Recently, many theoretical works have been carried out on shallow donors impurity states in QRs employing the matrix diagonalization method [13], the analytical and numerical approaches [14, 15], or variational

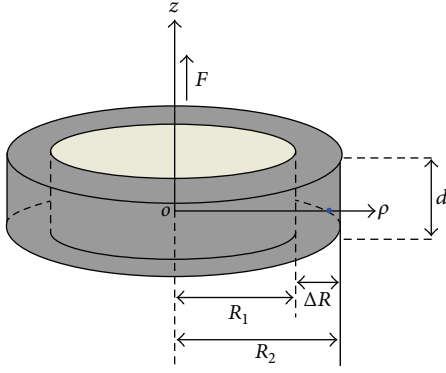


FIGURE 1: The graph defines the dimensions of the QR heterostructure and shows the radial coordinate  $\rho$  and the axial coordinate  $z$ . The QR heterostructure:  $R_1$  is the inner radii of the ring,  $R_2$  is the outer radii of the ring,  $d$  is the height of the ring,  $\Delta R$  is the radial thickness of the ring, and the electric field  $F$  is applied parallel to the  $z$  axis of the QR.

approach in [16–20, 22]. The linear and the third-order nonlinear optical absorption spectra of a donor impurity confined by a quantum ring are studied using the matrix diagonalization method within the effective-mass approximation in [13]. An analytical approach to the problem of an impurity positioned in a QR in the presence of crossed magnetic (axial directed) and electric (radial directed) fields is developed in [14]. In the same approach, Monozon et al. [15] also investigated the problem of an impurity in a QR in the presence of a radially directed strong external electric field in detail. On the other hand, a theoretical study of shallow donor states in GaAs-(Ga,Al)As QRs, within the effective mass approximation and using the variational method, is presented in [16, 22]. The explicit dependencies of the binding energy of the impurity electron on the magnetic field strength, the parameters of the QR, and the position of the impurity within the QR are obtained. The effects of a positively charged impurity on the single and many electron energy states in semiconductor QR under applied magnetic field have been put forward in [17]. On the other hand, Barseghyan and coworkers [18, 19] have used the variational method and the effective mass and parabolic band approximations to study the behavior of the binding energy and photoionization cross-section of a hydrogenic-like donor impurity in InAs quantum ring with the Pöschl-Teller confinement potential along the axial direction. In the investigation, the combined effects of hydrostatic pressure and electric and magnetic fields applied in the growth direction have been also taken into account. The hydrogen-like donor binding energy in GaAs/Ga<sub>1-x</sub>Al<sub>x</sub>As concentric double quantum rings was investigated [20] considering the effects of hydrostatic pressure, temperature, aluminum concentration, and impurity position. We [22, 28] have investigated the hydrogenic impurity binding energy in GaAs/Al<sub>x</sub>Ga<sub>1-x</sub>As QR without external influences and the hydrogenic impurity states in GaAs QR in infinite potential barrier by the use of variational approach.

As far as we know, no studies have been made of electric field effect on the binding energy of a donor impurity in

a GaAs/Al<sub>x</sub>Ga<sub>1-x</sub>As QR by using a variational method with two-parameter trial wave function. In this work, the binding energy of a donor impurity was investigated as functions of the sizes of the QR (radial thickness  $\Delta R$  and height), the applied electric field, and the impurity position. Calculations are made in the effective mass approximations and finite potential barrier confinement. The paper is organized as follows: in Section 2 we describe the theoretical framework, Section 3 is dedicated to the results and discussion, and finally, our conclusions are given in Section 4.

## 2. Theoretical Model

Within the frame of the effective mass approximation, the Hamiltonian for a hydrogenic donor impurity in cylindrical GaAs/Al<sub>x</sub>Ga<sub>1-x</sub>As QR with an applied electric field parallel to the QR  $z$  axis as shown in Figure 1 is given by [13, 21, 22]

$$H = \begin{cases} -\nabla^2 + \eta z - \frac{2}{\sqrt{(\rho - \rho_0)^2 + (z - z_0)^2}} + V(\rho, z) & R_1 \leq \rho \leq R_2, |z| \leq \frac{d}{2} \\ -\frac{m_1^*}{m_2^*} \nabla^2 - \frac{2}{\sqrt{(\rho - \rho_0)^2 + (z - z_0)^2}} + V(\rho, z) & \text{others.} \end{cases} \quad (1)$$

Here, the effective Bohr radius  $a^* = \hbar^2 \epsilon_0 / m_1^* e^2$  and the effective Rydberg constant  $R_y = m_1^* e^4 / 2 \hbar \epsilon_0^2$  in GaAs material are used as the units of length and energy, respectively. One has  $\eta = ea^* F / R_y$ , which denotes a dimensionless measure of the electric field, where  $\rho(\rho_0)$  and  $z(z_0)$  are the coordinates of the electron (impurity) in the GaAs/Al<sub>x</sub>Ga<sub>1-x</sub>As QR.  $m_1^*$  and  $m_2^*$  are the electron effective mass in GaAs and Al<sub>x</sub>Ga<sub>1-x</sub>As materials, respectively.  $V(\rho, z)$  is the electron confinement potential due to the conductor band offset in the GaAs/Al<sub>x</sub>Ga<sub>1-x</sub>As QR which is given by [15]

$$V(\rho, z) = \begin{cases} 0 & R_1 \leq \rho \leq R_2, |z| \leq \frac{d}{2}, \\ V_0 & \text{others.} \end{cases} \quad (2)$$

Here, the aluminum concentration is  $x = 0.3$ , and the finite barrier height  $V_0 = 0.6 (1.36x + 0.22x^2)$  (eV) [16, 25]. If we assume that the in-plane and on-axis motions of the electron are weakly coupled in calculating the energy of the hydrogenic donor impurity in the GaAs/Al<sub>x</sub>Ga<sub>1-x</sub>As QR, the trial wave function may be written [21] as

$$\psi(\rho, \varphi, z) = N \phi(\rho, \varphi) f(z) \exp[-\lambda(\rho - \rho_0)^2 - \tau(z - z_0)^2], \quad (3)$$

where  $\lambda, \tau$  are variational parameters. The radial wave function  $\phi(\rho, \varphi)$  can be obtained using the ordinary (modified) Bessel functions of order  $m$  ( $m = 0, 1, 2, \dots$ ). Employing the

continuity relation of radial wave function at  $\rho = R_1$  and  $\rho = R_2$ , the radial part of wave function is given by [9]

$$\phi(\rho, \varphi) = \begin{cases} \frac{N_0 J_0(\beta R_1) + Y_0(\beta R_1)}{I_0(\alpha R_1)} I_0(\alpha \rho) & \rho < R_1, \\ N_0 J_0(\beta \rho) + Y_0(\beta \rho) & R_1 \leq \rho \leq R_2, \\ \frac{N_0 J_0(\beta R_2) + Y_0(\beta R_2)}{K_0(\alpha R_2)} K_0(\alpha \rho) & \rho > R_2. \end{cases} \quad (4)$$

By the requirement of the continuity of the derivative of the radial wave function at  $\rho = R_1$ , the constant  $N_0$  is given by

$$N_0 = \frac{-m_2^* \beta Y_1(\beta R_1) I_0(\alpha R_1) - m_1^* \alpha Y_0(\beta R_1) I_1(\alpha R_1)}{m_2^* \beta J_1(\beta R_1) I_0(\alpha R_1) + m_1^* \alpha J_0(\beta R_1) I_1(\alpha R_1)}, \quad (5)$$

using the boundary condition [22]

$$\begin{aligned} & \frac{1}{m_1^*} \frac{\partial [N_0 J_0(\beta \rho) + Y_0(\beta \rho)]}{\partial \rho} \Big|_{\rho=R_2} \\ &= \frac{1}{m_2^*} \frac{N_0 J_0(\beta R_2) + Y_0(\beta R_2)}{K_0(\alpha R_2)} \frac{\partial K_0(\alpha \rho)}{\partial \rho} \Big|_{\rho=R_2}, \end{aligned} \quad (6)$$

where the radial ground state energy  $E_{0\rho}$  and the constants  $(\alpha, \beta)$  are determined by (5) and (6), which are given by

$$\alpha = \sqrt{\frac{m_2^*}{m_1^*} (V_0 - E_{0\rho})}, \quad \beta = \sqrt{E_{0\rho}}. \quad (7)$$

In addition,  $f(z)$  is the eigenfunction of the electron along the growth direction of the GaAs/Al<sub>x</sub>Ga<sub>1-x</sub>As QR [24]:

$$f(z) = \begin{cases} C_1 \exp \left[ k_1 \left( z + \frac{d}{2} \right) \right] & z < -\frac{d}{2}, \\ D_1 Ai(\xi) + D_2 Bi(\xi) & |z| \leq \frac{d}{2}, \\ C_2 \exp \left[ -k_2 \left( z - \frac{d}{2} \right) \right] & z > \frac{d}{2}, \end{cases} \quad (8)$$

where  $Ai(\xi)$  and  $Bi(\xi)$  are the Airy functions. The coefficients  $C_1$  and  $C_2$  are determined by the continuity relation of the wave function  $f(z)$  at  $z = \pm d/2$ :

$$\begin{aligned} C_1 &= D_1 Ai(\xi_1) + D_2 Bi(\xi_1), \\ C_2 &= D_1 Ai(\xi_2) + D_2 Bi(\xi_2), \end{aligned} \quad (9)$$

where

$$\begin{aligned} \xi &= \frac{\eta z - E_{0z}}{\eta^{2/3}}, \\ \xi_1 &= \frac{\eta(-d/2) - E_{0z}}{\eta^{2/3}}, \\ \xi_2 &= \frac{\eta(d/2) - E_{0z}}{\eta^{2/3}}, \end{aligned}$$

$$Ai(Bi)(\xi_1) = Ai(Bi) \left( \frac{\eta(-d/2) - E_{0z}}{\eta^{2/3}} \right), \quad (10)$$

$$Ai(Bi)(\xi_2) = Ai(Bi) \left( \frac{\eta d/2 - E_{0z}}{\eta^{2/3}} \right),$$

$$Ai'(Bi') = \frac{dAi(\xi) [Bi(\xi)]}{d\xi},$$

$$k_{1,2} = \sqrt{\frac{m_2^*}{m_1^*} (V_{1,2} - E_{0z})}, \quad V_{1,2} = V_0 \mp \eta \frac{d}{2}.$$

Using the continuity relation of the derivative of the axis wave function at  $z = \pm d/2$  [25],

$$\begin{aligned} & \frac{1}{m_1^*} \frac{d \exp \{C_1 [k_1 (z + d/2)]\}}{dz} \Big|_{z=-d/2} \\ &= \frac{1}{m_2^*} \frac{d [D_1 Ai(\xi) + D_2 Bi(\xi)]}{dz} \Big|_{z=-d/2}, \\ & \frac{1}{m_1^*} \frac{d \exp \{C_1 [-k_2 (z - d/2)]\}}{dz} \Big|_{z=d/2} \\ &= \frac{1}{m_2^*} \frac{d [D_1 Ai(\xi) + D_2 Bi(\xi)]}{dz} \Big|_{z=d/2}. \end{aligned} \quad (11)$$

The axial ground energy  $E_{0z}$  with the applied electric field with no impurity may be obtained by solving the transcendental equation using the boundary condition [25]

$$\begin{aligned} & m_2^2 \eta^{2/3} [Ai'(\xi_2) Bi'(\xi_1) - Ai'(\xi_1) Bi'(\xi_2)] \\ &+ m_1 m_2 k_1 \eta^{1/3} [Ai(\xi_1) Bi'(\xi_2) - Bi(\xi_1) Ai'(\xi_2)] \\ &- m_1 m_2 k_2 \eta^{1/3} [Ai(\xi_2) Bi'(\xi_1) - Ai'(\xi_1) Bi(\xi_2)] \\ &- m_1^2 k_1 k_2 [Ai(\xi_1) Bi(\xi_2) - Ai(\xi_2) Bi(\xi_1)] = 0. \end{aligned} \quad (12)$$

With the adiabatic approximation, the binding energy of a hydrogenic donor impurity  $E_b$  is defined as the difference between the ground state energy of the system without impurity and the ground state energy of the system with impurity [20]; that is,

$$E_b = E_{0\rho} + E_{0z} - \min_{\lambda, \tau} \frac{\langle \psi | \hat{H} | \psi \rangle}{\langle \psi | \psi \rangle}. \quad (13)$$

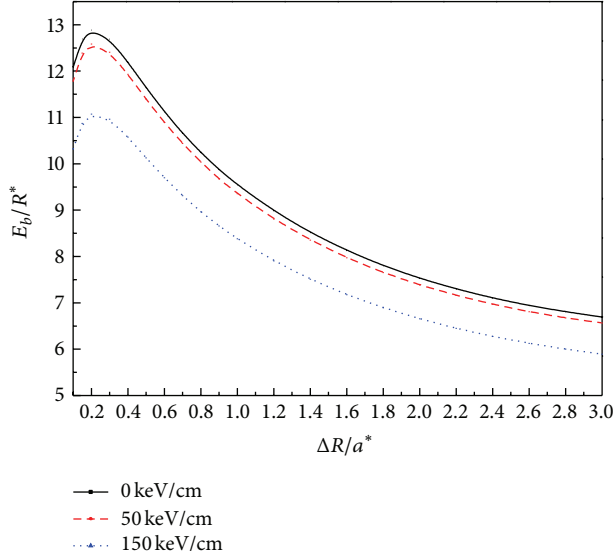


FIGURE 2: Binding energy of a donor impurity in a cylindrical GaAs/Al<sub>x</sub>Ga<sub>1-x</sub>As QR as a function of the QR radial thickness ( $\Delta R$ ) for  $R_1 = 0.3a^*$ ,  $d = 1.0a^*$ , and several values of the applied electric field.

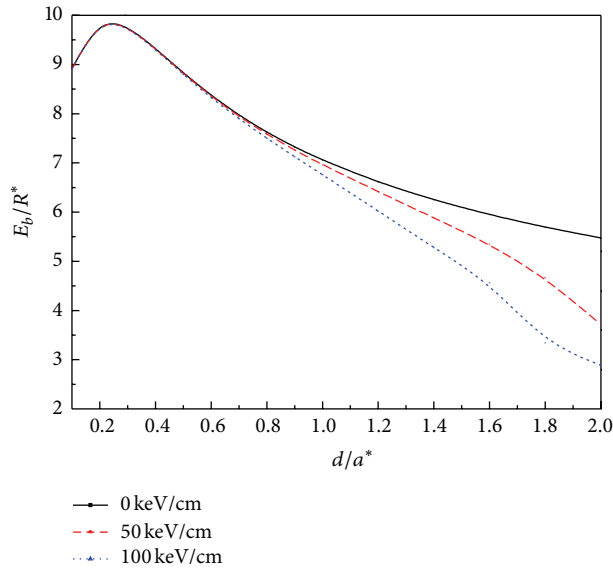


FIGURE 3: Binding energy of a donor impurity in a cylindrical GaAs/Al<sub>x</sub>Ga<sub>1-x</sub>As QR as a function of the QR height for  $R_1 = 0.5a^*$ ,  $R_2 = 3.0a^*$ , and several values of the applied electric field.

### 3. Results and Discussions

The binding energy of a hydrogenic donor impurity was calculated as a function of the impurity position and the applied electric field and the QR structure parameters (radial thickness and height) in the framework of the effective mass approximation and using a variational method. The parameters were chosen in our calculation as follows [8, 22]:  $a^* = 10$  nm,  $R_y^* = 5.72$  meV,  $x = 0.3$ ,  $m_1^* = 0.067m_0$ , and  $m_2^* = (0.067 + 0.083)m_0$ . The results are illustrated in Figures 2–6.

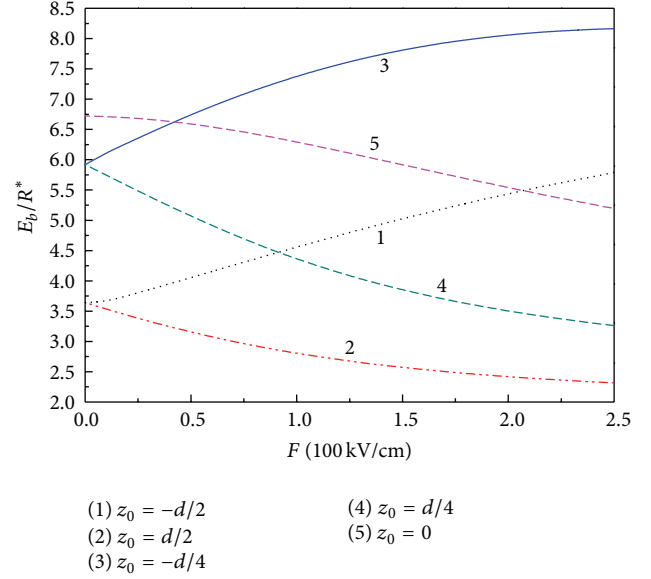


FIGURE 4: Binding energy of a donor impurity in a cylindrical GaAs/Al<sub>x</sub>Ga<sub>1-x</sub>As QR as a function of the applied electric field for  $R_1 = 0.5a^*$ ,  $R_2 = 3.5a^*$ ,  $d = 1.0a^*$ , and five different positions of the donor impurity.

Figure 2 presents the binding energy of a donor impurity as a function of the radial thickness ( $\Delta R$ ) of the QR with the parameters ( $R_1 = 0.3a^*$ ,  $d = 1.0a^*$ ,  $\rho_0 = (R_1 + R_2)/2$ ,  $z_0 = 0.0a^*$ ) and different values of the applied electric field ( $F = 0, 50, 150$  kV/cm). The figure shows that the binding energy of a donor impurity increases with decreasing the radial thickness ( $\Delta R$ ) in all cases, reaches a maximum value, and then decreases sharply. It can be understood that with the strengthening of the size quantization (with the decrease of radial thickness of the QR), the electron cloud moves towards the impurity, the expectation values of the electron-impurity distance increase, and the leakage of electron wave function into surrounded finite barrier region becomes stronger especially for smaller QR radius thickness, thus resulting in a decrease of the binding energy. Figure 2 also displays that the larger the applied electric field is, the smaller the binding energy of a donor impurity placed at the center of the QR is. It is well known that the wave function can be shifted from the impurity ion by the electric field, thus leading to a lower binding energy for a large electric field. This can be explained by the fact that the probability of the electron leaking into barrier region increases greatly and the coulomb confinement action between the electron and the impurity diminishes gradually. It is exciting that the results of the QR are in quite good agreement with those of the quantum dot [27].

Figure 3 displays the binding energy of a donor impurity as a function of the QR height with the parameters ( $R_1 = 0.5a^*$ ,  $R_2 = 3.0a^*$ ,  $\rho_0 = (R_1 + R_2)/2$ ,  $z_0 = 0.0a^*$ ) and different values of the applied electric field ( $F = 0, 50, 100$  kV/cm). The figure shows that the binding energy increases, as the height of the QR is reduced, reaches a maximum value, and then drops slowly for a given value

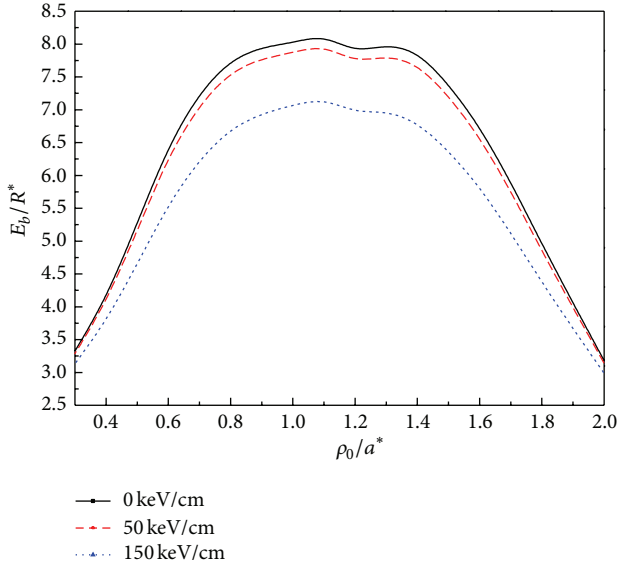


FIGURE 5: Binding energy of a donor impurity in a cylindrical GaAs/Al<sub>x</sub>Ga<sub>1-x</sub>As QR as a function of the impurity radial position  $\rho_0$  for  $R_1 = 0.3a^*$ ,  $R_2 = 2.0a^*$ ,  $d = 1.0a^*$ , and several values of the applied electric field.

of the electric field. As expected, it is because the electron wave function is compressed with decreasing the height of the QR, leading to enhancement of the binding energy [22, 28]. However, below a certain value of the height ( $d$ ), the binding energy starts decreasing until it reaches the bulk value due to leakage of the wave function into the barrier region. It follows that the external electric field has prominent effect on donor binding energy for  $d > 6$  nm and has a little effect on donor binding energy for  $d \leq 6$  nm, which is due to the geometrical or spatial localization, which overcomes the effect of the electric field. As it should be expected, the effect of the electric field is more pronounced for the larger value of the QR height. For the height of the QR  $d \leq 2$  nm, the binding energy drops correspondingly. It is because the probability of the electron leaking into barrier region increases greatly and the coulomb confinement action between the electron and the impurity diminishes gradually.

In Figure 4, the binding energy of a donor impurity in a GaAs/Al<sub>x</sub>Ga<sub>1-x</sub>As QR is presented as a function of the applied electric field for a donor impurity implanted at five values of impurity position  $z = -d/2$  (curve 1),  $z = d/2$  (curve 2),  $z = -d/4$  (curve 3),  $z = d/4$  (curve 4), and  $z = 0$  (curve 5) for the parameters ( $R_1 = 0.5a^*$ ,  $R_2 = 3.5a^*$ ,  $d = 1.0a^*$ ), respectively. It can be clearly seen that the electric field tends to concentrate the electron on one of the sides of the QR. Therefore, the electric field effect may either increase or reduce the binding energy of a donor impurity. The results obtained for the binding energy dependency of external electric field effect are in good agreement with those reported by Duque and coworker [26] concerning density plot of the electron probability cloud for the ground state in the QR. For curve 1 and curve 3, it can be seen that the binding energy of a donor impurity increases monotonically with the increment of the electric field. It is because the probability

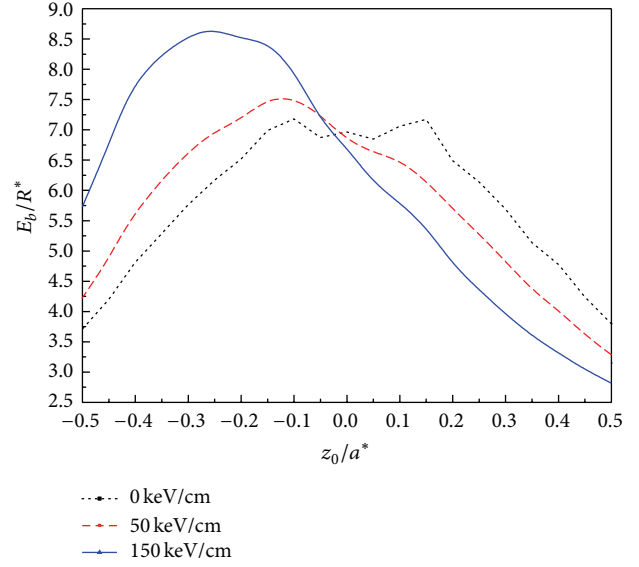


FIGURE 6: Binding energy of a donor impurity in a cylindrical GaAs/Al<sub>x</sub>Ga<sub>1-x</sub>As QR as a function of the axial impurity position  $z_0$  for  $R_1 = 0.4a^*$ ,  $R_2 = 3.0a^*$ ,  $d = 1.0a^*$ , and several values of the applied electric field.

of the electron wave function confined around the impurity ion increases greatly and the Coulomb interaction between the electron and the impurity ion becomes larger with the increase of the applied electric field; the behavior is caused by strengthening the electron confinement because of the stark effect. Curve 2, curve 4, and curve 5 show that the binding energy drops gradually as the electric field becomes large. It is because of the shifting effect of the electric field on the probability densities of the electron wave function, and the increment of the electric field weakens the Coulomb interaction between the electron and the impurity.

Figure 5 presents the binding energy of a donor impurity in a GaAs/Al<sub>x</sub>Ga<sub>1-x</sub>As QR as a function of the radial impurity position  $\rho_0$  with the parameters ( $R_1 = 0.3a^*$ ,  $R_2 = 2.0a^*$ ,  $d = 1.0a^*$ ,  $z_0 = 0.0a^*$ ) and different values of the applied electric field ( $F = 0, 50, 150$  kV/cm). In Figure 5, The curves show that the binding energy firstly increases and then decreases as the radial displacement  $\rho_0$  of the impurity moves from the internal boundary  $R_1$  of the QR to the external boundary  $R_2$ . Taking curve 1, for example, the maximum value of the binding energy is located at the point  $[(R_1 + R_2)/2, 0]$ . The reason is that the electron probability distribution is symmetrical around the axis of the QR ( $\rho_0 = (R_1 + R_2)/2$ ) and the electron wave function is distributed mainly around the axis of the QR. Therefore, the Coulomb interaction between the electron and the impurity becomes the largest, when the impurity is positioned at the middle point of the radial cross-section of the QR. At the same time, the curves also demonstrate that the binding energy of a donor impurity reduces correspondingly with increasing the electric field. As we can expect, the probability of the electron wave function removed from the central along the  $z$ -direction increases greatly, which leads to the reduction of the Coulomb interaction between the electron and the impurity

with the increment of the electric field. The same effect has also been observed for quantum well wires [27].

In Figure 6, the binding energy of a donor impurity is investigated as a function of the impurity position  $z_0$  in  $z$ -direction with the parameters ( $R_1 = 0.4a^*$ ,  $R_2 = 3.0a^*$ ,  $d = 1.0a^*$ ,  $\rho_0 = (R_1 + R_2)/2$ ) and different values of the external electric field ( $F = 0, 50, 150$  kV/cm). It is also seen from Figure 6 that the dot curve for zero applied electric field is absolutely asymmetry, and the binding energy changes irregularly with the impurity axial position  $-1.5 \text{ nm} \leq z_0 \leq 1.5 \text{ nm}$ . The binding energy increases gradually when the impurity is moved from the plane  $z = \pm d/2$  (5 nm) to the symmetry plane  $z = \pm 1.5 \text{ nm}$  along the growth direction of the QR. It is because the topology structure of the QR modifies the spread of the electron wave function in the QR; therefore, the maximum value of the binding energy is not located at the point  $[(R_1 + R_2)/2, 0]$ . The narrower the QR radial thickness is, the more sensitive the irregular change of the maximum binding energy due to the QR special structure is. Our result accords with [16]. From the dash curve and the solid curve, one can see that the binding energy exhibits a maximum with moving the impurity from the plane  $z = -d/2$  to the plane  $z = d/2$  of the QR. In addition, the curves also show that the stronger the applied electric field is, the larger the peak value of the impurity binding energy is with the same parameters ( $d$ ,  $\Delta R$ , and  $\rho_0$ ). Moreover, the position of the peak value of the binding energy is also shifted to negative  $z$  direction. It is because the electronic wave function is obviously modified and the higher concentration of the electron wave function is squeezed strongly around the impurity. In addition, the stronger the applied electronic field is, the bigger the localization effect of the electron wave function is, so that the peak value of the binding energy increases accordingly. Therefore, the distributing of the electron wave function is not central symmetrical about the QR in presence of an electric field.

#### 4. Conclusions

The binding energy of a hydrogenic donor impurity subjected to an external electric field in a GaAs/Al<sub>x</sub>Ga<sub>1-x</sub>As QR with the framework of the effective mass approximation was calculated by using the variational approach. We found that the impurity binding energy depends strongly on ring geometry, applied electric field strength, and impurity position in the finite confinement potential. The binding energy increases firstly, reaches a maximum value, and then drops slowly as the radial thickness and/or the height of the QR decrease. Meanwhile, the binding energy exhibits a maximum as the radial displacement of the impurity moves from the internal boundary  $R_1$  of the QR to the external boundary  $R_2$ . In addition, the position of the peak value of the binding energy is also shifted towards negative  $z$  direction. The electronic wave function distribution is also obviously modified by the applied electric field. Moreover, the stronger the applied electric field is, the larger the peak value of the impurity binding energy is with the same spatial confinement as the impurity position moves along the symmetry axis of

the QR from the bottom of the QR to the top. These theoretical results obtained in this paper are useful for the design of some photoelectric devices constructed based on GaAs/Al<sub>x</sub>Ga<sub>1-x</sub>As QR structures.

#### Acknowledgments

This work was supported by the Scientific and Technological Department Foundation of Hebei Province (no. 12210617), the Young Scientific Research Foundation of Hebei United University (no. z201222), and the Science and Technology Bureau Foundation of Tangshan City in China (no. 12110208a).

#### References

- [1] Y. K. Mishra, V. S. K. Chakravadhanula, V. Hrkac et al., "Crystal growth behaviour in Au-ZnO nanocomposite under different annealing environments and photoswitchability," *Journal of Applied Physics*, vol. 112, no. 6, Article ID 064308, 2012.
- [2] O. Lupan, T. Pauporté, B. Viana et al., "UV-blue and green electroluminescence from Cu-doped ZnO nanorod emitters hydrothermally synthesized on p-GaN," *Journal of Nanoelectronics and Optoelectronics*, vol. 7, no. 7, pp. 712–718, 2012.
- [3] D. Gedamu, I. Paulowicz, S. Jebril, Y. Kumar Mishra, and R. Adelung, "Procedures and properties for a direct nano-micro integration of metal and semiconductor nanowires on Si chips," *Journal of Nanotechnology*, vol. 2012, Article ID 325732, 13 pages, 2012.
- [4] Z. Gong, Z. C. Niu, S. S. Huang, Z. D. Fang, B. Q. Sun, and J. B. Xia, "Formation of GaAs/AlGaAs and InGaAs/GaAs nanorings by droplet molecular-beam epitaxy," *Applied Physics Letters*, vol. 87, no. 9, Article ID 093116, 2005.
- [5] M. DeJarld, K. Reyes, P. Smereka, and J. M. Millunchick, "Mechanisms of ring and island formation in lattice mismatched droplet epitaxy," *Applied Physics Letters*, vol. 102, no. 13, Article ID 133107, 2013.
- [6] M. Abbarchi, L. Cavigli, C. Somaschini et al., "Micro-photoluminescence of GaAs/AlGaAs triple concentric quantum rings," *Nanoscale Research Letters*, vol. 6, article 569, 2011.
- [7] S.-S. Li and J.-B. Xia, "Electronic states of InAs/GaAs quantum ring," *Journal of Applied Physics*, vol. 89, no. 6, pp. 3434–3437, 2001.
- [8] S.-S. Li and J.-B. Xia, "Electronic structures of GaAs/Al<sub>x</sub>Ga<sub>1-x</sub>As quantum double rings," *Nanoscale Research Letters*, vol. 1, no. 2, pp. 167–171, 2006.
- [9] Z. Barticevic, M. Pacheco, and A. Latgé, "Quantum rings under magnetic fields: electronic and optical properties," *Physical Review B*, vol. 62, no. 11, pp. 6963–6966, 2000.
- [10] G. A. Farias, M. H. Degani, J. A. K. Freire, J. Costa E Silva, and R. Ferreira, "Impurities and geometrical effects on the electron energy spectrum of quantum rings," *Physical Review B*, vol. 77, no. 8, Article ID 085316, 2008.
- [11] V. A. Harutyunyan, "Semiconductor nanocylindrical hetero-layer in a radial electrostatic field: the electronic spectrum and optical properties," *Applied Surface Science*, vol. 256, no. 2, pp. 455–459, 2009.
- [12] V. A. Harutyunyan, "Semiconductor nanotube in strong electrostatic field," *Journal of Applied Physics*, vol. 109, no. 1, Article ID 014325, 2011.

- [13] W. Xie, "Absorption spectra of a donor impurity in a quantum ring," *Physica Status Solidi (B) Basic Research*, vol. 246, no. 6, pp. 1313–1317, 2009.
- [14] B. S. Monozon and P. Schmelcher, "Impurity center in a semiconductor quantum ring in the presence of crossed magnetic and electric fields," *Physical Review B*, vol. 67, no. 4, Article ID 045203, 2003.
- [15] B. S. Monozon, M. V. Ivanov, and P. Schmelcher, "Impurity center in a semiconductor quantum ring in the presence of a radial electric field," *Physical Review B*, vol. 70, no. 20, Article ID 205336, 2004.
- [16] A. Bruno-Alfonso and A. Latgé, "Semiconductor quantum rings: shallow-donor levels," *Physical Review B*, vol. 61, no. 23, pp. 15887–15894, 2000.
- [17] M. Aichinger, S. A. Chin, E. Krotscheck, and E. Räsänen, "Effects of geometry and impurities on quantum rings in magnetic fields," *Physical Review B*, vol. 73, no. 19, Article ID 195310, 2006.
- [18] M. G. Barseghyan, M. E. Mora-Ramos, and C. A. Duque, "Hydrostatic pressure, impurity position and electric and magnetic field effects on the binding energy and photo-ionization cross section of a hydrogenic donor impurity in an InAs Pöschl-Teller quantum ring," *European Physical Journal B*, vol. 84, no. 2, pp. 265–271, 2011.
- [19] M. G. Barseghyan, A. Hakimyfar, A. A. Kirakosyan, M. E. Mora-Ramos, and C. A. Duque, "Hydrostatic pressure and electric and magnetic field effects on the binding energy of a hydrogenic donor impurity in InAs Pöschl-Teller quantum ring," *Superlattices and Microstructures*, vol. 51, no. 1, pp. 119–127, 2012.
- [20] H. M. Baghrmian, M. G. Barseghyan, C. A. Duque, and A. A. Kirakosyan, "Binding energy of hydrogenic donor impurity in GaAs/Ga<sub>1-x</sub>Al<sub>x</sub>As concentric double quantum rings: effects of geometry, hydrostatic pressure, temperature, and aluminum concentration," *Physica E*, vol. 48, no. 1, pp. 164–170, 2013.
- [21] A. Zounoubi, I. Zorkani, K. El Messaoudi, and A. Jorio, "Magnetic field effect on the polarizability of shallow donor in cylindrical quantum dot," *Physics Letters A*, vol. 312, no. 3-4, pp. 220–227, 2003.
- [22] G. X. Wang and P. Zhang, "Hydrogenic impurity binding energy in self-assembled GaAs/Ga<sub>1-x</sub>Al<sub>x</sub>As quantum rings," *Journal of Applied Physics*, vol. 103, no. 6, Article ID 063713, 2008.
- [23] D. M. Zheng, Z. C. Wang, and B. Q. Xiao, "Effects of hydrostatic pressure on ionized donor bound exciton states in strained wurtzite GaN/Al<sub>x</sub>Ga<sub>1-x</sub>N cylindrical quantum dots," *Physica B*, vol. 407, no. 1, pp. 4160–4167, 2012.
- [24] J. Lapez-Gondar, J. Dalbuquerque E Castro, and L. E. Oliveira, "Electric-field effects on shallow impurity states in GaAs-(Ga,Al)As quantum wells," *Physical Review B*, vol. 42, no. 11, pp. 7069–7077, 1990.
- [25] J.-H. Pan, L.-Z. Liu, and M. Liu, "Hydrogenic-donor impurity states in GaAs/Al<sub>x</sub>Ga<sub>1-x</sub>As quantum dots in the presence of an electric field," *Chinese Physics Letters*, vol. 28, no. 8, Article ID 086201, 2011.
- [26] C. M. Duque, A. L. Morales, M. E. MoraRamos, and C. A. Duque, "Optical nonlinearities associated to applied electric fields in parabolic two-dimensional quantum rings," *Journal of Luminescence*, vol. 143, no. 1, pp. 81–88, 2011.
- [27] H. Wang, L. Jiang, Q. Gong, and S. Feng, "External electric field effect on the hydrogenic donor impurity in zinc-blende InGaN/GaN cylindrical quantum well wire," *Physica B*, vol. 405, no. 18, pp. 3818–3821, 2010.
- [28] G. X. Wang, X. Z. Duan, and L. Y. Ai, "Hydrogenic donor impurity states of quantum ring in the presence of an electric field," in *Proceedings of the IEEE Symposium on Electrical & Electronics Engineering (EEESYM '12)*, vol. 1, pp. 738–741, 2012.

## Research Article

# Light Output Enhancement of InGaN/GaN Light-Emitting Diodes with Contrasting Indium Tin-Oxide Nanopatterned Structures

Sang Hyun Jung,<sup>1,2</sup> Keun Man Song,<sup>1</sup> Young Su Choi,<sup>1</sup> Hyeong-Ho Park,<sup>1</sup>  
Hyun-Beom Shin,<sup>1</sup> Ho Kwan Kang,<sup>1</sup> and Jaejin Lee<sup>2</sup>

<sup>1</sup>Nano Process Division, Korea Advanced Nano Fab. Center, Suwon, Kyeonggi 443-270, Republic of Korea

<sup>2</sup>Department of Electrical and Computer Engineering, Ajou University, Suwon, Kyeonggi 443-749, Republic of Korea

Correspondence should be addressed to Ho Kwan Kang; [hokwan.kang@kanc.re.kr](mailto:hokwan.kang@kanc.re.kr) and Jaejin Lee; [jaejin@ajou.ac.kr](mailto:jaejin@ajou.ac.kr)

Received 12 April 2013; Revised 9 July 2013; Accepted 9 July 2013

Academic Editor: M. Reza Bayati

Copyright © 2013 Sang Hyun Jung et al. This is an open access article distributed under the Creative Commons Attribution License, which permits unrestricted use, distribution, and reproduction in any medium, provided the original work is properly cited.

Various nanopatterns on the transparent conducting indium tin oxide (ITO) layer are investigated to enhance the light extraction efficiency of the InGaN/GaN light-emitting diodes (LEDs). Triangular, square, and circular nanohole patterns with the square and hexagonal lattices are fabricated on the ITO layer by an electron beam lithography and inductively coupled plasma dry etching processes. The circular hole pattern with a hexagonal geometry is found to be the most effective among the studied structures. Light output intensity measurements reveal that the circular hole nanopatterned ITO LEDs with a hexagonal lattice show up to 35.6% enhancement of output intensity compared to the sample without nanopatterns.

## 1. Introduction

In recent years, InGaN/GaN light-emitting diodes (LEDs) have been used in many applications such as general white lightening, traffic signals, automobile head lights, and back light units of liquid crystal display [1]. Although InGaN/GaN LEDs are being commercially available, it is still necessary to further improve the light extraction efficiency and the internal quantum efficiency for the realization of the high-efficiency and high-power LEDs. There are many methods to improve the efficiency of the InGaN/GaN LEDs such as substrate design, metal reflection layer, distributed Bragg reflector, omnidirectional reflector, truncated-inverted-pyramid chip geometry, nanopatterning, transparent substrate, surface texturing, and laser lift off [2–10]. In addition, the surface texturing or patterning of a p-type transparent conducting layer has been demonstrated to be effective for enhancing light extraction efficiency [11–18]. In the previous works, Pan et al. conducted photolithography and dry etching to fabricate the InGaN/GaN LEDs with a 3  $\mu\text{m}$  square surface-textured ITO [15]. With the textured ITO surface, they achieved 16% output power enhancement compared to the

planar ITO LEDs. Also, Chang et al. reported nitride-based LEDs with an ITO electrode, patterned by an imprint lithography and dry etching [11]. It was found that the LED output power for nanopatterned ITO LEDs with 0.85  $\mu\text{m}$  holes was about 12 and 8% higher than that of the planar ITO LEDs and micropatterned ITO LEDs with 1.75  $\mu\text{m}$  holes, respectively. Such a result suggested that submicron-sized holes can scatter light more effectively. It is thus worth investigating the nanopatterned structure and geometry on the ITO layer of the GaN-based LEDs for achieving the higher light extraction efficiency. Nanopatterning technique has attracted great attentions for more efficient light extraction from the LED structure and various methods are explored. Most of researches have been focused on the influences of periods and hole depths of the nanopatterns on the properties of the LEDs [11, 12, 18]. There are few studies on the light output enhancement by various geometry and shapes of the nanopatterned structure on the transparent conducting oxide layer of the LEDs. In this study, we report the light output analysis of the InGaN/GaN LEDs with varying geometric lattices and hole shapes fabricated on a transparent ITO layer.

## 2. Experiments

GaN-based LED structures were grown on sapphire substrates by metalorganic vapor phase epitaxy (MOVPE, AIXTRON, G3 2600HT). For the growth of GaN, trimethylgallium (TMGa) and ammonia ( $\text{NH}_3$ ) were used as the reactant sources for Ga and N, respectively. Silane ( $\text{SiH}_4$ ) and bis(cyclopentadienyl) magnesium ( $\text{Cp}_2\text{Mg}$ ) were used as n- and p-type dopants, respectively. A 30 nm thick GaN nucleation layer was grown on a sapphire substrate and followed by 2  $\mu\text{m}$  thick undoped GaN buffer, 3  $\mu\text{m}$  thick Si-doped n-GaN layer, InGaN/GaN multiple quantum wells (MQWs), and 0.15  $\mu\text{m}$  thick Mg-doped p-GaN layer. The MQWs region consists of 3 nm thick InGaN wells and 10 nm thick GaN barriers.

To fabricate 1  $\text{mm}^2$  LED devices, mesa etching was carried out by a standard photolithography and inductively coupled plasma etching processes. A 200 nm thick ITO was deposited on top of the p-GaN surface as a transparent conducting layer using an electron beam evaporator, followed by annealing at 550°C under the  $\text{N}_2$  flow for 4 min to obtain a good p-ohmic contact. After the deposition of Cr/Au for an n-type contact, chip isolation was carried out by a standard photolithography and inductively coupled plasma etchings.

Triangular, square, and circular hole nanopatterns with the square and hexagonal lattices are generated by Layout Editor (L-EDIT, TANNER), which is the gds file generation program. To create the nanopatterns on the ITO layer, the GaN-based LED wafer was coated with 400 nm thick ZEP-520A (ZEON), which is a positive-type electron beam resist. The square and hexagonal nanopatterned structures with various shaped holes including triangle, square, and circle were patterned using a 100 kV electron beam lithography machine (JBX9300FS of JEOL). After the electron beam exposure, electron beam resist was developed by dipping in ZED-N50 (ZEON), rinsed in isopropyl alcohol (IPA), and blown with a  $\text{N}_2$  dry gun.

The samples then were etched by an inductively coupled plasma dry etcher (STS, MULTIPLEX LITE ICP System) using a  $\text{Cl}_2/\text{CF}_4$  gas mixture. The electron beam resist on the etched LED wafer was removed by microwave asher (ULVAC, ENVIRO II) in the mixed  $\text{O}_2$  and  $\text{N}_2\text{H}_2$  gas conditions. Figure 1(a) schematically describes the diagram of the LED chip structure with a patterned ITO surface. The microscopic image of the top view of the fabricated LED chip with a nanopatterned ITO is shown in Figure 1(b). The patterned samples were examined by a field emission scanning electron microscopy (FE-SEM, HITACHI, S-4800). Electroluminescence (EL), current-voltage ( $I$ - $V$ ), and light output-current ( $L$ - $I$ ) measurements were carried out using an in-line LED tester (WITHLIGHT, OPI-150). The diameter of the photodetector and the distance between the photodetector and LEDs are 11 and 60 mm, respectively, in the EL measurement conditions.

## 3. Results and Discussion

The design parameters of the nanopatterns for an ITO layer are summarized in Table 1. The shapes of the nanopatterns consist of triangle, square, and circle with either square or

TABLE 1: The lattice and dimension of the nanopatterns fabricated on the ITO layer by an electron beam lithography.

Nanopatterns	Lattice	Pattern shape	X pitch (nm)	Y pitch (nm)	Pattern dimension (nm)
ST		Triangle	400	400	304
SS	Square	Square	400	400	200
SC		Circle	400	400	226
HT		Triangle	400	693	283
HS	Hexagonal	Square	400	693	186
HC		Circle	400	693	210

hexagonal lattices for comparison study of shape and geometry dependencies on the InGaN/GaN LEDs performances. We designed six different types of nanopatterns, which are square lattice triangular (ST), square lattice square (SS), square lattice circular (SC), hexagonal lattice triangular (HT), hexagonal lattice square (HS), and hexagonal lattice circular hole (HC). The coverage of nanopatterned area is fixed at 25% by controlling the length and pitch of the nanopatterns. The dimensions of the triangular, square, and circular holes are 304, 200, and 226 nm, respectively, with a 400 nm pitched square lattice. In case of the hexagonal lattice, X and Y pitches are 400 and 693 nm, respectively, and the dimensions of the triangular, square, and circular holes are 283, 186, and 210 nm, respectively. Scanning electron microscopy (SEM) images of the fabricated nanopatterns with varying hole-shapes and lattices are displayed in Figure 2. The etched depth of the ITO layer on the LEDs is 70 nm.

Figure 3 shows the injection current versus voltage ( $I$ - $V$ ) characteristics of the nanopatterned ITO LEDs. Under 20 mA current injection, it was measured that forward voltage for the conventional ITO LED is 2.95 V and that of the nanopatterned ITO LED with the ST, SS, SC, HT, HS, and HC hole structures is 3.03, 3.02, 3.02, 3.00, 3.01, and 2.99 V, respectively. It also reveals that the nanopatterned ITO electrode causes a slight increase of operating voltage. The slightly higher forward voltage could result from the dry etching damage to the ITO layer, which affects the sheet resistances and current spreading [13].

Figure 4 shows the light output versus injection current ( $L$ - $I$ ) characteristics of the nanopatterned ITO LEDs. The output power increased with the injection current and no intensity saturation was observed up to 100 mA for all the nanopatterned LEDs. It was also found that the highest output power is achieved from the nanopatterned ITO LED with an HC hole structure. For the 20 mA injection current, the LED output powers are 3.25, 3.61, 3.87, 4.03, 3.77, 4.03, and 4.40 mW for the conventional ITO LED, nanopatterned ITO LED with the ST, SS, SC, HT, HS, and HC hole structures, respectively. Table 2 summarizes the relative light output intensity increments of the samples with the different nanopatterns. The light output intensities of the nanopatterned ITO LEDs with the ST, SS, SC, HT, HS, and HC hole structures increase by 11.0, 19.1, 24.2, 16.2, 24.1, and 35.6%, respectively, compared to the one without

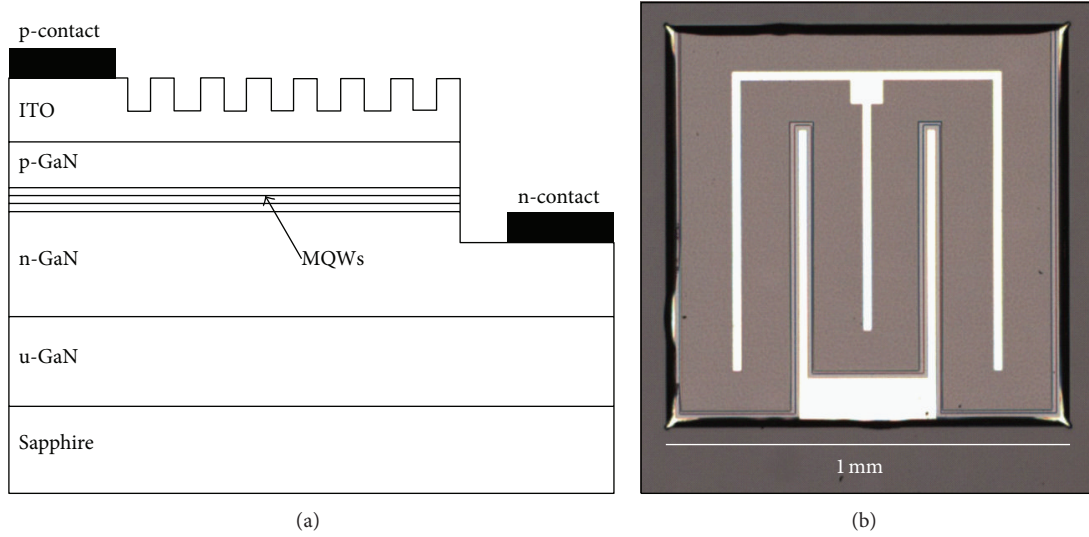


FIGURE 1: (a) Schematic diagram of the InGaN/GaN LED structure and (b) top-view microscopic image of the fabricated ITO LED chip with nanopatterns.

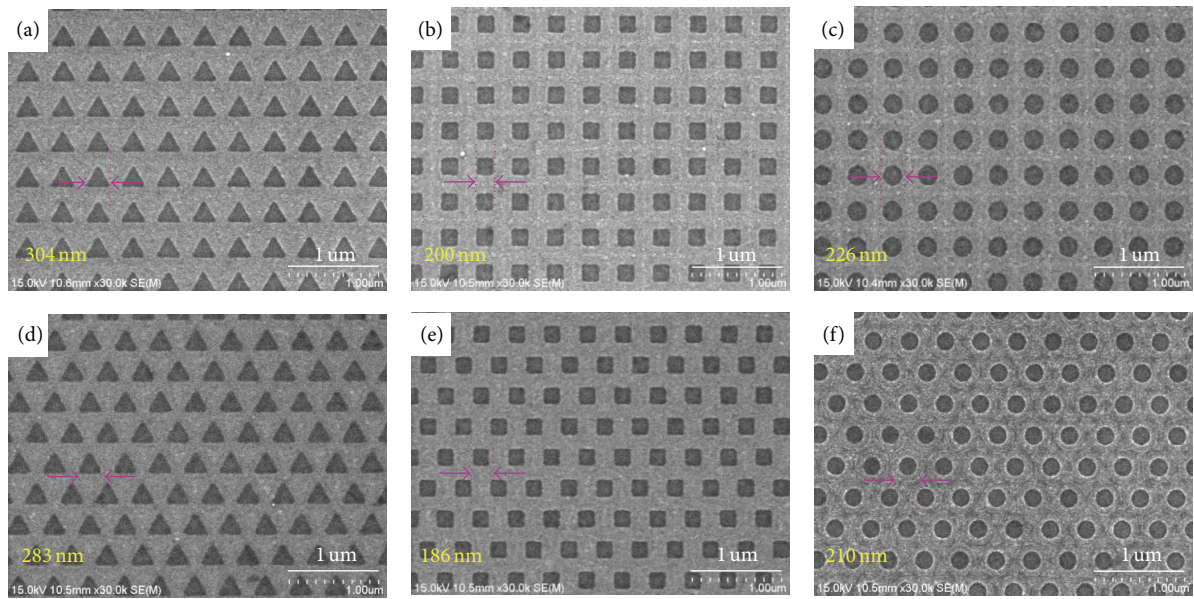


FIGURE 2: SEM images of the (a) triangular, (b) square, and (c) circular holes with the square lattice and (d) triangular, (e) square, and (f) circular holes with the hexagonal lattice on the ITO layer.

the nanopatterns. According to Snell's law, the critical angle of the total internal reflection at air/ITO interface is around  $29^\circ$ , assuming the refractive index of the ITO to be 2.06 at 437 nm wavelength. Thus, a significant amount of photon will be reflected at the sample surface for conventional ITO LEDs. The nanopatterned ITO layer results in the formation of large sidewalls, with which some of the reflected light may escape through the sidewall air/ITO interfaces, resulting in additional light extraction and, in turn, enhancement of the light output power. The more efficient relative light output intensity in the nanopatterned LEDs may be attributed to the improvement of the spontaneous Purcell emission rate [7].

TABLE 2: The relative light output increment of the InGaN/GaN LEDs with a nanopatterned ITO layer.

Lattice type	Relative increment of light output intensity (%)		
	Triangular holes	Square holes	Circular holes
Square	11.0	19.1	24.2
Hexagonal	16.2	24.1	35.6

As shown in Figure 4 and Table 2, circular hole pattern on the ITO layer is measured to be more effective in enhancing the light extraction efficiency than the square and triangular

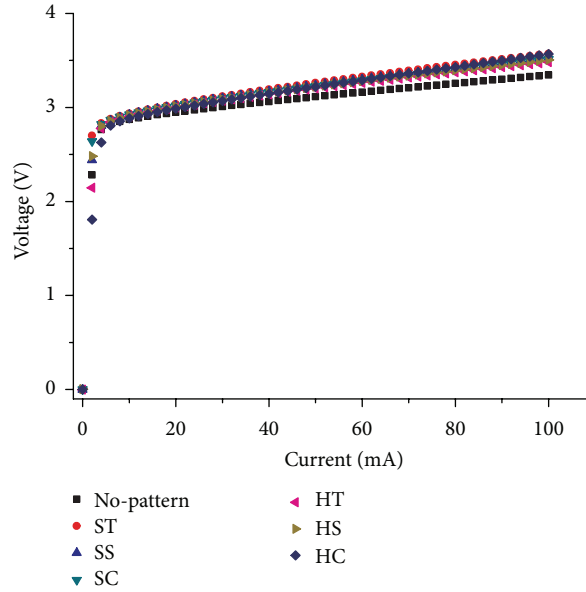


FIGURE 3: Voltage versus current characteristics of the nanopatterned ITO LEDs at room temperature.

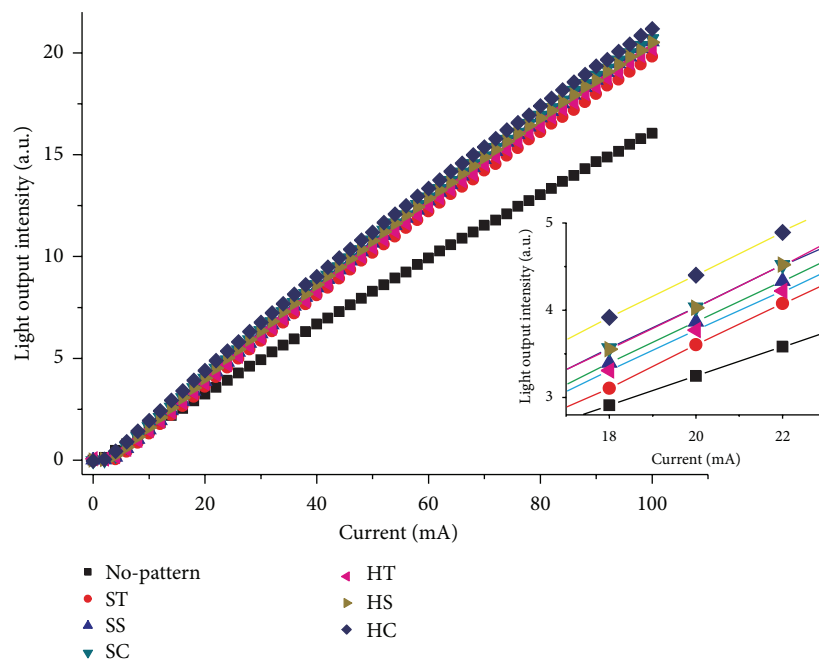


FIGURE 4: Light output versus injection current ( $L-I$ ) characteristics of the nanopatterned ITO LEDs at room temperature. The inset shows light output versus injection current ( $L-I$ ) characteristics at 20 mA injection current.

hole-patterns. Photons generated in the multiple quantum well (MQW) regions may escape more efficiently at the ITO/air sidewall interfaces through the circular hole patterns due to the unfolded side surface areas. Furthermore, the light output of the LEDs with the nanopatterned ITO with a hexagonal lattice is greater than those with the square lattice because the number of hole patterns per unit ITO area of hexagonal lattice is higher than that of square lattice.

Figure 5 shows the room temperature EL spectra of the nanopatterned ITO LED at 20 mA injection current. EL

intensities of the LEDs with the nanopatterned ITO layer are measured to be significantly increased compared to the one without the nanopatterns. The EL intensity of the nanopatterned ITO LEDs with the HC hole structures increases by 35.6% compared to the one without the nanopatterns. Our results for the HC structures with  $0.21 \mu\text{m}$  holes show better EL intensity enhancement compared to the previously reported 12% EL enhancement from the nanopatterned ITO LEDs with  $0.85 \mu\text{m}$  holes [11]. It could be attributed to the increment of the number of hole patterns per unit ITO area by

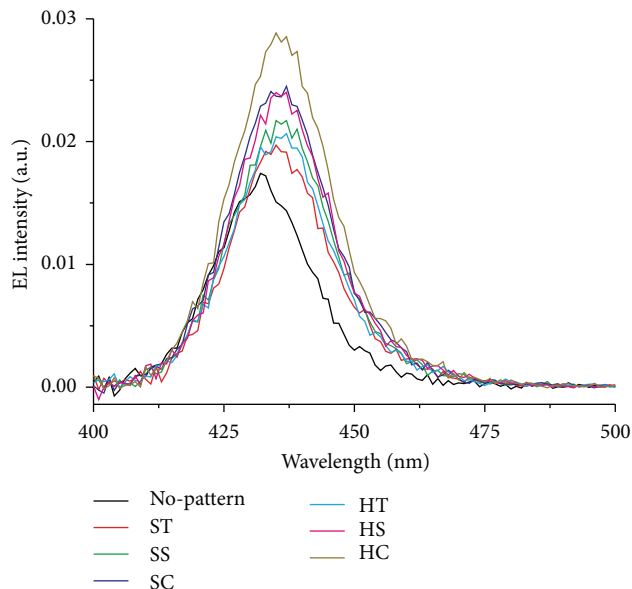


FIGURE 5: EL spectra of the nanopatterned ITO LEDs at room temperature.

the smaller hole pattern, which scatters light more efficiently than the larger hole pattern. The circular nanopatterned ITO LEDs with the hexagonal lattice show the highest enhancement of the EL intensity, consistent with the results from the light output intensity current measurements. The possibility of vertical penetration of photons at the ITO/air hole interfaces is enhanced by the increased surface areas of the circular hole patterns in comparison with the other square and triangular hole patterns. Furthermore, the EL intensity of the LEDs with the nanopatterned ITO with a hexagonal lattice is greater than those with the square lattice. Because the number of hole patterns per unit ITO area of the hexagonal lattice is larger than that of the square lattice, the circular nanopatterned ITO LEDs with the hexagonal lattice show the greatest EL intensity enhancement. The main EL emission peak of the nanopatterned ITO LEDs is measured to be red-shifted; for example, the main peak emission for the nanopatterned ITO LEDs with an HC hole structure was observed at 437 nm, while that of the conventional ITO LEDs was measured at 432 nm. It is known that the main EL emission peak of the InGa<sub>N</sub>/Ga<sub>N</sub> LEDs with a nanopatterned ITO layer shifts to a longer wavelength compared to the non-patterned ITO LEDs due to the Joule heating effect [19]. This could be attributed to the increased surface areas of the patterned ITO layer, resulting in more heat dissipation through the increased surface.

#### 4. Conclusions

Various nanopatterns have been fabricated on the transparent conducting ITO layer of the InGa<sub>N</sub>/Ga<sub>N</sub> LEDs by the electron beam lithography and inductively coupled plasma dry etching process. It is found that the InGa<sub>N</sub>/Ga<sub>N</sub> LEDs fabricated with the nanopatterned ITO layer produce a higher

light output power than the sample with the planar ITO electrodes. The circular hole pattern with a hexagonal geometry is found to be the most effective among the tested structures. The light output intensity of the hexagonal lattice with the circular hole patterns on the ITO layer of the InGa<sub>N</sub>/Ga<sub>N</sub> LED showed an enhancement of 35.6% over that of the conventional LED with a planar ITO at 20 mA injection current.

#### Conflict of Interests

The authors declare no competing financial interests.

#### Acknowledgment

This work is supported by the National Research Foundation Grants (Midcareer Researcher Program: 2009-0083803 and KRF-2007-331-D00250).

#### References

- [1] N. Narendran, Y. Gu, J. P. Freyssonier-Nova, and Y. Zhu, "Extracting phosphor-scattered photons to improve white LED efficiency," *Physica Status Solidi A*, vol. 202, no. 6, pp. R60–R62, 2005.
- [2] T. Nishida, H. Saito, and N. Kobayashi, "Efficient and high-power AlGa<sub>N</sub>-based ultraviolet light-emitting diode grown on bulk Ga<sub>N</sub>," *Applied Physics Letters*, vol. 79, no. 6, pp. 711–712, 2001.
- [3] T. Gessmann and E. F. Schubert, "High-efficiency AlGaInP light-emitting diodes for solid-state lighting applications," *Journal of Applied Physics*, vol. 95, no. 5, pp. 2203–2216, 2004.
- [4] D. A. Steigerwald, J. C. Bhat, D. Collins et al., "Illumination with solid state lighting technology," *IEEE Journal on Selected Topics in Quantum Electronics*, vol. 8, no. 2, pp. 310–320, 2002.
- [5] C.-F. Chu, F.-I. Lai, J.-T. Chu et al., "Study of Ga<sub>N</sub> light-emitting diodes fabricated by laser lift-off technique," *Journal of Applied Physics*, vol. 95, no. 8, pp. 3916–3922, 2004.
- [6] S. Noda, M. Fujita, and T. Asano, "Spontaneous-emission control by photonic crystals and nanocavities," *Nature Photonics*, vol. 1, no. 8, pp. 449–458, 2007.
- [7] T. N. Oder, J. Shakya, J. Y. Lin, and H. X. Jiang, "III-nitride photonic crystals," *Applied Physics Letters*, vol. 83, no. 6, pp. 1231–1233, 2003.
- [8] T. N. Oder, K. H. Kim, J. Y. Lin, and H. X. Jiang, "III-nitride blue and ultraviolet photonic crystal light emitting diodes," *Applied Physics Letters*, vol. 84, no. 4, pp. 466–468, 2004.
- [9] J. J. Wierer, M. R. Krames, J. E. Epler et al., "InGa<sub>N</sub>/Ga<sub>N</sub> quantum-well heterostructure light-emitting diodes employing photonic crystal structures," *Applied Physics Letters*, vol. 84, no. 19, pp. 3885–3887, 2004.
- [10] S.-F. Yu, S.-P. Chang, S.-J. Chang, R.-M. Lin, H.-H. Wu, and W.-C. Hsu, "Characteristics of InGa<sub>N</sub>-based light-emitting diodes on patterned sapphire Substrates with various pattern heights," *Journal of Nanomaterials*, vol. 2012, Article ID 346915, 6 pages, 2012.
- [11] S. J. Chang, C. F. Shen, W. S. Chen et al., "Nitride-based light emitting diodes with indium tin oxide electrode patterned by imprint lithography," *Applied Physics Letters*, vol. 91, no. 1, Article ID 013504, 2007.
- [12] X. Zhang, S. Liu, Y. Liu, X. Chen, H. Lin, and X. Ren, "Enhancement of LED light extraction via diffraction of hexagonal lattice

- fabricated in ITO layer with holographic lithography and wet etching,” *Physics Letters A*, vol. 372, no. 20, pp. 3738–3740, 2008.
- [13] D.-S. Leem, T. Lee, and T.-Y. Seong, “Enhancement of the light output of GaN-based light-emitting diodes with surface-patterned ITO electrodes by maskless wet-etching,” *Solid-State Electronics*, vol. 51, no. 5, pp. 793–796, 2007.
- [14] M. Yamada, T. Mitani, Y. Narukawa et al., “InGaN-based near-ultraviolet and blue-light-emitting diodes with high external quantum efficiency using a patterned sapphire substrate and a mesh electrode,” *Japanese Journal of Applied Physics*, vol. 41, no. 2, pp. L1431–L1433, 2002.
- [15] S.-M. Pan, R.-C. Tu, Y.-M. Fan, R.-C. Yeh, and J.-T. Hsu, “Improvement of InGaN-GaN light-emitting diodes with surface-textured indium-tin-oxide transparent ohmic contacts,” *IEEE Photonics Technology Letters*, vol. 15, no. 5, pp. 649–651, 2003.
- [16] P. Uthirakumar, J. H. Kang, B. D. Ryu, H. G. Kim, H. K. Kim, and C.-H. Hong, “Nanoscale ITO/ZnO layer-texturing for high-efficiency InGaN/GaN light emitting diodes,” *Materials Science and Engineering B*, vol. 166, no. 3, pp. 230–234, 2010.
- [17] D.-S. Leem, T. Lee, and T.-Y. Seong, “Enhancement of the light output of GaN-based light-emitting diodes with surface-patterned ITO electrodes by maskless wet-etching,” *Solid-State Electronics*, vol. 51, no. 5, pp. 793–796, 2007.
- [18] K.-M. Yoon, K.-Y. Yang, K.-J. Byeon, and H. Lee, “Enhancement of light extraction in GaN based LED structures using TiO<sub>2</sub> nano-structures,” *Solid-State Electronics*, vol. 54, no. 4, pp. 484–487, 2010.
- [19] X. A. Cao and S. D. Arthur, “High-power and reliable operation of vertical light-emitting diodes on bulk GaN,” *Applied Physics Letters*, vol. 85, no. 18, pp. 3971–3973, 2004.

## Research Article

# Low-Temperature Rapid Fabrication of ZnO Nanowire UV Sensor Array by Laser-Induced Local Hydrothermal Growth

**Sukjoon Hong, Junyeob Yeo, Wanit Manrotkul, Gunho Kim, Jinhyeong Kwon, Kunsik An, and Seung Hwan Ko**

*Applied Nano Tech and Science Lab, KI for Nano Century, Graduate School of (Energy Environment Water and Sustainability) EEWS, Korea Advanced Institute of Science and Technology (KAIST), 291 Daehak-ro, Yuseong-gu, Daejeon 305-701, Republic of Korea*

Correspondence should be addressed to Seung Hwan Ko; [maxko@kaist.ac.kr](mailto:maxko@kaist.ac.kr)

Received 12 April 2013; Accepted 28 June 2013

Academic Editor: Naeimeh Naseri

Copyright © 2013 Sukjoon Hong et al. This is an open access article distributed under the Creative Commons Attribution License, which permits unrestricted use, distribution, and reproduction in any medium, provided the original work is properly cited.

We demonstrate ZnO nanowire based UV sensor by laser-induced hydrothermal growth of ZnO nanowire. By inducing a localized temperature rise using focused laser, ZnO nanowire array at  $\sim 15 \mu\text{m}$  size consists of individual nanowires with  $\sim 8 \mu\text{m}$  length and 200–400 nm diameter is readily synthesized on gold electrode within 30 min at the desired position. The laser-induced growth process is consecutively applied on two different points to bridge the micron gap between the electrodes. The resultant photoconductive ZnO NW interconnections display 2–3 orders increase in the current upon the UV exposure at a fixed voltage bias. It is also confirmed that the amount of photocurrent can be easily adjusted by changing the number of ZnO NW array junctions. The device exhibits clear response to the repeated UV illumination, suggesting that this process can be usefully applied for the facile fabrication of low-cost UV sensor array.

## 1. Introduction

1D nanostructures, or nanowires (NWs), have been studied extensively for the future application in diverse areas including optoelectronics [1, 2], energy harvesting devices [3, 4], and sensors [5–9] due to its large surface-to-volume ratio and other unique properties. Among various materials, ZnO NW can be employed usefully for sensor applications because of its high on/off ratio [10] and low cost fabrication [11], and the related studies reported that ZnO NW can detect the change in pressure [5], humidity [6], gas concentration [7], UV illumination [12–14], and even biomolecular interactions [8]. Menzel et al. also reported a ZnO NW based multifunctional sensor [9] which can detect temperature, UV exposure, and pH change in a single platform.

For the fabrication of conventional ZnO NW based sensor having metal-semiconductor-metal (MSM) configuration, ZnO NW is firstly grown in tube furnace by chemical vapor deposition (CVD) method [15] which requires a very high temperature of around 1000°C. The grown ZnO NW is then harvested and transferred to the target substrate, followed by e-beam lithography and evaporation [16] in

order to form electrodes that capture two ends of the NW for further electrical characterization. These two aspects—high temperature for the NW synthesis and difficult technique for capturing the NW with electrode layer—have been remained as big problems for the facile fabrication of ZnO NW based sensors. Recent studies on ZnO NW based sensor [12–14] attempt to utilize the ZnO NW grown by hydrothermal method which can be conducted in very low-temperature ( $<100^\circ\text{C}$ ) compared to other CVD methods such as vapor-solid [17] (VS) or vapor-liquid-solid [18] (VLS); yet hydrothermally grown ZnO NW also has to pass through the same steps required for the NWs grown using CVD methods. Swanwick et al. [13] reported symmetric and antisymmetric ZnO NW near-UV sensor using low temperature hydrothermal growth without any further lithographic process after the growth; yet it required a careful design of the substrate and an extra sputtering step for ZnO layer. For the substitution of e-beam lithography process, numerous efforts have been made for the facile positioning of ZnO NW on the premade electrode layer using different techniques such as direct printing [19] and dielectrophoresis [12]. These methods,

however, often remain unwanted NWs at the unintended region of the substrate that lower the reliability of the process.

In this study, we propose laser-induced hydrothermal growth of ZnO NW for the facile fabrication of ZnO NW based UV sensor. For a conventional hydrothermal bulk growth of ZnO NW, a seeded substrate, either using ZnO nanoparticles [11] (NPs) or zinc acetate [20], is immersed in precursor solution that contains zinc ions and capping agents at elevated temperature for several hours to induce further anisotropic growth. Instead of heating the whole substrate, a focused laser has been utilized as a localized heater to raise the temperature locally and synthesize the NWs only at the desired position. By applying this process on two different points in sequence, ZnO NW network consist of photoconductive NW junctions that bridges the gap between two pads can be readily produced without any additional lithographic process or complicated aligning techniques. We demonstrated that the resultant ZnO NW junction shows clear response to the UV exposure, so that this process can be effectively utilized for the fabrication of ZnO NW based sensor applications.

## 2. Experimental

**2.1. ZnO Seed Preparation.** 30 mL of 30 mM NaOH solution in ethanol is added slowly to 60 mL of 10 mM zinc acetate dehydrate ( $\text{Zn}(\text{OAc})_2$ ) in ethanol. The reaction is continued for 2 hour at 60°C with a gentle stirring. The solution, after the complete reaction, is cooled to room temperature and stored in the refrigerator. The resultant synthesized ZnO NPs are 5–10 nm in diameter with quasi-spherical shape. For the seeding, the solution is dropped and spread on the target substrate, followed by washing out with fresh ethanol after several seconds before its complete dry. This coating step is repeated 3~4 times to ensure the complete coverage of ZnO NPs on the substrate. By coating ZnO NP layer on the substrate, the growth of ZnO NW can be initiated from the adhered ZnO NPs (“seeds”) without going through homogeneous nucleation step [21].

**2.2. ZnO Precursor Solution Preparation.** 25 mM of zinc nitrate hexahydrate ( $\text{Zn}(\text{NO}_3)_2 \cdot 6\text{H}_2\text{O}$ ) and 25 mM of hexamethylenetetramine (HMTA,  $\text{C}_6\text{H}_{12}\text{N}_4$ ) are dissolved in DI water, and 5~7 mM of polyethylenimine (PEI,  $\text{C}_2\text{H}_5\text{N}$ ) is added for further hindrance of lateral growth. The solution is then heated at 95°C for 1h and cooled to room temperature, whereas the white precipitates produced during the heating process are filtered out afterwards. The resultant precursor solution is transparent with yellowish color.

**2.3. Laser-Induced Hydrothermal Growth of ZnO NW.** The overall process of laser-induced hydrothermal growth is depicted in Figure 1. The substrate initially goes through the seeding step as explained in Section 2.1. A small PDMS chamber is placed on top of the sample and filled with the precursor solution (details in Section 2.2). The opening of the chamber is then blocked with a cover glass to prevent any undesirable optical disturbances such as solvent evaporation.

The laser beam is focused on the sample through an optical system to generate a local temperature field at the sample.

532 nm continuous wave (CW) Nd:YAG laser is used as the optical source, and a half-wave plate (HWP), together with a polarized beam splitter (PBS), is located after the mechanical shutter in order to control the laser power by rotating the polarization state and passing the vertical polarization only [22, 23]. Another 50:50 beam splitter is placed subsequently for the real-time measurement of the laser power. The laser beam is focused by using commercial objective lens (5X), and the laser power is adjusted in the range of 60~150 mW in order to find the optimum power that generates the proper temperature field for the ZnO NW growth. Two CCD modules are located on both sides to constitute a dual inverted microscope system for the in situ monitoring of the entire growth process.

**2.4. Fabrication of ZnO NW Based UV Sensor Using Laser-Induced Hydrothermal Growth.** The electrode layer with two pads separated by sub-10  $\mu\text{m}$  gap is deposited on a glass wafer in advance of the laser-induced hydrothermal growth process. The electrode layer not only provides the external interconnections for the electrical characterization but also acts as a uniform light-absorbing layer for the temperature rise. The ZnO NW array is grown at the edges of two pads as shown in Figure 5(a). The laser power and growth time for each point is fixed to be 120 mW and 15 min.

**2.5. Characterization.** All the electrical characterizations are conducted in probe station having 4 axis micromanipulators in a dark faraday cage. The IV curve and photocurrent time evolution are measured by a semiconductor analyzer, where the UV lamp has the peak power at 365 nm wavelength with 350  $\mu\text{W}/\text{cm}^2$  power. The optical, SEM, and TEM images are acquired for characterization.

## 3. Results and Discussion

**3.1. Laser-Induced Hydrothermal Growth of ZnO NW.** The growth of ZnO NWs on gold coated glass wafer can be detected from CCD camera within several minutes when the laser power exceeds ~60 mW. We searched for the highest possible laser power for the synthesis of longer NW by generating extended temperature field. However, since the temperature rise happens in liquid environment, laser power that exceeds a certain threshold value induces a temperature that is higher than the boiling point of the solvent and creates a bubble which destroys the previously grown NW array. For the current optical configuration, a bubble easily appears at 150 mW, and thus the laser power is fixed to be 120 mW, unless stated otherwise, for sufficiently efficient but stable growth condition. Figure 2(a) shows the typical outcome of ZnO NW array produced by laser-induced hydrothermal growth process when the laser is focused at a single point using 5X objective lens for 30 min. The temperature induced by the focused laser spot is the largest at the center due to the Gaussian profile of the laser beam, and thus the length of individual NW is the maximum at the middle of the array. The

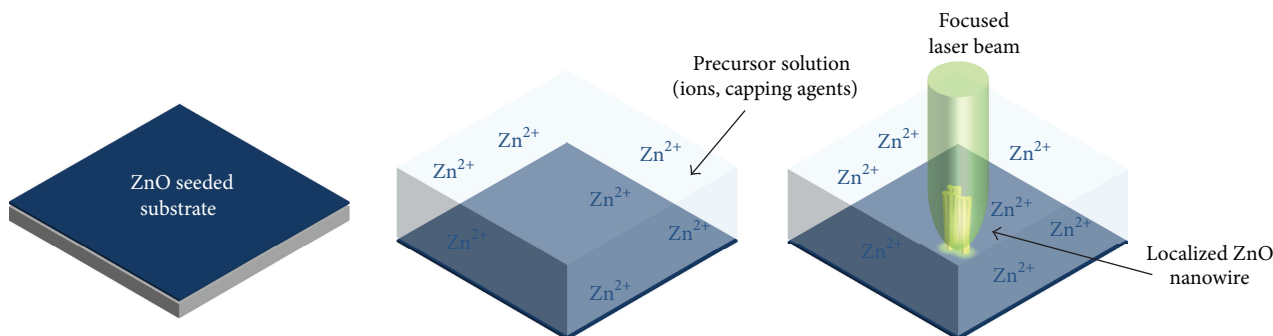


FIGURE 1: Schematic illustration of laser-induced hydrothermal growth process. The target substrate is seeded with ZnO NP, and immersed in the precursor solution. The laser is then focused on the sample surface to generate a confined temperature field to induce localized synthesis of ZnO NW.

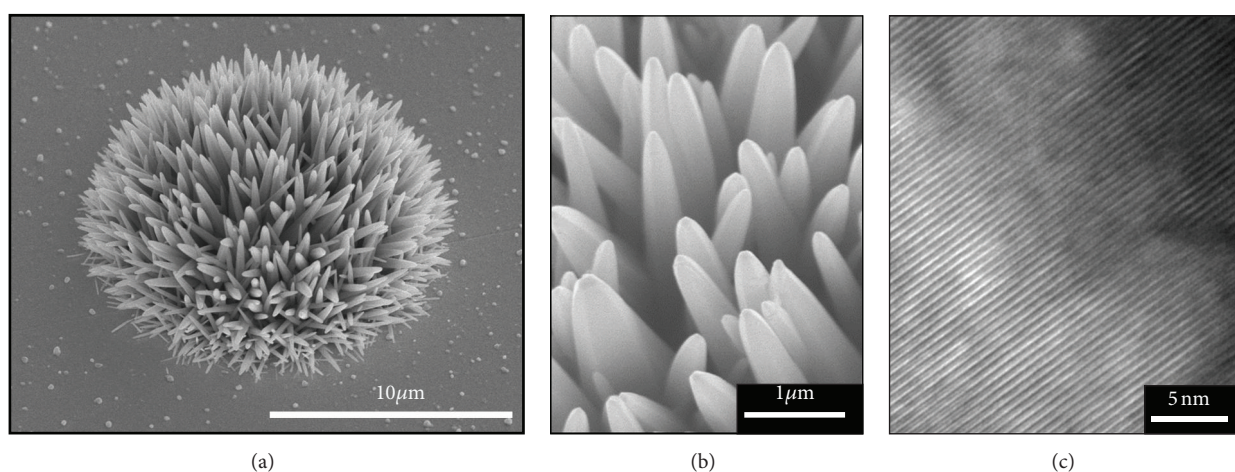
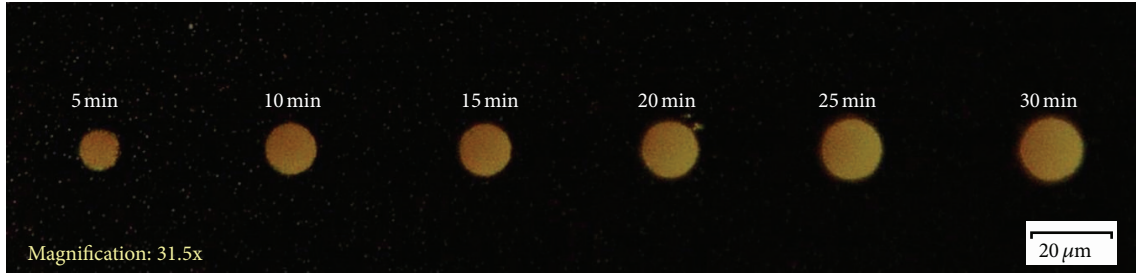


FIGURE 2: ZnO NW array synthesized using laser-induced hydrothermal growth at 120 mW power for 30 min using 5X objective lens. (a) SEM image of ZnO NW array synthesized by laser-induced hydrothermal growth. ZnO NW array consists of individual NWs facing radial direction with  $\sim 8\mu\text{m}$  and length, is synthesized only at the laser spot. (b) SEM image of ZnO NW array with higher magnification. Distinct facets are observable, while the thickness of each NW is  $200\sim 400\text{nm}$ . (c) TEM image of a single ZnO NW, showing the lattice arrangement along  $c$ -axis.

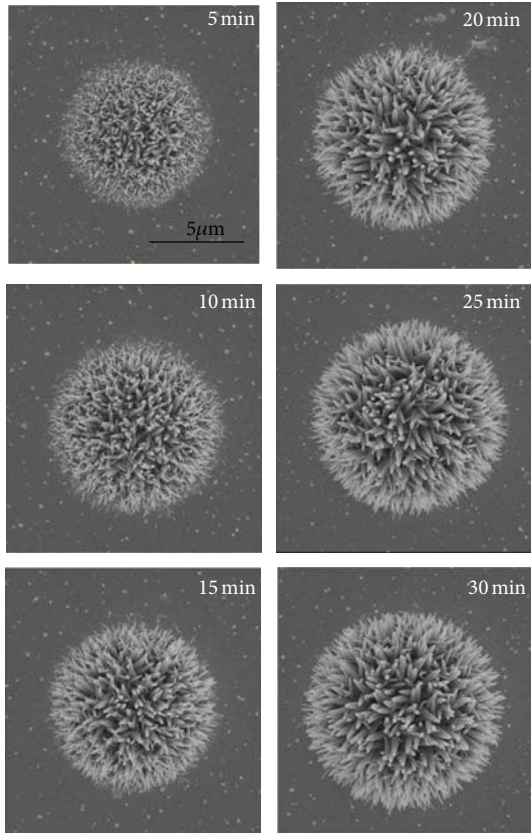
size of the resultant ZnO NW array ( $\sim 15\mu\text{m}$ ) is considerably larger than the estimated laser spot size ( $\sim 10\mu\text{m}$ ) since the NWs at the edge are grown at more oblique angle to expand the lateral dimension of the array. These NWs grown at oblique angles are favorable for the fabrication of UV sensor as shown in Figure 5(a). From the magnified SEM image in Figure 2(b), distinct facets of ZnO NW due to the wurtzite crystal structure can be confirmed. The lateral dimension of each NW is around  $200\sim 400\text{nm}$ , and its crystalline nature is noticeable in TEM image in Figure 2(c), showing its  $c$ -axis with the lattice constant of  $0.52\text{nm}$ .

The dark-field optical image and the corresponding SEM image for different growth time (5 min, 10 min, 15 min, 20 min, 25 min, and 30 min) are shown in Figures 3(a) and 3(b). The increase in the overall array size according to the elapsed growth time is apparent in both optical and SEM images. An interesting point is that the growth rate of laser-induced growth is much faster than that of the conventional bulk hydrothermal growth. For the conventional bulk growth

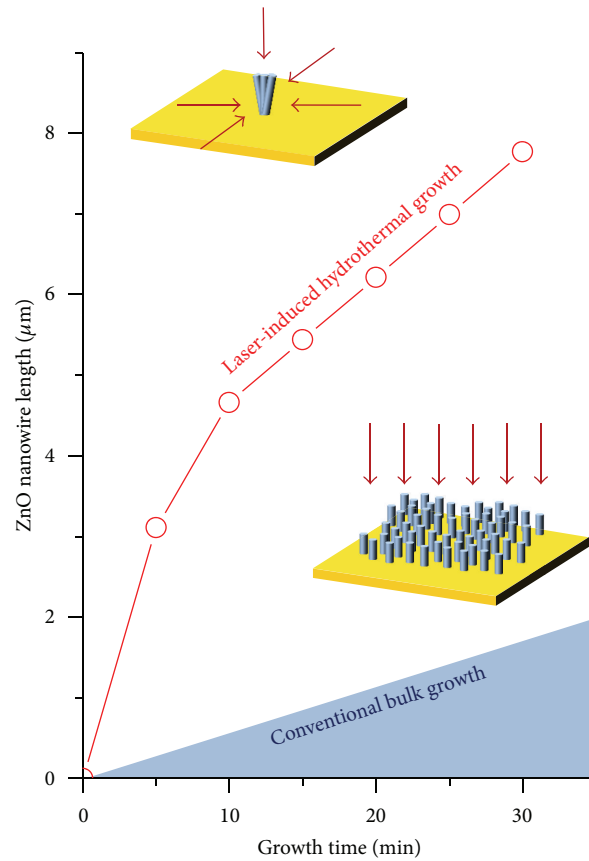
using the same precursor solution, the growth speed is normally bounded to  $\sim 2\mu\text{m/hr}$ . Recent studies on preferential growth [24] availed the growth speed to be as high as  $\sim 5\mu\text{m/hr}$  by adding different chemical compounds, but the growth rate of laser-induced growth easily exceeds  $10\mu\text{m/hr}$  and even reaches  $20\mu\text{m/hr}$  at higher laser power. Such rapid growth is considered to be originated from three different reasons [22]. Firstly, the overall concentration remains almost unchanged for the laser-induced hydrothermal growth process. For the conventional bulk hydrothermal growth, the length of NW grows asymptotically since the zinc precursor in the solution is constantly consumed in the course of growth process. As a result, the precursor solution has to be refreshed for the further growth. In contrary, the consumption of zinc precursor, in terms of total amount, is almost negligible for the laser growth, and thus the zinc precursor can be continuously supplied to the growth spot. Secondly, the zinc precursor is supplied from single direction in the case of conventional bulk growth; however, the zinc precursor can



(a)



(b)



(c)

FIGURE 3: (a) Optical images of ZnO NW array grown using laser-induced hydrothermal growth for 5 min, 10 min, 15 min, 20 min, and 25 min and 30 min and (b) the corresponding SEM images. (c) Plot of the ZnO NW length at different growth time. It is noticeable that the growth rate of laser-induced hydrothermal process is much faster than the conventional bulk growth.

reach the growth spot from all radial direction for laser-induced growth as shown in the inset of Figure 3(c). Thirdly, the natural convection due to the temperature gradient might be also beneficial for the zinc precursor supply. These two properties of laser-induced growth—localized synthesis only at the desired position and rapid growth speed—are both advantageous for the facile fabrication of ZnO NW based sensor [23].

**3.2. ZnO NW Based UV Sensor.** It is well-known that ZnO NW changes its conductivity upon UV illumination [23, 25] as its working mechanism is illustrated in Figure 4.

A depletion region is formed at the surface of ZnO NW in the dark because the oxygen molecules are adsorbed on the surface by capturing the free electrons in the n-type semiconductor. When the UV light that exceeds the bandgap of ZnO is illuminated to the ZnO NW, electron-hole pairs are generated, and the holes migrate to the surface due to the potential slope. The oxygen molecule is then detached from the surface by capturing the hole, while the remaining electron contributes to the conductivity. The current therefore typically increases upon the UV exposure at a fixed voltage bias.

By applying laser-induced hydrothermal growth twice, the gap between two pads can be interconnected with UV

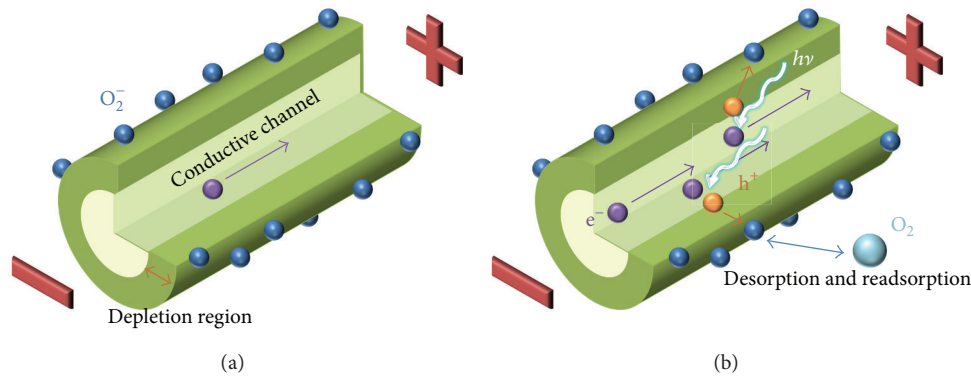


FIGURE 4: Schematics on the mechanism of ZnO NW based UV sensor. (a) In the dark, oxygen molecules are adsorbed on the surface of ZnO NW by capturing the free electrons in n-type semiconductor. (b) Upon the UV illumination, electron-hole pairs are generated, and the oxygen molecules are detached from the surface by taking the holes. The remaining electrons contribute to the increase in conductivity.

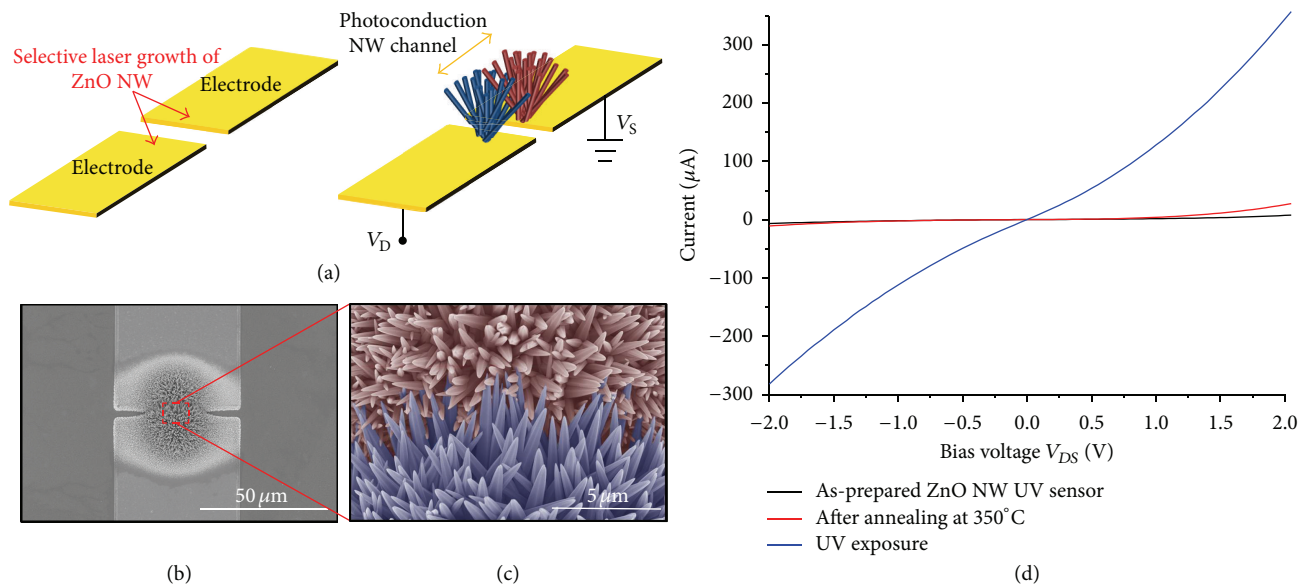


FIGURE 5: (a) Schematic of ZnO NW based UV sensor fabricated by laser induced hydrothermal growth. ZnO NW array is grown selectively at the two edges of the electrodes by applying laser-induced growth twice. The resultant ZnO NW arrays form interconnecting ZnO NWs whose conductance changes upon UV illumination. (b) SEM image of the resultant ZnO NW based UV sensor (c) SEM image at higher magnification. It is noticeable that the NWs grown from different electrodes come into contact with each other. (d) *IV* curves of as-prepared device, the device after annealing process and the same device upon UV illumination.

sensitive NW channel. The schematic diagram is shown in Figure 5(a), whereas the ZnO NW based UV sensor with the similar configurations can be found in the previous studies [9, 26] as well. It can be confirmed from the SEM image in Figure 5(b) that the grown ZnO NW has sufficient length to bridge the gap between two pads. The high magnification SEM image in Figure 5(c) shows that the individual NWs are contacted to form photoconductive ZnO NW channel. After the application of laser-induced hydrothermal growth, the device is annealed at  $350^\circ\text{C}$  for 10 min [27]. The *IV* curves before and after the annealing process are plotted in Figure 5(d), and the device shows subtle difference upon the annealing process, possibly due to the polymer removal at the surface. While on the other hand, the current under the

UV illumination increases significantly by 2 to 3 orders of magnitude, which is comparable to the value acquired from single ZnO NW [25]. Such huge difference in current upon the UV illumination makes our device suitable for the UV detection.

The *IV* curves in Figure 5(d) are not completely ohmic, but somewhat nonlinear and asymmetrical, showing diode-like characteristics. The electrical behavior of ZnO NW in metal-semiconductor-metal configuration is still under debate, and previous studies have shown that the ZnO NW can either form ohmic contact [25] or Schottky barrier [12], although the configurations are not completely the same. The origin of schottky barrier has been described by numerous explanations. The intrinsic property of ZnO NW seems to

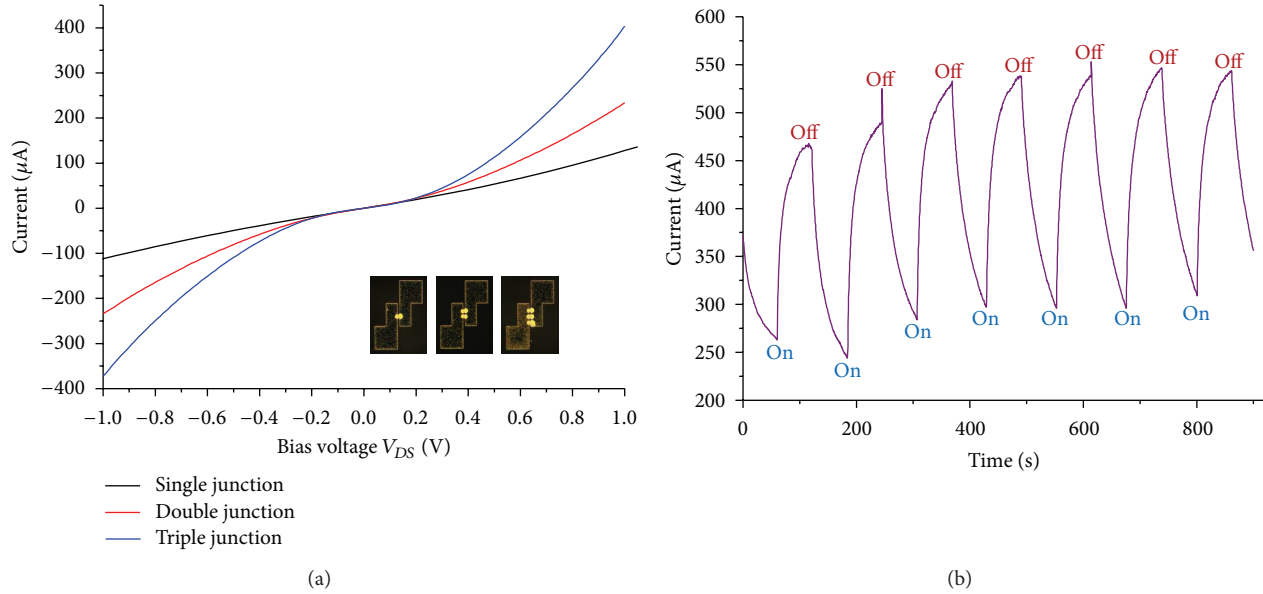


FIGURE 6: (a)  $IV$  curves of the ZnO NW based UV sensors with single, double, and triple junctions. The current increases almost linearly with the number of junctions. (b) Time evolution of the current when the UV illumination is switched on and off for every 60 seconds at a fixed bias voltage.

be responsible for the asymmetry in  $IV$  curve in the first place, since the alternating zinc and oxygen layers of ZnO NW can influence the symmetry of  $IV$  curve by providing dipole moment [12]. The process concerned for the fabrication of MSM configuration, such as electrode deposition or dielectrophoresis, can also contribute to the formation of the schottky barrier by providing different fixations, contact areas, and annealing conditions at both ends of the NW [16, 28]. It is reported that the properties of the schottky barrier is actually adjustable by intentional modulation of barrier height and width using different contacting metal layers for each end of the NW [28]. Furthermore, the transformation of ohmic contact into schottky barrier, or vice versa, is possible as well through various methods such as laser irradiation, bending, or annealing [29]. The electrical properties of the current device are also expected to be controllable by various methods to yield the optimum characteristics for sensing applications.

It is worth mentioning that the amount of photocurrent even at low bias voltage is relatively high for the UV sensor fabricated by laser-induced hydrothermal growth process due to the densely grown ZnO NW at the growth spot. High photoresponse can be measured without any high-precision measurement system, so that the overall cost of the sensor can be reduced [19]. The photocurrent can be further adjusted by controlling the number of ZnO NW array network junction digitally. Figure 6(a) shows the  $IV$  curves upon the UV exposure when single, double, and triple ZnO NW array junctions are synthesized between two pads by applying laser-induced growth 2, 4, and 6 times. The optical images of each device are shown in the inset. We can confirm that the current increases almost linearly with the number of the junctions.

Figure 6(b) shows the photocurrent of the UV sensor with triple junction when the UV illumination is switched on and

off for every 60 seconds. The device presents clear response to the UV exposure; however, its saturation characteristics are not fully perceived. The rising and decay times are estimated from fitting a biexponential function. For the current device, the rising times are 4.2 s and 29.32 s, while two decaying times are 4.41 s and 38.6 s. These values are comparable to the similar device fabricated with a dielectrophoretic method, [30] and much smaller than the recovery time of the UV sensor based on ZnO thin film [19]. The high magnified SEM image in Figure 5(c) shows that the NWs grown from two pads almost agglomerate and start to lose their properties as individual NWs. Therefore, the response and recovery time are expected to be reduced further by shortening the growth time.

## 4. Conclusion

We introduced laser-induced hydrothermal growth process in order to grow ZnO NW array rapidly at a desire position without any high temperature or vacuum environment. By controlling the laser power and irradiation time, ZnO NW arrays were easily integrated to the premade electrode layers to constitute photoconductive channel by bridging the gap between two electrode pads to demonstrate UV sensor. The resultant UV sensor displayed clear response to the UV exposure, showing that this process has a high potential for the facile fabrication of low-cost ZnO NW based UV sensor.

## Acknowledgments

This work is supported by National Research Foundation of Korea (NRF) (Grant nos. 2012-0008779, 2012-0003722), Global Frontier R&D-Program on Center for Multiscale

Energy System (Grant no. 2012-054172) under the Ministry of Science, ICT & Future, Korea, and the cooperative R&D Program (Grant no. B551179-10-01-00) on the Korea Research Council Industrial Science and Technology.

## References

- [1] M. H. Huang, S. Mao, H. Feick et al., "Room-temperature ultraviolet nanowire nanolasers," *Science*, vol. 292, no. 5523, pp. 1897–1899, 2001.
- [2] H. W. Kang, J. Yeo, J. O. Hwang et al., "Simple ZnO nanowires patterned growth by microcontact printing for high performance field emission device," *Journal of Physical Chemistry C*, vol. 115, no. 23, pp. 11435–11441, 2011.
- [3] M. Law, L. E. Greene, J. C. Johnson, R. Saykally, and P. Yang, "Nanowire dye-sensitized solar cells," *Nature Materials*, vol. 4, no. 6, pp. 455–459, 2005.
- [4] S. Xu, Y. Qin, C. Xu, Y. Wei, R. Yang, and Z. L. Wang, "Self-powered nanowire devices," *Nature Nanotechnology*, vol. 5, no. 5, pp. 366–373, 2010.
- [5] X. Wang, J. Zhou, J. Song, J. Liu, N. Xu, and Z. L. Wang, "Piezoelectric field effect transistor and nanoforce sensor based on a single ZnO nanowire," *Nano Letters*, vol. 6, no. 12, pp. 2768–2772, 2006.
- [6] Y. Zhang, K. Yu, D. Jiang, Z. Zhu, H. Geng, and L. Luo, "Zinc oxide nanorod and nanowire for humidity sensor," *Applied Surface Science*, vol. 242, no. 1–2, pp. 212–217, 2005.
- [7] S. N. Das, J. P. Kar, J. H. Choi, T. I. Lee, K. J. Moon, and J. M. Myoung, "Fabrication and characterization of ZnO single nanowire-based hydrogen sensor," *Journal of Physical Chemistry C*, vol. 114, no. 3, pp. 1689–1693, 2010.
- [8] A. Choi, K. Kim, H. Jung, and S. Y. Lee, "ZnO nanowire biosensors for detection of biomolecular interactions in enhancement mode," *Sensors and Actuators B*, vol. 148, no. 2, pp. 577–582, 2010.
- [9] A. Menzel, K. Subannajui, F. Güder, D. Moser, O. Paul, and M. Zacharias, "Multifunctional ZnO-nanowire-based sensor," *Advanced Functional Materials*, vol. 21, no. 22, pp. 4342–4348, 2011.
- [10] C. S. Lao, M. C. Park, Q. Kuang et al., "Giant enhancement in UV response of ZnO nanobelts by polymer surface-functionalization," *Journal of the American Chemical Society*, vol. 129, no. 40, pp. 12096–12097, 2007.
- [11] L. E. Greene, M. Law, J. Goldberger et al., "Low-temperature wafer-scale production of ZnO nanowire arrays," *Angewandte Chemie—International Edition*, vol. 42, no. 26, pp. 3031–3034, 2003.
- [12] O. Harnack, C. Pacholski, H. Weller, A. Yasuda, and J. M. Wessels, "Rectifying behavior of electrically aligned ZnO nanorods," *Nano Letters*, vol. 3, no. 8, pp. 1097–1101, 2003.
- [13] M. E. Swanwick, S. M. L. Pfaendler, A. I. Akinwande, and A. J. Flewitt, "Near-ultraviolet zinc oxide nanowire sensor using low temperature hydrothermal growth," *Nanotechnology*, vol. 23, no. 34, Article ID 344009, 2012.
- [14] N. Liu, G. Fang, W. Zeng et al., "Direct growth of lateral ZnO nanorod UV photodetectors with schottky contact by a single-step hydrothermal reaction," *ACS Applied Materials and Interfaces*, vol. 2, no. 7, pp. 1973–1979, 2010.
- [15] Y. C. Kong, D. P. Yu, B. Zhang, W. Fang, and S. Q. Feng, "Ultraviolet-emitting ZnO nanowires synthesized by a physical vapor deposition approach," *Applied Physics Letters*, vol. 78, no. 4, pp. 407–409, 2001.
- [16] Z. M. Liao, J. Xu, J. M. Zhang, and D. P. Yu, "Photovoltaic effect and charge storage in single ZnO nanowires," *Applied Physics Letters*, vol. 93, no. 2, Article ID 023111, 3 pages, 2008.
- [17] K. H. Lee, S. W. Lee, R. R. Vanfleet, and W. Sigmund, "Amorphous silica nanowires grown by the vapor-solid mechanism," *Chemical Physics Letters*, vol. 376, no. 3–4, pp. 498–503, 2003.
- [18] R. S. Wagner and W. C. Ellis, "Vapor-liquid-solid mechanism of single crystal growth," *Applied Physics Letters*, vol. 4, no. 5, pp. 89–90, 1964.
- [19] S. Bai, W. Wu, Y. Qin, N. Cui, D. J. Bayerl, and X. Wang, "High-performance integrated ZnO nanowire UV sensors on rigid and flexible substrates," *Advanced Functional Materials*, vol. 21, no. 23, pp. 4464–4469, 2011.
- [20] L. E. Greene, M. Law, D. H. Tan et al., "General route to vertical ZnO nanowire arrays using textured ZnO seeds," *Nano Letters*, vol. 5, no. 7, pp. 1231–1236, 2005.
- [21] S. Xu and Z. L. Wang, "One-dimensional ZnO nanostructures: solution growth and functional properties," *Nano Research*, vol. 4, no. 11, pp. 1013–1098, 2011.
- [22] J. Yeo, S. Hong, M. Wanit et al., "Rapid, one-step, digital selective growth of ZnO nanowires on 3D structures using laser induced hydrothermal growth," *Advanced Functional Materials*, vol. 23, no. 26, pp. 3316–3323, 2013.
- [23] S. Hong, J. Yeo, W. Manorotkul et al., "Digital selective growth of a ZnO nanowire array by large scale laser decomposition of zinc acetate," *Nanoscale*, vol. 5, no. 9, pp. 3698–3703, 2013.
- [24] C. Xu, P. Shin, L. Cao, and D. Gao, "Preferential growth of long ZnO nanowire array and its application in dye-sensitized solar cells," *Journal of Physical Chemistry C*, vol. 114, no. 1, pp. 125–129, 2010.
- [25] C. Soci, A. Zhang, B. Xiang et al., "ZnO nanowire UV photodetectors with high internal gain," *Nano Letters*, vol. 7, no. 4, pp. 1003–1009, 2007.
- [26] Y. Li, F. D. Valle, M. Simonnet, I. Yamada, and J. J. Delaunay, "High-performance UV detector made of ultra-long ZnO bridging nanowires," *Nanotechnology*, vol. 20, no. 4, Article ID 045501, 2009.
- [27] S. H. Ko, D. Lee, H. W. Kang et al., "Nanoforest of hydrothermally grown hierarchical ZnO nanowires for a high efficiency dye-sensitized solar cell," *Nano Letters*, vol. 11, no. 2, pp. 666–671, 2011.
- [28] C. S. Lao, J. Liu, P. Gao et al., "ZnO nanobelt/nanowire schottky diodes formed by dielectrophoresis alignment across Au electrodes," *Nano Letters*, vol. 6, no. 2, pp. 263–266, 2006.
- [29] Y. Hu, Y. Chang, P. Fei, R. L. Snyder, and Z. L. Wang, "Designing the electric transport characteristics of ZnO micro/nanowire devices by coupling piezoelectric and photoexcitation effects," *ACS Nano*, vol. 4, no. 2, pp. 1234–1240, 2010.
- [30] L. Guo, H. Zhang, D. Zhao et al., "High responsivity ZnO nanowires based UV detector fabricated by the dielectrophoresis method," *Sensors and Actuators B*, vol. 166–167, pp. 12–16, 2012.

## Research Article

# Simulation of an Improved Design for n-Electrode with Holes for Thin-GaN Light-Emitting Diodes

Farn-Shiun Hwu

*Department of Mechanical Engineering, Taoyuan Innovation Institute of Technology, Jhongli 32091, Taiwan*

Correspondence should be addressed to Farn-Shiun Hwu; [hfs@tiit.edu.tw](mailto:hfs@tiit.edu.tw)

Received 26 March 2013; Revised 10 June 2013; Accepted 10 June 2013

Academic Editor: Yogendra Mishra

Copyright © 2013 Farn-Shiun Hwu. This is an open access article distributed under the Creative Commons Attribution License, which permits unrestricted use, distribution, and reproduction in any medium, provided the original work is properly cited.

A novel design is proposed for n-electrode with holes to be applied in Thin-GaN light-emitting diodes (LEDs). The influence of the n-electrode with holes on the thermal and electrical characteristics of a Thin-GaN LED chip is investigated using a three-dimensional numerical simulation. The variations in current density and temperature distributions in the active layer of n-electrodes both with and without holes are very tiny. The percentages of light output from these holes are 29.8% and 38.5% for cases with 5  $\mu\text{m}$  holes and 10  $\mu\text{m}$  holes, respectively; the side length of the n-electrode (L) is 200  $\mu\text{m}$ . Furthermore, the percentage increases with the size of the n-electrode. Thus, the light output can be increased 2.45 times using the n-electrode with holes design. The wall-plug efficiency (WPE) can also be improved from 2.3% to 5.7%. The most appropriate n-electrode and hole sizes are determined by WPE analysis.

## 1. Introduction

Light-emitting diodes have many advantages over conventional light sources, such as their narrow spectrum, long lifetime, and good mechanical stability [1, 2]. High-brightness LEDs have been proven to have excellent abilities to function in back and general lighting applications [3]. There are two major methods that can be used to increase the light output of an LED chip: enlarging the area of a single LED chip or manufacturing a monolithic LED chip array [4, 5]. When the area of an LED chip is enlarged, it results in an increase in the input current and the heat dissipation. Several methods have been developed to improve the current distribution and heat transfer in LED chips by means of altering the design of the electrode pattern and the geometry of the structure [6–9]. The Thin-GaN LED has also been demonstrated to have great potential for high-power illumination usage [8, 10–12]. The better current spreading and superior heat dissipation of the Thin-GaN LED allow it to operate under higher power conditions. A better design for the electrode pattern can increase the light-emitting ratio and decrease the thermal burden in the Thin-GaN LED [1]. The current distribution in an LED chip is usually estimated from the light output [8, 10] and is affected by the material properties of the chip, as well as

the size and pattern of the electrode [8, 10–12]. The current crowding effect can be improved by the insertion of the current blocking layer (CBL) in the epitaxial structure of the Thin-GaN LED [8]. Many different LED chip structures have been designed and fabricated in the search for superior LED performance [1, 4, 8, 13]. Several studies have investigated the fabrication and performance of blue/near-UV LEDs composed of an array of nanowires on a p- or n-GaN thin film substrate [14–16]. The problem is that the mass fabrication procedure for LEDs is expensive and time consuming.

Several numerical models have been proposed to explain the phenomenon of current spreading and to find possible ways to obtain better device geometry for LEDs [1, 5, 9, 17–19]. Tu et al. improved the design of the n-electrode patterns to obtain more uniform current spreading [1]. Hwang and Shim [20] developed a three-dimensional numerical simulation model, based on the concept of series and parallel connections, with which to investigate current spreading in an LED. The continuity equation for electronic transport can be used in three-dimensional models to simulate the electric potential and current in lateral-injection LED chips. This has proven to be much more economical than other methods [9, 17]. Using this approach, the simulation of complex LED structures

becomes possible. The influence of the thermal effect on the performance of the LED has been considered in some studies [8, 10, 11, 13, 20, 21]. In our previous study, a numerical model, which considered the thermal effect, was proposed for simulating a vertical LED chip [22]. The simulation results for different areas of the n-electrode and the influence of CBL were discussed. The results were found to be consistent with the experimental results obtained in the study of Kim et al. [8].

The main problem with Thin-GaN LEDs is the shadowing effect of the n-electrode when current crowding under the n-electrode is serious. Recently, a novel n-electrode with holes has been manufactured with wet etching technology to solve this problem. In the present study, we modify the 3D numerical model developed in our previous work [22] to simulate the influence of the n-electrode with holes. This method is used to investigate the thermal and electrical characteristics of Thin-GaN LED chips operating under high-power conditions. The effects of the hole size are considered. In addition, the wall-plug efficiency (WPE) is also discussed in our numerical model.

## 2. Numerical Simulation

A Thin-GaN LED chip is analyzed in the present study. A schematic representation of a cross section in the lateral direction is shown in Figure 1. The full chip dimensions are  $600 \times 600 \mu\text{m}^2$ . The thicknesses of the n-type GaN layer, active layer, and p-type GaN layer are 2.5, 0.07, and  $0.07 \mu\text{m}$ , respectively. A p-type electrode is formed by the application of a  $0.93 \mu\text{m}$  thick Ag/Ni/Au metalized layer to the entire wafer ( $600 \times 600 \mu\text{m}^2$ ). The n-type electrode is formed by the application of a  $0.7 \mu\text{m}$  thick Ti/Au metalized layer with various square dimensions and different widths ( $L = 100, 200, 300, 400, 500, \text{ and } 600 \mu\text{m}$ ).

The continuity equation for electronic transport in an LED chip is

$$\nabla \cdot (\sigma \nabla V) = 0, \quad (1)$$

where  $\sigma$  is the conductivity and  $V$  is the electrical potential. The resistivities of the n- and p-type cladding layers are  $\rho_n = 1 \times 10^{-2} \Omega \cdot \text{cm}$  and  $\rho_p = 14 \Omega \cdot \text{cm}$ , respectively; and the other resistivities for the metallic electrode are  $\rho_{\text{Ag}} = 1.59 \times 10^{-6} \Omega \cdot \text{cm}$ ,  $\rho_{\text{Ni}} = 6.9 \times 10^{-6} \Omega \cdot \text{cm}$ ,  $\rho_{\text{Au}} = 2 \times 10^{-6} \Omega \cdot \text{cm}$ , and  $\rho_{\text{Ti}} = 4.2 \times 10^{-5} \Omega \cdot \text{cm}$ . The specific p-contact resistance and the specific n-contact resistance are set to be  $2.8 \times 10^{-3} \Omega \cdot \text{cm}^2$  and  $3.6 \times 10^{-4} \Omega \cdot \text{cm}^2$ , respectively, [8]. Following upon our previous work [22], the current through the active layer is assumed to move in the direction perpendicular to the layer. The equation for calculating the electrical potential in the LED is solved using the finite-element method (FEM). The equivalent conductivity for each element in the active layer is calculated by

$$\sigma = \frac{l_e}{V_j} \cdot J_e, \quad (2)$$

where  $l_e$  is the elemental thickness of the mesh;  $V_j$  is the voltage drop between the active layer; and  $J_e$  is the elemental

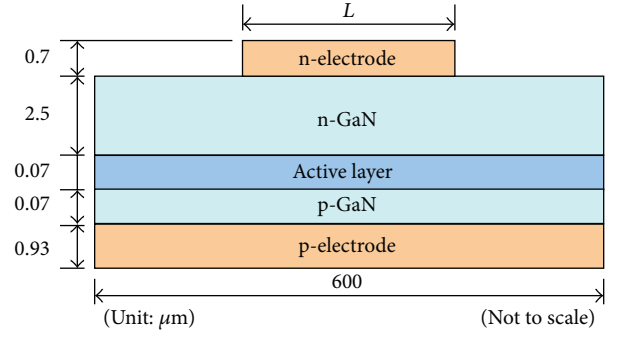


FIGURE 1: A cross-sectional schematic representation of a Thin-GaN LED chip in the lateral direction, where  $L$  represents the size of the n-electrode.

current density [23]. The current behavior through the active layer of the LED chip is dominated by the following Shockley equation:

$$J_e = J_0 \left( \exp^{eV_j/nkT} - 1 \right), \quad (3)$$

where  $J_0$  is the saturation current density;  $e$  is the elementary charge ( $1.6 \times 10^{-19}$  coul);  $n$  is the ideality factor;  $k$  is the Boltzmann constant ( $1.38 \times 10^{-23}$  J/K); and  $T$  is the absolute temperature [23]. It is well known that  $J_0$  and  $n$  are dependent on the material quality and/or device structure. The parameters used for the geometric dimensions and for the Shockley equation are the same as those used in previous studies [8]; that is, the saturation current and  $n$  are set to be  $4.72 \times 10^{-22}$  A and 2.5, respectively. The p-pad is set to have a uniform input current and the n-pad is set as the ground. With the exception of the electrodes, the rest of the boundaries in the LED chip are all assumed to be insulated. The relationship between  $J_0$  and  $T$  developed by Millman and Grabel [24] is also adopted in the present study:

$$J_0(T) = J_0|_{300\text{K}} \times 2^{(T-300)/10}. \quad (4)$$

The equation for conduction heat transfer with the heat source for the steady-state is

$$-k_c \nabla \cdot (\nabla T) = \dot{q}, \quad (5)$$

where  $k_c$  is the thermal conductivity [23]. Based on the law of energy conservation, the input electrical power can be divided into two major parts; one is the light output power and the other is heat generation. Given the same assumptions for the active layer as in (2), we propose the following heat generation term  $\dot{q}$  in the active layer [22]:

$$\dot{q} = J_e \times \frac{\left[ V_j - (\hbar\omega/e) \times \eta_{\text{int}} \times \eta_{\text{ext}} \times \exp(-(T-300)/1600) \right]}{l_e}, \quad (6)$$

where  $\hbar$  is the reduced Planck constant;  $\omega$  is the angular frequency;  $\eta_{\text{int}}$  is the internal quantum efficiency at room

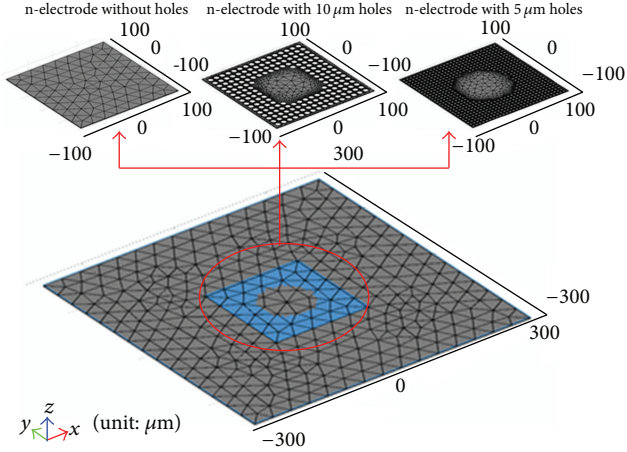


FIGURE 2: Triangular prism elements of each layer in the LED chip.

TABLE 1: Thermal conductivities used in the simulation [22, 23].

Material	Ni	Ag	Au	Ti	GaN
$k_c$ (W/m · K)	55.2	374	290	17.1	130

temperature; and  $\eta_{\text{ext}}$  is the light extraction efficiency at room temperature. The heat generated by light absorption inside the LED chip is assumed to be included in this  $\dot{q}$  term. In the present study, the value of the external quantum efficiency ( $\eta_{\text{int}} \times \eta_{\text{ext}}$ ) is 25%, as obtained in the literature [22]. The heat generation term per unit volume  $\dot{q}$  due to Joule heating [23] in the other layers of the LED chip is

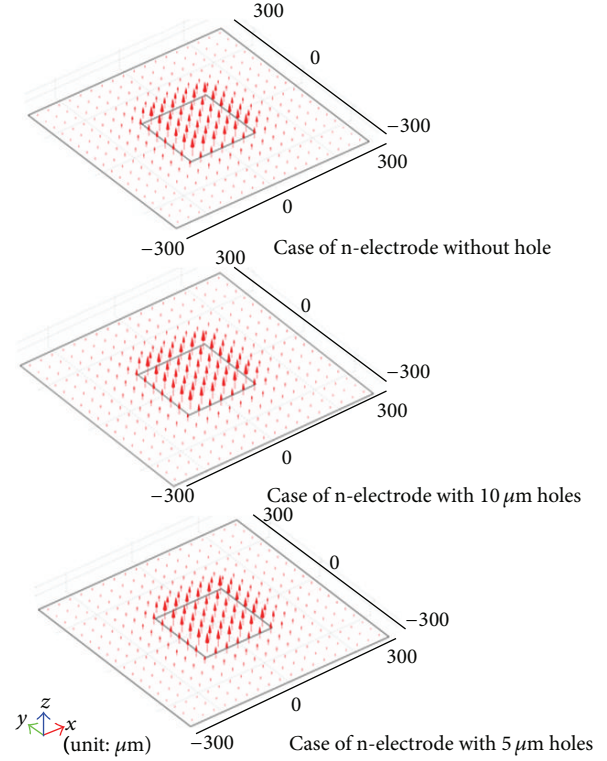
$$\dot{q} = J_e \cdot \nabla V. \quad (7)$$

The thermal conductivities of the materials are summarized in Table 1 [22, 23]. The thermal boundary conditions of the top, lateral, and bottom surfaces of the LED chip are shown by

$$\hat{n} \cdot (k_c \nabla T) = h_e (T_{\text{inf}} - T), \quad (8)$$

where  $\hat{n}$  is the unit normal vector of the interface;  $T_{\text{inf}}$  is the air temperature; and  $h_e$  is the equivalent heat transfer coefficient [23]. A copper slug with a board is usually used to dissipate the heat generated from the LED chip. The size is set to be about  $7.2 \text{ cm}^2$  in the present study. Natural convection conditions affect the surfaces with  $h_e = 5 \text{ W/m}^2 \cdot \text{K}$  and  $T_{\text{inf}}$  is 300 K. The convection from the bottom surface of the slug is replaced by the convection condition from the chip with the equivalent heat transfer coefficient  $h_e$ . In this case,  $h_e$  is about  $40000 \text{ W/m}^2 \cdot \text{K}$ .

A self-developed correlation coupling of the thermal and electrical equations is added to the FEM software (COMSOL Multiphysics licensed version 3.4) to obtain the temperature, the electrical potential, and the current density in the LED chip. In the present study, the simulation is performed in a three-dimensional, steady-state condition and the mesh for each layer is made up of triangular prism elements. The mesh numbers for n-electrodes with holes are much higher than for those without holes due to the structure of the holes. After

FIGURE 3: Current densities in the active layer with an input current of 100 mA for the case of  $L = 200 \mu\text{m}$ .

convergence testing, the mesh numbers are found to be 2656, 10681, and 18406 for the cases without holes, with  $5 \mu\text{m}$  holes and with  $10 \mu\text{m}$  holes, respectively, as shown in Figure 2. A circular area  $100 \mu\text{m}$  in diameter is reserved in the central region of the n-electrode for wire bonding. Utilizing a similar testing procedure, the relative tolerance is selected to be  $1 \times 10^{-3}$  for the variables of temperature and voltage.

### 3. Results and Discussion

Figure 3 displays the current densities in the active layer for an input current of 100 mA for the cases where  $L = 200 \mu\text{m}$ , without holes, with  $5 \mu\text{m}$  holes, and with  $10 \mu\text{m}$  holes. The simulated current density distributions show almost the same results. In every case, the current crowding beneath the n-electrode is more serious.

Figure 4 shows the temperature distribution in the active layer for the cases of  $L = 200 \mu\text{m}$ , without holes, with  $5 \mu\text{m}$  holes, and with  $10 \mu\text{m}$  holes, under the same operating conditions. There is little difference (about 0.1 K) in the maximum temperature in the active layer between the three cases. The temperature distribution results are also the same. Therefore, the structure of the holes on the n-electrode may not cause the change in thermal behavior in the active layer of the LED. The electrical characteristics of the LEDs will not be affected by this slight temperature difference. According to the analyses of the current distribution and temperature distribution, the influences of the n-electrode for cases with and without holes seem very tiny.

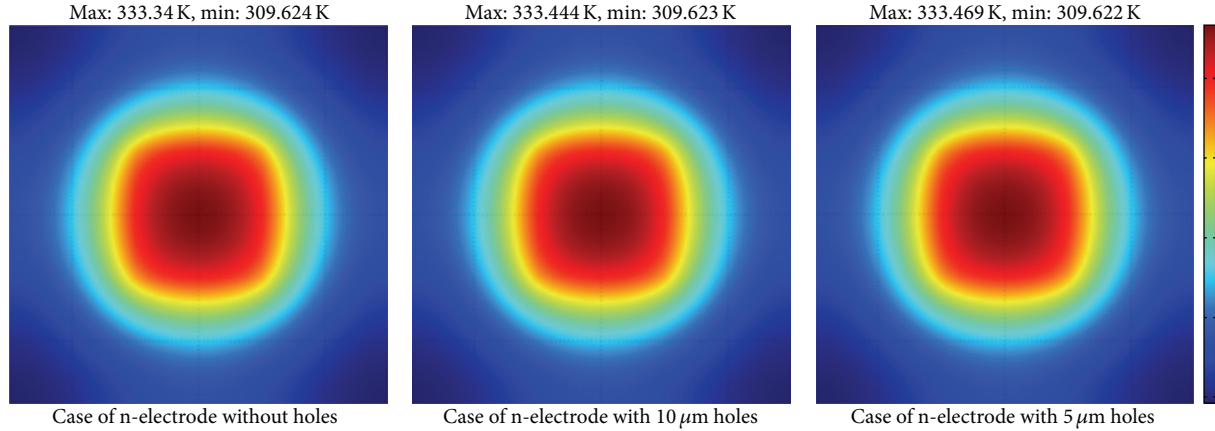


FIGURE 4: Temperature distributions in the active layer for the cases with  $L = 200 \mu\text{m}$ .

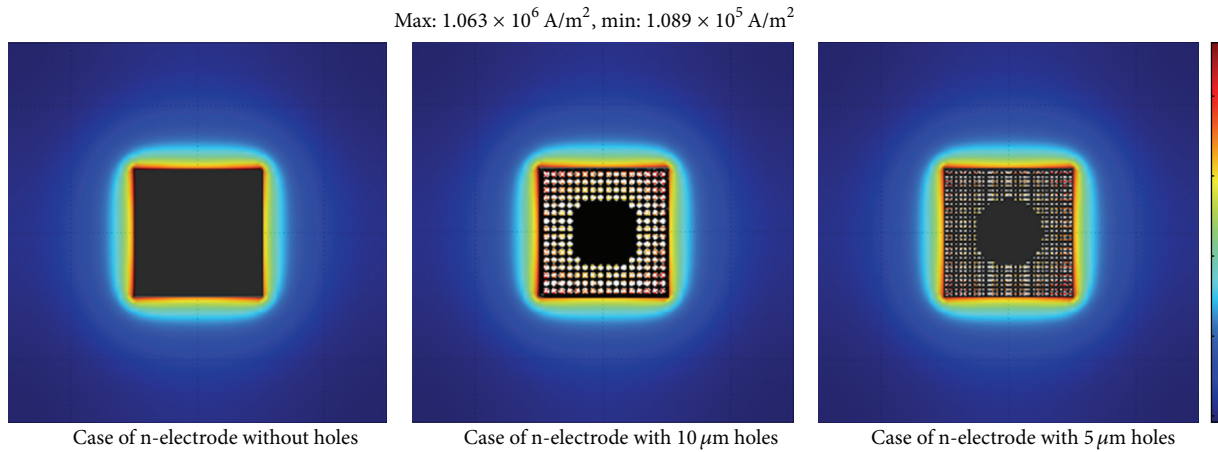


FIGURE 5: Current density distributions in the active layer including the shadow of the n-electrode.

In order to improve the shadowing effect of the n-electrode, the current density distributions in the active layer, including the shadow of the n-electrode are shown in Figure 5 for different cases. For the case with  $L = 200 \mu\text{m}$ , the area beneath the n-electrode is only 1/9 of the total area in the active layer, but the average current density beneath the n-electrode is 3.78 times that of the rest of the area (see Figure 3). The percentages of the light output power from those holes can be integrated in the present numerical simulation. A comparison between the two cases for n-electrodes with holes of different n-electrode size is shown in Figure 6. The results indicate that the n-electrode with  $10 \mu\text{m}$  holes offers increased light output power, about 2.45 times more than n-electrodes without holes.

The wall-plug efficiency of the LED chip is defined as the output light power divided by the total input electrical power. Here, the output light power is selected as the electrical power generated by the residual region of the active layer not covered by the n-electrode subtracted from the total heat generated in the same region. The WPEs for different sizes of n-electrodes with  $5 \mu\text{m}$  and  $10 \mu\text{m}$  holes are also discussed, and the results are compared with the cases of n-electrodes

without holes, as shown in Figure 7. The welding region occupies most of the area of n-electrodes with  $5 \mu\text{m}$  and  $10 \mu\text{m}$  holes in cases where  $L = 100 \mu\text{m}$ . The n-electrode thus obstructs most light emission for all the cases with and without holes. The WPE for the case without holes is very close to that of the cases with holes. The WPE then decreases as the size of the n-electrode is increased for the cases without holes since the major part of the light emitting area in the active layer is covered by the n-electrode. However, in the cases with holes, the WPE increases when  $L = 200 \mu\text{m}$  and then decreases as the size of the n-electrode increases. The light output from these holes plus that from the residual region of the active layer not covered by the n-electrode equals the total light output. Due to a higher current density under the n-electrode, the WPE for  $L = 200 \mu\text{m}$  reaches a maximum value. Otherwise, the size of the hole will also influence the light output. A larger size will emit more light output. Therefore, a better size for the n-electrode would be  $L = 200 \mu\text{m}$ , in the case with  $10 \mu\text{m}$  holes. The WPE can be increased from 2.33% to 5.72% by the design of n-electrode with holes. Based on the study of nanowire array LEDs [14], these LEDs give an external quantum efficiency of 2.5%. The results of the present

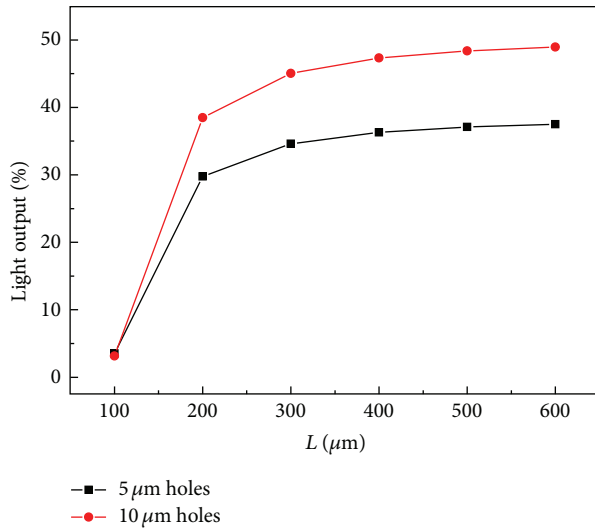


FIGURE 6: Percentage of light output with different sizes of n-electrode for the cases with two different hole sizes.

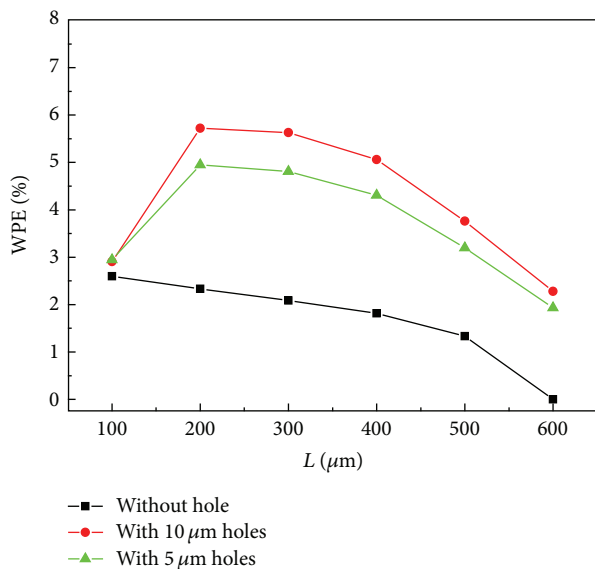


FIGURE 7: Calculated WPE for different sizes of n-electrode for the cases with and without holes.

study are found to agree with the experimental result obtained in the study of Xu et al. [14].

#### 4. Conclusions

In the present study, a design is proposed for n-electrode with holes for application in Thin-GaN LEDs. A new numerical model is used to investigate the effect of the n-electrode with holes design on the thermal and electrical characteristics of a Thin-GaN LED chip. The variation in current density and temperature distributions in the active layer is very tiny for n-electrodes with and without holes. The percentage of light output power from these holes ranges from 3.5% to 37.5% and from 3.1% to 49% for the cases with 5 μm and 10 μm holes

in n-electrodes with different side lengths ( $L$ ). Therefore, the light output power can be increased 2.45 times by using the n-electrode with holes design. When  $L = 100 \mu\text{m}$ , the wall-plug efficiency for the case without holes is very close to that of the cases with holes. For the cases with holes, the wall-plug efficiency increases when  $L = 200 \mu\text{m}$  and then decreases as the size of the n-electrode is increased. The devices with larger hole size will emit more light output. Thus, the wall-plug efficiency is also improved from 2.3% to 5.7% for the case of  $L = 200 \mu\text{m}$  n-electrodes with  $10 \mu\text{m}$  holes. WPE analysis is used to determine better n-electrode and hole sizes.

#### Acknowledgment

The authors gratefully acknowledge the support of the National Science Council of Taiwan for this work, through Grant no. NSC 101-2221-E-253-006.

#### References

- [1] S. H. Tu, J. C. Chen, F. S. Hwu et al., "Characteristics of current distribution by designed electrode patterns for high power ThinGaN LED," *Solid-State Electronics*, vol. 54, no. 11, pp. 1438–1443, 2010.
- [2] L. C. Chen, C. H. Tien, X. Liu, and B. Xu, "Zigzag and helical AlN layer prepared by glancing angle deposition and its application as a buffer layer in a GaN-based light-emitting diode," *Journal of Nanomaterials*, vol. 2012, Article ID 409123, 6 pages, 2012.
- [3] Y.-C. Hsu, Y.-K. Lin, M.-H. Chen et al., "Failure mechanisms associated with lens shape of high-power LED modules in aging test," *IEEE Transactions on Electron Devices*, vol. 55, no. 2, pp. 689–694, 2008.
- [4] A. Chakraborty, L. Shen, H. Masui, S. P. Denbaars, and U. K. Mishra, "Interdigitated multipixel arrays for the fabrication of high-power light-emitting diodes with very low series resistances," *Applied Physics Letters*, vol. 88, no. 18, Article ID 181120, 3 pages, 2006.
- [5] J.-P. Ao, "Monolithic integration of GaN-based LEDs," *Journal of Physics: Conference Series*, vol. 276, no. 1, Article ID 012001, 4 pages, 2011.
- [6] F. S. Hwu and H. L. Hsieh, "Numerical study of thermal behavior in alternating current light-emitting diodes," *Advances in Mechanical Engineering*, vol. 2013, Article ID 426767, 5 pages, 2013.
- [7] P. Wang, W. Wei, B. Cao, Z. Gan, and S. Liu, "Simulation of current spreading for GaN-based light-emitting diodes," *Optics & Laser Technology*, vol. 42, no. 5, pp. 737–740, 2010.
- [8] H. Kim, K.-K. Kim, K.-K. Choi et al., "Design of high-efficiency GaN-based light emitting diodes with vertical injection geometry," *Applied Physics Letters*, vol. 91, no. 2, Article ID 023510, 3 pages, 2007.
- [9] G.-J. Sheu, F.-S. Hwu, J.-C. Chen, J.-K. Sheu, and W.-C. Lai, "Effect of the electrode pattern on current spreading and driving voltage in a GaNSapphire LED chip," *Journal of the Electrochemical Society*, vol. 155, no. 10, pp. H836–H840, 2008.
- [10] J.-T. Chu, C.-C. Kao, H.-W. Huang et al., "Effects of different n-electrode patterns on optical characteristics of large-area p-side-down InGaN light-emitting diodes fabricated by laser lift-off," *Japanese Journal of Applied Physics*, vol. 44, no. 11, pp. 7910–7912, 2005.

- [11] S.-J. Wang, K.-M. Uang, S.-L. Chen et al., "Use of patterned laser liftoff process and electroplating nickel layer for the fabrication of vertical-structured GaN-based light-emitting diodes," *Applied Physics Letters*, vol. 87, no. 1, Article ID 011111, 3 pages, 2005.
- [12] D. W. Kim, H. Y. Lee, G. Y. Yeom, and Y. J. Sung, "A study of transparent contact to vertical GaN-based light-emitting diodes," *Journal of Applied Physics*, vol. 98, no. 5, Article ID 053102, 4 pages, 2005.
- [13] H. Kim, J. Cho, J. W. Lee et al., "Consideration of the actual current-spreading length of GaN-based light-emitting diodes for high-efficiency design," *IEEE Journal of Quantum Electronics*, vol. 43, no. 8, pp. 625–632, 2007.
- [14] S. Xu, C. Xu, Y. Liu et al., "Ordered nanowire array blue/near-UV light emitting diodes," *Advanced Materials*, vol. 22, no. 42, pp. 4749–4753, 2010.
- [15] O. Lupan, T. Pauporté, and B. Viana, "Low-voltage UV-electroluminescence from ZnO-Nanowire array/p-CaN light-emitting diodes," *Advanced Materials*, vol. 22, no. 30, pp. 3298–3302, 2010.
- [16] S. D. Hersee, M. Fairchild, A. K. Rishinaramangalam et al., "GaN nanowire light emitting diodes based on templated and scalable nanowire growth process," *Electronics Letters*, vol. 45, no. 1, pp. 75–76, 2009.
- [17] J.-C. Chen, G.-J. Sheu, F.-S. Hwu et al., "Electrical-optical analysis of a GaN/sapphire LED chip by considering the resistivity of the current-spreading layer," *Optical Review*, vol. 16, no. 2, pp. 213–215, 2009.
- [18] M. V. Bogdanov, K. A. Bulashevich, I. Y. Evstratov, A. I. Zhmaikin, and S. Y. Karpov, "Coupled modeling of current spreading, thermal effects and light extraction in III-nitride light-emitting diodes," *Semiconductor Science and Technology*, vol. 23, no. 12, Article ID 125023, 10 pages, 2008.
- [19] M. V. Bogdanov, K. A. Bulashevich, I. Y. Evstratov, and S. Y. Karpov, "Current spreading, heat transfer, and light extraction in multi-pixel LED array," *Physica Status Solidi (C)*, vol. 5, no. 6, pp. 2070–2072, 2008.
- [20] S. Hwang and J. Shim, "A method for current spreading analysis and electrode pattern design in light-emitting diodes," *IEEE Transactions on Electron Devices*, vol. 55, no. 5, pp. 1123–1128, 2008.
- [21] H. Kim, S.-J. Park, H. Hwang, and N.-M. Park, "Lateral current transport path, a model for GaN-based light-emitting diodes: applications to practical device designs," *Applied Physics Letters*, vol. 81, no. 7, pp. 1326–1328, 2002.
- [22] F.-S. Hwu, J.-C. Chen, S.-H. Tu, G.-J. Sheu, H.-I. Chen, and J.-K. Sheu, "A numerical study of thermal and electrical effects in a vertical LED chip," *Journal of the Electrochemical Society*, vol. 157, no. 1, pp. H31–H37, 2010.
- [23] F. S. Hwu, T. S. Sung, C. H. Chen et al., "A numerical model for studying multimicrochip and single-chip LEDs with an interdigitated mesa geometry," *IEEE Photonics Journal*, vol. 5, no. 2, Article ID 6600515, 2013.
- [24] J. Millman and A. Grabel, *Microelectronics*, McGraw-Hill, New York, NY, USA, 2nd edition, 1987.

## Research Article

# InGaAs Quantum Dots on Cross-Hatch Patterns as a Host for Diluted Magnetic Semiconductor Medium

**Teeravat Limwongse, Supachok Thainoi,  
Somsak Panyakeow, and Songphol Kanjanachuchai**

*Semiconductor Device Research Laboratory (Nanotec Center of Excellence), Department of Electrical Engineering,  
Faculty of Engineering, Chulalongkorn University, Bangkok 10330, Thailand*

Correspondence should be addressed to Songphol Kanjanachuchai; [songphol.k@chula.ac.th](mailto:songphol.k@chula.ac.th)

Received 19 March 2013; Accepted 13 June 2013

Academic Editor: Sudhakar Nori

Copyright © 2013 Teeravat Limwongse et al. This is an open access article distributed under the Creative Commons Attribution License, which permits unrestricted use, distribution, and reproduction in any medium, provided the original work is properly cited.

Storage density on magnetic medium is increasing at an exponential rate. The magnetic region that stores one bit of information is correspondingly decreasing in size and will ultimately reach quantum dimensions. Magnetic quantum dots (QDs) can be grown using semiconductor as a host and magnetic constituents added to give them magnetic properties. Our results show how molecular beam epitaxy and, particularly, lattice-mismatched heteroepitaxy can be used to form laterally aligned, high-density semiconducting host in a single growth run without any use of lithography or etching. Representative results of how semiconductor QD hosts arrange themselves on various stripes and cross-hatch patterns are reported.

## 1. Introduction

Quantum dots (QDs) are very small regions of homogeneous material with typical size smaller than 100 nm for semiconductors [1]. There are two main approaches to synthesize QDs: top down and bottom up [2]. The top-down approach starts with a bulk material and scales it down to small feature using lithography and etching. The bottom-up approach starts with atoms or molecules and scales them up by chemical means to the required size. The quantum dots of interests are diluted magnetic semiconductor (DMS) which, as its name suggests, is electrically semiconducting and magnetically active [3]. While their applications in memory technology have not yet been fully realized, it is expected that various forms of DMS structures can be used as magnetic storage dots or read heads in hard disk drives (HDDs). (For examples, see US Patents no. 7249518 sensors based on giant planar hall effect in dilute magnetic semiconductors, no. 5294287 class of magnetic materials for solid state devices, 6999279 perpendicular patterned magnetic media, no. 6947235 Patterned multilevel perpendicular magnetic recording media, and no. 6906879 magnetic recording system with patterned multilevel perpendicular magnetic recording.) The paper is

organized as follows. Section 2 reviews the current magnetic media technologies. Section 3 explains how DMS will benefit hard disk-based storage. Section 4 describes how QD semiconducting hosts for DMS are formed using molecular beam epitaxy (MBE), followed by the summary in Section 5.

## 2. Magnetic Media

A key characteristic of HDDs is storage capacity in gigabyte which is directly proportional to the areal density of the magnetic medium. The areal density in bits per square inch is a product of bits per inch along a recording track times the number of tracks per inch. Smaller magnetic bits will allow the increases in bits/inch and tracks/inch, resulting in increased areal density and storage capacity. One key goal in HDD research is to increase the areal density which has been increasing approximately at an exponential rate. The rapid increase is enabled by improvements in several technologies, mainly read-write heads and magnetic media.

Magnetic media generally contains Co, due to its high magnetocrystalline anisotropy and coercivity, and is alloyed with Cr and Pt. The magnetic media are in the form of thin film, typically less than 50 nm [4], deposited on a glass,

ceramic, or metal substrate by a vacuum deposition process or by sputtering. Information is stored in small magnetic grains (CoCrPt) segregated in an insulator (SiO<sub>2</sub>). The grain size in current disk generation is kept between 10 and 50 nm and is a competition between fundamental limits and economic considerations: end users want high-capacity disks which drive *down* the grain size, but smaller grains are unstable as thermal energy can randomly revert magnetization direction and hence can corrupt the stored information. This superparamagnetic limit thus drives *up* the grain size and keeps it above 10 nm. Because of the randomness of the grain shapes and sizes, each bit written on the disk must cover about 100 grains to ensure reliable storage [5]. Our proposed approach provides a nonrandom semiconducting host (InAs QDs on cross-hatch pattern) that when diluted with a 3d transition element such as Mn can provide a magnetic medium that theoretically takes a single grain to store one bit. The semiconducting host is a prerequisite for diluted magnetic semiconducting media.

### 3. Diluted Magnetic Semiconductors

Diluted magnetic semiconductors are a class of material that exhibits both semiconducting and ferromagnetic properties and can thus provide a platform for data storage and processing in the same material. A DMS is traditionally defined as a diamagnetic semiconductor doped with a few to several atomic per cent of some transition metal with unpaired d electrons [6]. DMS materials can be realized by alloying a transition metal with III–V binary (GaMnAs, InMnAs, InMnSb, InFeAs, GaCrSb), ternary (GaInMnAs, GaAlMnSb, InMnAsSb, GaCrAsSb), and quaternary (GaInMnAsP, GaAlInMnSb) compounds [7].

One of the most studied DMS systems is Ga<sub>1-x</sub>Mn<sub>x</sub>As with  $0 < x < 8\%$  grown using MBE. Despite significant effort, the maximum Curie temperature of bulk (Ga, Mn)As is still well below room temperature,  $T_c < 190$  K, yet theories predict that at  $x > 10\%$  (Ga, Mn)As can exhibit room temperature ferromagnetism [8]. However, incorporation of Mn at such high concentration suffers from solid solubility limits and high vapor growth in MBE: Mn tends to agglomerate on the surface giving rise to elemental Mn clusters, as opposed to the desired random incorporation that results in carrier-mediated spin coupling. Migration-enhanced epitaxy may help but requires precise temperature control [8].

MBE is typically used to grow III–V compounds such as GaAs (the host for GaMnAs), InAs (host for InMnAs), and InGaAs (host for GaInMnAs); all are potential hosts for room-temperature DMS materials. Recently, it has been shown that GaMnAs nanodot arrays are a DMS with  $T_c = 140$  K [9]. The synthesis of such GaMnAs quantum dot arrays, however, requires top-down masking technique which creates structural defects and is thus inferior to self-assembled techniques that can grow defects-free QDs, particularly if the technique can grow self-assembled and self-aligned QDs.

## 4. Quantum Dots on Cross-Hatch Patterns

We demonstrated the use of lattice-mismatched InGaAs films grown on GaAs as templates for the growth of self-assembled and self-aligned QDs. By growing InAs QDs on a nonplanar surface, the nucleation positions of the QDs can be controlled. The use of InGaAs/GaAs stripes and cross-hatch patterns (CHPs) as templates for subsequent nucleation of QDs gives rise to laterally aligned QDs. The areal density of the QDs is dictated by the dislocation line densities. This section describes the results and explains the mechanisms related to the growths of QDs, CHPs, and QDs on CHPs, respectively.

*4.1. Quantum Dots.* When a material with atomic spacing  $a_1$  is grown on a substrate with a different atomic spacing  $a_0$ , the growth mode will be principally determined by the degree of misfit  $\varepsilon \equiv (a_1 - a_0)/a_0$ . For thin films with low misfits, the epilayer will grow layer by layer in the Frank-van der Merwe (FM) mode, resulting in smooth films. The growing layer, however, has a different atomic spacing ( $a_0$ ) from thermal equilibrium ( $a_1$ ) and is thus under strain. The associated strain energy is contained in this growing layer. As growth continues and the thickness increases, the strain energy will also increase. When the strain energy is too high, the two-dimensional (2D) film is unstable and spontaneous formation of three-dimensional (3D) dots will occur, resulting in the reduction of the total energy of the system. The resulting dots are usually small and exhibit quantum behaviors, hence *quantum dots*. The growth of semiconductor QDs by this mechanism is a well-known phenomenon called Stranski-Krastanow (SK) growth mode [10] and has been observed in the growth of several semiconductor QD systems such as InAs on GaAs [11] or Ge on Si [12]. These QDs are defects-free and are electronically and optically active. Quantum effects which include delta function-like density of states and size-dependent electronic levels allow several physical properties to be tuned. Electronic devices that benefit from QDs as the active medium, or as part of the active layer, include single-electron transistors [13], flash memory [14], and lasers [15]. With transition element incorporation, the magnetic properties of these QDs can also be tuned.

The spontaneous formation of QDs via the SK growth mode is a statistical process; the positions of QDs are random, and an example is shown in the atomic force microscopic (AFM) image of InAs QDs on low-mismatched InGaAs in Figure 1. Though the size of the QDs is quite uniform, the positions are completely random. For QD hosts to be appropriate as a HDD medium, the QDs must not only have high density but they must also line up in accordance with data read-write scheme. For rotating media with information access by head gimbal assemblies (HGA), the QDs should line up radially. For stationary media with information access by multichannel read-write probe matrix, the QDs should line up orthogonally.

*4.2. Cross-Hatch Patterns.* Cross-hatch patterns are used as templates to influence the QDs to nucleate orthogonally.

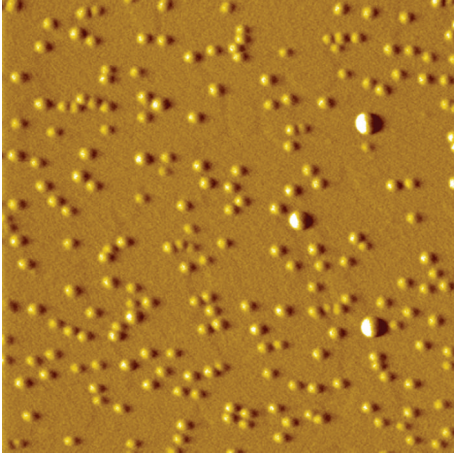


FIGURE 1: AFM image ( $2 \times 2 \mu\text{m}^2$ ) of InAs QDs grown on planar InGaAs surface.

CHPs are formed by lattice-mismatched heteroepitaxy similar to the QDs above; the only difference is the degree of mismatch  $\varepsilon$ . To form a CHP instead of a QD, the misfit needs to be low. For a certain epilayer thickness there is a range of  $\varepsilon$  that will result in a cross-hatch pattern.

Figure 2 illustrates the case of lattice-mismatched epitaxy of 50 nm  $\text{In}_x\text{Ga}_{1-x}\text{As}$  on flat (001)-GaAs substrates. Figure 2(a) shows the primordial stage or the onset of CHP formation at low In molar fraction of  $x \approx 8\%$  or misfit of  $\varepsilon \approx 0.573\%$ . The surface is atomically flat: the height contrast in the figure is only 0.79 nm, less than twice the lattice parameters. The AFM image clearly shows atomic steps with dominant surface ripples running along the [110] crystallographic direction. Some ripples running orthogonally, along the [1-10] direction, can be seen to be merging. The ripples along the [1-10] direction merge and form long lines before those along the [110] direction do due to asymmetric adatoms mobilities in the two orthogonal directions which explains the generally observed asymmetric misfit dislocation (MD) line densities.

Figure 2(b) shows the complete CHP formation at In molar fraction of  $x = 15\%$  or misfit of  $\varepsilon = 1.075\%$ . The surface morphology exhibits asymmetrical cross-hatch pattern with MD line density along [1-10] direction greater than [110] direction due to the different formation times as explained above. The heights of most hatches range between 0.5 and 2 nm with those along the [1-10] direction slightly taller.

There are two challenges in employing CHPs as templates for the growth of regularly arranged, high-density QDs. First, the [110] and [1-10] line densities need be symmetrical. In view of different adatom mobilities as a result of solid source-derived  $\text{As}_4$ , this asymmetry is fundamental and cannot be avoided. With the availability of a cracker valve or a higher cracking temperature source that yields the more reactive  $\text{As}_2$  species, the degree of asymmetry is expected to decrease. Second, there is an upper limit to which  $\varepsilon$  (or equivalently  $x$ ) can be increased before the growth mode changes from 2D (FM) to 3D (SK). This also sets the upper limit to subsequent QD areal density.

**4.3. Quantum Dots on Cross-Hatch Patterns.** Growth of InAs QDs on InGaAs CHPs leads to spontaneous alignment of QDs along the cross-hatches. Main parameters used to control/optimize QDs alignment are growth interruption which affects the orderliness of QDs on the hatches [16], cross-hatch layer thickness, and composition which affect MD line density [17], growth rates, excess growth, and the use of spacer layer prior to QD growth [18]. The origin and evolution of InAs QD alignment on InGaAs CHPs, which apply to other material systems, are now well understood [19, 20]. This section captures the main results of our continued efforts towards aligning InAs QDs on InGaAs CHPs.

Figure 3 shows the AFM images of InAs QDs on 50 nm  $\text{In}_x\text{Ga}_{1-x}\text{As}$  layer grown on (001)-GaAs when the In molar fraction ( $x$ ) increases from 8% in Figure 3(a) to 10% in Figure 3(b) and to 15% in Figures 3(c) and 3(d). The QDs on the surfaces of these samples can be grouped into two broad categories: those nucleated along the buried dislocation lines and those nucleated on the flat regions between the dislocations. For  $x = 8\%$ , Figure 3(a) shows that the majority QDs are dispersed randomly on the flat regions while the minority formed along the MD lines. The QDs along the MD lines are taller and more closely spaced. For  $x = 10\%$ , Figure 3(b) shows that the MD line density is greater than that observed in Figure 3(a) and that the proportion of QDs on the MD lines increases as a result. The increased MD line density results from the increased misfit. The greater the misfit the shorter the average dislocation spacing  $l$ . In the case of  $x = 8\%$  in Figure 3(a), only [1-10] MD lines are observed and the average dislocation spacing  $l_{[1-10]} \approx 5 \mu\text{m}$ . In the case of  $x = 10\%$  in Figure 3(b),  $l_{[1-10]} \approx 1.5 \mu\text{m}$  while  $l_{[110]} > 10 \mu\text{m}$ . In the high-misfit case of  $x = 15\%$ , the dislocation distribution is highly irregular. Some parts of the wafer show moderate MD density as seen in Figure 3(c) while other parts show high or very high density as seen in Figure 3(d). The stochastic nature of dislocation formation gives rise to this asymmetrical behavior, and we believe this particular characteristic is also present in Figures 3(a) and 3(b), although it is possible to tune the growth parameters to obtain dislocation spacing in one direction to be greater than the sample size in which case the surface pattern would not be a cross-hatch one but rather stripes. When the cross-hatch spacing is smaller than adatoms diffusion lengths on the surface, all adatoms will be driven towards the dislocation lines leaving the regions in between completely free of QDs. The denuded zones can be observed in Figures 3(c) and 3(d).

## 5. Conclusion

InAs QDs on InGaAs/GaAs are grown by MBE. Lattice-mismatched epitaxy results in the formation of QDs, CHPs, stripes, and smooth films in decreasing order of misfit. For low-misfit InGaAs/GaAs, the dislocation lines making up the CHPs are widely spaced, resulting in stripes or cross-hatch patterns. For intermediate-misfit InGaAs/GaAs, surface CHPs are characterized by narrowly spaced dislocation lines along the two orthogonal directions with a different line density. Subsequent growth of high-misfit InAs or InGaAs

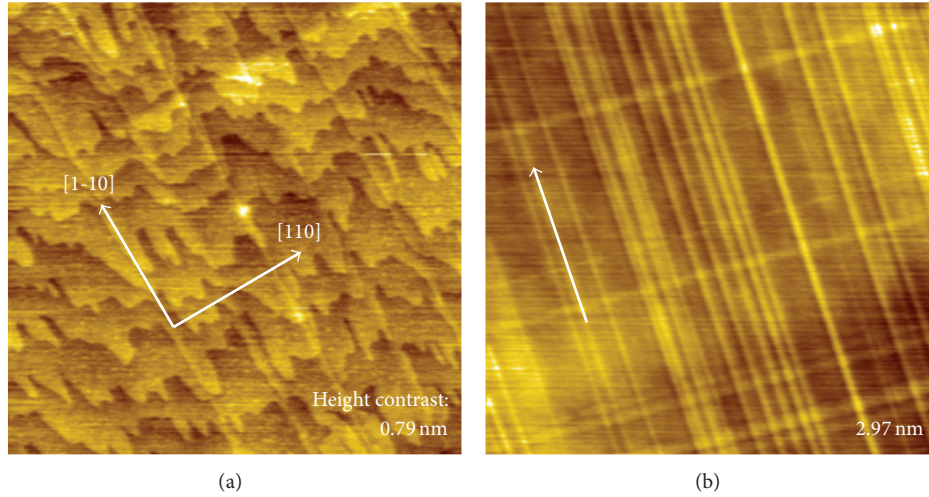


FIGURE 2: AFM images of 50 nm  $\text{In}_x\text{Ga}_{1-x}\text{As}$  films on (001)-GaAs during (a) early or (b) late stages of CHP formation. (a) Image size:  $5 \times 5 \mu\text{m}^2$ , height contrast: 0.79 nm, effective  $x < 8\%$ . (b) Image size:  $10 \times 10 \mu\text{m}^2$ , height contrast: 2.97 nm,  $x = 15\%$ .

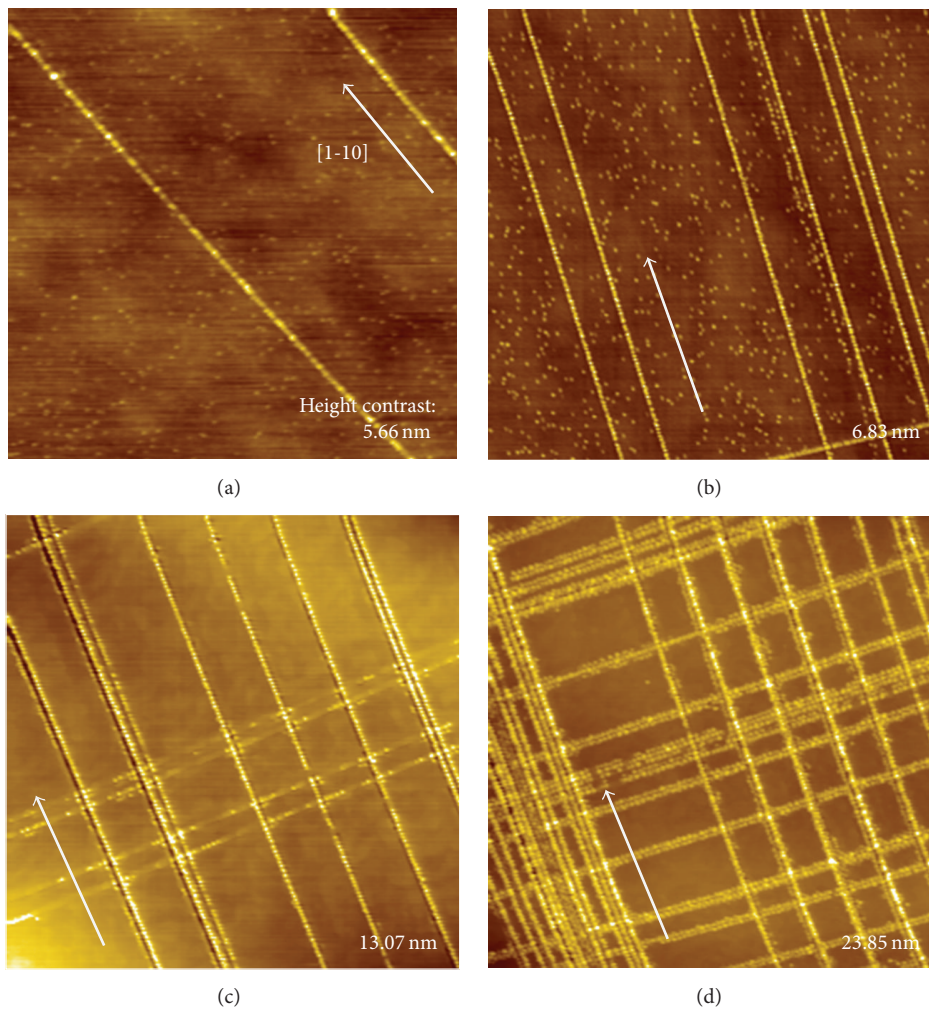


FIGURE 3: AFM images ( $10 \times 10 \mu\text{m}^2$ ) of InAs QDs on  $\text{In}_x\text{Ga}_{1-x}\text{As}/\text{GaAs}$  surfaces with increasing lattice mismatch, or In molar fraction from (a)  $x = 0.08$  to (b) 0.10 and (c) and (d) 0.15.

on stripes or CHP surfaces results in uni- or bidirectionally aligned QDs, respectively. The unidirectionally aligned QDs result in QD chains with electronic and optical coupling between dots. The bidirectionally aligned QDs result in QD matrices. With appropriate alloying of a transition element and careful control of average dislocation spacings, these QD matrices can exhibit spin coupling and may serve as a high-density DMS medium/read head.

## Acknowledgments

Pornchai Changmoang is acknowledged for maintaining the MBE system. This work is partially funded by I/UCRC in HDD Component, the Faculty of Engineering, Khon Kaen University (CPN R&D 01-18-53); NSTDA via Nectec and Nanotec; Thailand Research Fund (DPG5380002, RSA5580015); and the Higher Education Research Promotion and National Research University Project of Thailand, Office of the Higher Education Commission (EN1180A-56).

## References

- [1] P. Harrison, *Quantum Wells, Wires and Dots: Theoretical and Computational Physics of Semiconductor Nanostructures*, John Wiley & Sons, 2nd edition, 2005.
- [2] G. Cao, *Nanostructures and Nanomaterials: Synthesis, Properties & Applications*, Imperial College Press, 2004.
- [3] M. Jain, Ed., *Diluted Magnetic Semiconductors*, World Scientific, 1992.
- [4] S. O. Kasap, *Principle of Electronic Materials and Devices*, McGraw-Hill, 3rd edition, 2002.
- [5] Perpendicular Magnetic Recording Technology white Paper, Hitachi Global Storage Technology, 2011.
- [6] S. A. Chambers and B. Gallagher, "Focus on dilute magnetic semiconductors," *New Journal of Physics*, vol. 10, Article ID 055004, 2008.
- [7] L. L. Chang, L. Esaki, H. Munekata, H. Ohno, and S. von Molnar, "Class of magnetic materials for solid state devices," US patent #5296048.
- [8] T. Jungwirth, K. Y. Wang, J. Mašek et al., "Prospects for high temperature ferromagnetism in (Ga,Mn)As semiconductors," *Physical Review B*, vol. 72, no. 16, Article ID 165204, 2005.
- [9] S. P. Bennett, L. Menon, and D. Heiman, "Magnetic properties of GaMnAs nanodot arrays fabricated using porous alumina templates," *Journal of Applied Physics*, vol. 104, no. 2, Article ID 024309, 4 pages, 2008.
- [10] I. N. Stranski and L. Krastanow, "Zur Theorie der orientierten Ausscheidung von Ionenkristallen aufeinander," *Sitzungsberichte-Akademie Der Wissenschaften in Wien, Mathematisch-Naturwissenschaftliche Klasse Abteilung Iib*, vol. 146, pp. 797–810, 1938.
- [11] M. Grundmann, O. Stier, and D. Bimberg, "InAs/GaAs pyramidal quantum dots: strain distribution, optical phonons, and electronic structure," *Physical Review B*, vol. 52, no. 16, pp. 11969–11981, 1995.
- [12] F. K. Legoues, M. Copel, and R. M. Tromp, "Microstructure and strain relief of Ge films grown layer by layer on Si(001)," *Physical Review B*, vol. 42, no. 18, pp. 11690–11700, 1990.
- [13] L. Zhuang, L. Guo, and S. Y. Chou, "Silicon single-electron quantum-dot transistor switch operating at room temperature," *Applied Physics Letters*, vol. 72, no. 10, pp. 1205–1207, 1998.
- [14] J. J. Welser, S. Tiwari, S. Rishton, K. Y. Lee, and Y. Lee, "Room temperature operation of a quantum-dot flash memory," *IEEE Electron Device Letters*, vol. 18, no. 6, pp. 278–280, 1997.
- [15] R. Mirin, A. Gossard, and J. Bowers, "Room temperature lasing from InGaAs quantum dots," *Electronics Letters*, vol. 32, no. 18, pp. 1732–1734, 1996.
- [16] C. C. Thet, S. Panyakeow, and S. Kanjanachuchai, "Growth of InAs quantum-dot hatches on InGaAs/GaAs cross-hatch virtual substrates," *Microelectronic Engineering*, vol. 84, no. 5–8, pp. 1562–1565, 2007.
- [17] C. C. Thet, S. Sanorpim, S. Panyakeow, and S. Kanjanachuchai, "The effects of relaxed InGaAs virtual substrates on the formation of self-assembled InAs quantum dots," *Semiconductor Science and Technology*, vol. 23, no. 5, Article ID 055007, 5 pages, 2008.
- [18] S. Kanjanachuchai, M. Maitreeboriraks, C. C. Thet, T. Limwongse, and S. Panyakeow, "Self-assembled InAs quantum dots on cross-hatch InGaAs templates: excess growth, growth rate, capping and preferential alignment," *Microelectronic Engineering*, vol. 86, no. 4–6, pp. 844–849, 2009.
- [19] T. Limwongse, S. Panyakeow, and S. Kanjanachuchai, "Evolution of InAs quantum dots grown on cross-hatch substrates," *Physica Status Solidi (C) Current Topics in Solid State Physics*, vol. 6, no. 4, pp. 806–809, 2009.
- [20] S. Kanjanachuchai and T. Limwongse, "Nucleation sequence of InAs quantum dots on cross-hatch patterns," *Journal of Nanoscience and Nanotechnology*, vol. 11, no. 12, pp. 10787–10791, 2011.

## Research Article

# Nanocrystallization of Coarse Primary Phases in Al- and Mg-Based Alloys Induced by HCPEB Treatment

Gao Bo, He Jidong, Tu Ganfeng, and Hu Liang

School of Materials and Metallurgy, Northeastern University, Shenyang 110004, China

Correspondence should be addressed to Gao Bo; [surfgao@yahoo.com.cn](mailto:surfgao@yahoo.com.cn)

Received 12 April 2013; Accepted 26 May 2013

Academic Editor: Yogendra Mishra

Copyright © 2013 Gao Bo et al. This is an open access article distributed under the Creative Commons Attribution License, which permits unrestricted use, distribution, and reproduction in any medium, provided the original work is properly cited.

This paper reports on a phenomenon associated with high-current pulsed electron beam (HCPEB) treatment: surface nanocrystallization of coarse primary phase in hypereutectic Al17.5Si and quasicrystal alloys after multiple pulses of HCPEB irradiation. The HCPEB treatment induces superfast heating and diffusion of alloying elements and heterogeneous nucleation in a melting solution, followed by rapid solidification and cooling of the material surfaces. Consequently, nanostructured surface layers can be achieved easily. Nano-Si phase and nano-quasicrystal phase formation on the modified surface layer of hypereutectic Al17.5Si alloy and quasicrystal alloy ( $\text{Mg}_{37}\text{Zn}_{60}\text{Y}_3$ ) show a potential for surface nanocrystallization of materials with enhanced properties by HCPEB treatment.

## 1. Introduction

Nanomaterials are typically characterized by ultrafine grains ranging from 1 nm to 100 nm (at least one dimension) [1, 2]. Nanomaterials fundamentally exhibit unique properties such as increased strength/hardness, enhanced diffusivity, improved toughness/ductility, reduced elastic modulus, enhanced thermal expansion coefficient, and superior soft magnetic properties [3] compared with conventional coarse-grained materials.

The high-current pulsed electron beam (HCPEB) technique is a novel method [4–10] used to modify the surface of a material. This technique is simple, reliable, and has been proven highly efficient for decades. The electron beam causes intense and superfast melting as well as evaporation and solidification on the surface of target materials, thereby creating thermal stress and shockwaves. Consequently, nonequilibrium phase and structural transformations occur in the beam-affected zone, including a metastable structure or phase states on the surface layer [11, 12]. The combination of influencing factors unique to HCPEB treatment can induce the formation of nanocrystalline layers in the near-surface regions of metallic materials [10–12]. The present study

reports on the nanocrystallization of coarse primary phases in Al- and Mg-based alloys induced by HCPEB.

## 2. Experimental Procedures

**2.1. Starting Materials and HCPEB Treatment.** The starting materials consisted of  $\text{Mg}_{67}\text{Zn}_{30}\text{Y}_3$  quasicrystal alloy (with a chemical composition of Zn (50.86 wt%), Y (7.02 wt%), and Mg balance) and hypereutectic Al-17.5Si alloy (with a chemical composition of Si (17.5 wt%) and Al balance). Prior to HCPEB treatment, the samples were cut into  $\Phi 10 \text{ mm} \times 9 \text{ cm}$  cylinders with surfaces mechanically polished and washed with absolute ethyl alcohol. The sample surfaces were then treated on a Nadezhda-2-type HCPEB system under the following conditions: accelerating voltage, 23 kV; energy density,  $3 \text{ J/cm}^2$ ; pulse duration,  $\sim 1 \mu\text{s}$ ; and number of pulses, 2, 10, and 15 for the quasicrystal alloy  $\text{Mg}_{67}\text{Zn}_{30}\text{Y}_3$  and 5, 15, and 100 for the hypereutectic Al-17.5Si alloy.

**2.2. Microstructural Analysis.** The sample surface and cross-sectional morphologies were analyzed using a field-emission gun scanning electron microscope (FEG-SEM) (Jeol JSM

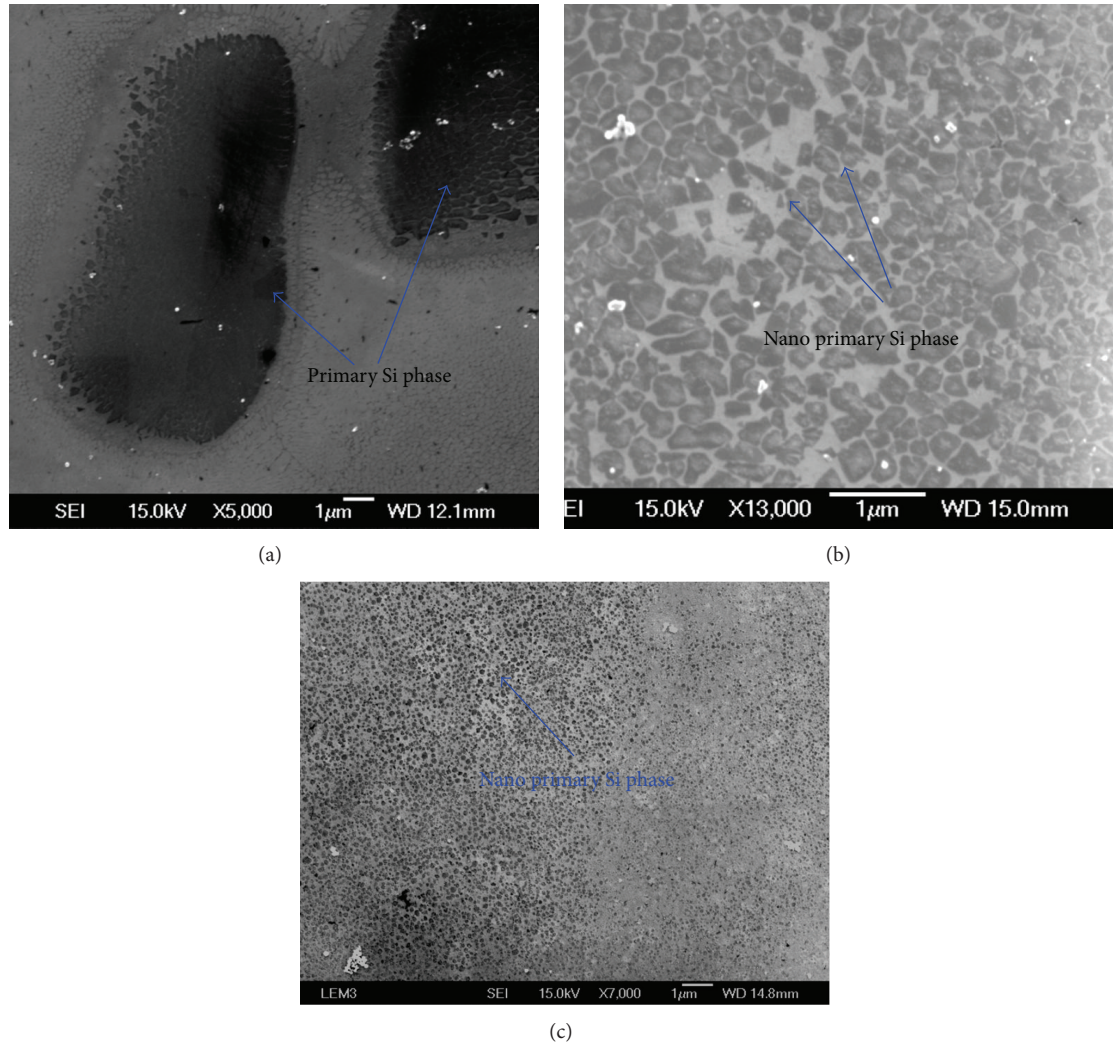


FIGURE 1: The evolution of the coarse primary Si phase in hypereutectic Al17.5Si alloy with number pulse of HCPEB treatment of hypereutectic Al-17.5Si alloy ((a) 5 pulse, (b) 15 pulse, and (c) 100 pulse).

6500 F) with an electron backscatter diffraction acquisition camera and Channel 5 software. The beam control mode was applied for automatic orientation mapping with a step size of  $0.04 \mu\text{m}$ . Thin films for transmission electron microscopy (TEM) were prepared by grinding, dimpling, and ion-beam thinning, and the microstructure characteristics were observed using a transmission electron microscope (FEI-Tecnai G220).

**2.3. Wear Resistance Measurement.** The dry wear tests for the two alloys were performed by an MG-2000 type pin-on-disc machine at room temperature of  $25^\circ\text{C}$ . The sample size was 6 mm-diameter and 12 mm-length. The stainless steel (1Cr18Ni9) was acted as sliding counterpart disc in wear tests, whose surface hardness and roughness were 192 HV and  $1 \mu\text{m}$  ( $R_a$ ), respectively. The applied load was 10 N. Sliding speed and distance were kept at 0.8 m/s and 0.096 km.

### 3. Results

#### 3.1. Nano-Si Phase in Irradiated Hypereutectic Al17.5Si Alloy.

Figure 1 shows the evolution of the coarse primary Si phase in hypereutectic Al17.5Si alloy with the number of pulses of HCPEB treatment. Figure 1(a) presents the typical SEM micrograph taken on a 5-pulsed sample. The figure shows that the size of the coarse primary Si phase is approximately  $20 \mu\text{m}$ , and the edge of the primary Si phase begins to melt and form fine Si crystals with a size of 500 nm. In the Al-rich zone outside the primary Si phase, the special nanocellular structure is formed. Figure 1(b) presents a typical SEM micrograph of the Si-rich zone taken on a 15-pulsed sample. As indicated in the figure, the coarse primary Si phase disappears completely, and numerous fine, dispersive nanoprimary Si phases are formed, with sizes ranging from 200 nm to 300 nm. Figure 1(c) shows a typical SEM micrograph of the Si-rich zone on a 100-pulsed sample. The figure reveals that the coarse primary Si phase is refined further, with sizes

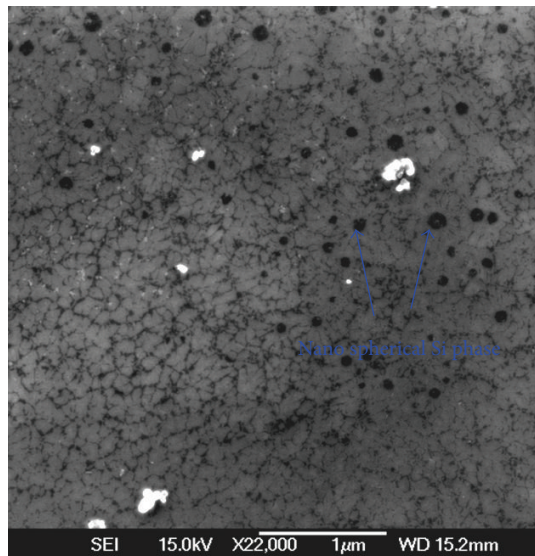


FIGURE 2: High magnification SEM image of primary Si phase in HCPEB-treated hypereutectic Al-17.5Si alloy under energy density of  $3 \text{ J/cm}^2$  and 100 pulses.

ranging from 60 nm to 120 nm. The morphology of the nano primary phase almost resembles a spherical shape. Figure 1 shows that the size of the primary Si phase is refined in the range of  $20 \mu\text{m}$  to  $30 \mu\text{m}$  in the initial sample, whereas the size of the 100-pulsed sample is refined in the range of 60 nm to 120 nm. We can deduce that with the increase in the number of pulses, the coarse primary Si phase underwent multiple melting, diffusion, and solidification and was then refined step by step to sizes ranging from 60 nm to 120 nm.

Figure 2 reveals a high-magnification FEG-SEM image of the 100 pulses treated with Al-17.5Si alloy. As indicated in the figure, a number of ultrafine and dispersive spherical Si crystals are formed in the Si-rich zone and surrounded by  $\alpha(\text{Al})$  cells. The  $\alpha(\text{Al})$  cells grow on top of the nano-Si crystals, indicating that nano-Si crystals can function as superfine heterogeneous nucleation sites for the  $\alpha(\text{Al})$  phase. A detailed discussion is provided in the subsequent section.

**3.2. Nano-Quasicrystal Phase in Irradiated  $\text{Mg}_{67}\text{-Zn}_{30}\text{-Y}_3$  Quasicrystal Alloy.** Figure 3 presents the SEM back-scattered electron images of the  $\text{Mg}_{67}\text{Zn}_{30}\text{Y}_3$  quasicrystal alloy in its initial state and after HCPEB treatment for 2 and 15 pulses. Figure 1(a) shows the initial structure of the  $\text{Mg}_{67}\text{Zn}_{30}\text{Y}_3$  quasicrystal alloy, composed of the following: a gray matrix phase, a black dendrite phase, and a white petal-shaped phase. Energy-dispersive X-ray spectroscopy (EDS) analysis demonstrates that the chemical composition of the gray matrix phase consists of Mg 68.820%, Zn 30.858%, and Y 0.322%. The globular black dendrite is composed of Mg 45.088%, Zn 54.080%, and Y 0.832%. In Figure 1(a), the most prominent characteristic of the initial structure is the formation of the white petal-shaped phase, consisting of Mg 37.496%, Zn 53.022%, and Y 9.482%. This phase is represented by the chemical formula  $\text{Mg}_{37}\text{Zn}_{53}\text{Y}_{10}$ , which deviates from

the quasicrystal  $\text{Mg}_{30}\text{Zn}_{60}\text{Y}_{10}$  of the standard ternary Mg-Zn-Y alloy reported in [13]. The white petal-shaped phase is a quasicrystal phase confirmed by TEM detection [14].

As shown in Figure 3(b), the surfaces of  $\text{Mg}_{67}\text{Zn}_{30}\text{Y}_3$  quasicrystal alloys are repeatedly melted and solidified owing to multiple HCPEB treatments (two pulses). Consequently, the phase boundaries between different phases become indistinct, and a petal-shaped white phase in the initial structure is uniformly distributed in the matrix after HCPEB irradiation. Figure 3(c) shows the top-surface microstructure characteristics of  $\text{Mg}_{67}\text{Zn}_{30}\text{Y}_3$  after a 15-pulsed treatment. Compared with that of the sample after a two-pulsed treatment, the chemical composition distribution becomes more uniform, with the phase boundary becoming indistinct. By EDS analysis, the dispersed white phase is determined to consist of Mg 58.139%, Zn 34.655%, and Y 7.206%. Under HCPEB treatment, the Mg element in the matrix phase and dendrite phase diffuses into a white phase, whereas Zn and Y elements enriched in the white phase diffuse outward. HCPEB irradiation leads to the interdiffusion of alloying elements; consequently, the chemical composition of the treated surface layer exhibits a homogeneous distribution. Simultaneously, the size of the petal quasicrystal phase becomes significantly refined after multiple irradiations. The size and morphology of the quasicrystal phase are analyzed by TEM.

Figures 4(a) and 4(b) present a TEM bright field image of 10-pulse treated  $\text{Mg}_{67}\text{Zn}_{30}\text{Y}_3$  and its corresponding selected area (electron) diffraction pattern (diffraction rings) [14]. After the 10-pulse treatment, numerous nanosized particles with grain sizes ranging from 10 nm to 30 nm are uniformly distributed on the surface layer. To determine the crystalline structure of the nanophase, the interplanar spacing values corresponding to each diffraction ring were calculated. Compared with the interplanar spacing ( $d_{\text{stan}}$ ) values of the acknowledged quasicrystal  $\text{Mg}_3\text{Zn}_6\text{Y}$ , the relative errors of all calculated results, except for one, are within 5%. Thus, the dispersed metastable nanocrystalline phase is a quasicrystal phase  $\text{Mg}_3\text{Zn}_6\text{Y}$ , indicating that a nanostructured quasicrystal layer is obtained by the action of electron beam.

**3.3. Improvement in Wear Resistance.** The weight loss of the Al-17.5Si and the  $\text{Mg}_{67}\text{Zn}_{30}\text{Y}_3$  quasicrystal alloys was determined before and after the HCPEB treatment. The results are shown in Figure 5. For the Al-17.5Si alloy, weight loss was reduced from  $1.3 \times 10^{-3} \text{ g}$  of the initial sample to  $0.2 \times 10^{-3} \text{ g}$  of the sample treated with 15 pulses, indicating a significant improvement in the wear resistance of the Al-17.5Si alloy after HCPEB treatment. The relative wear resistance was enhanced by a factor of 6.5. The weight loss of the  $\text{Mg}_{67}\text{Zn}_{30}\text{Y}_3$  quasicrystal alloy sample was  $1.7 \times 10^{-3} \text{ g}$  before the HCPEB treatment, which was reduced to  $0.8 \times 10^{-3} \text{ g}$  after the 15-pulse treatment. Consequently, the relative wear resistance was improved by a factor of 2.1, which can be attributed to the formation of a supersaturated solid solution of  $\alpha(\text{Mg})$  and the grain refinement of the melted layer. Nanocrystallization induced by HCPEB surface treatment is known to contribute significantly to the improvement of wear

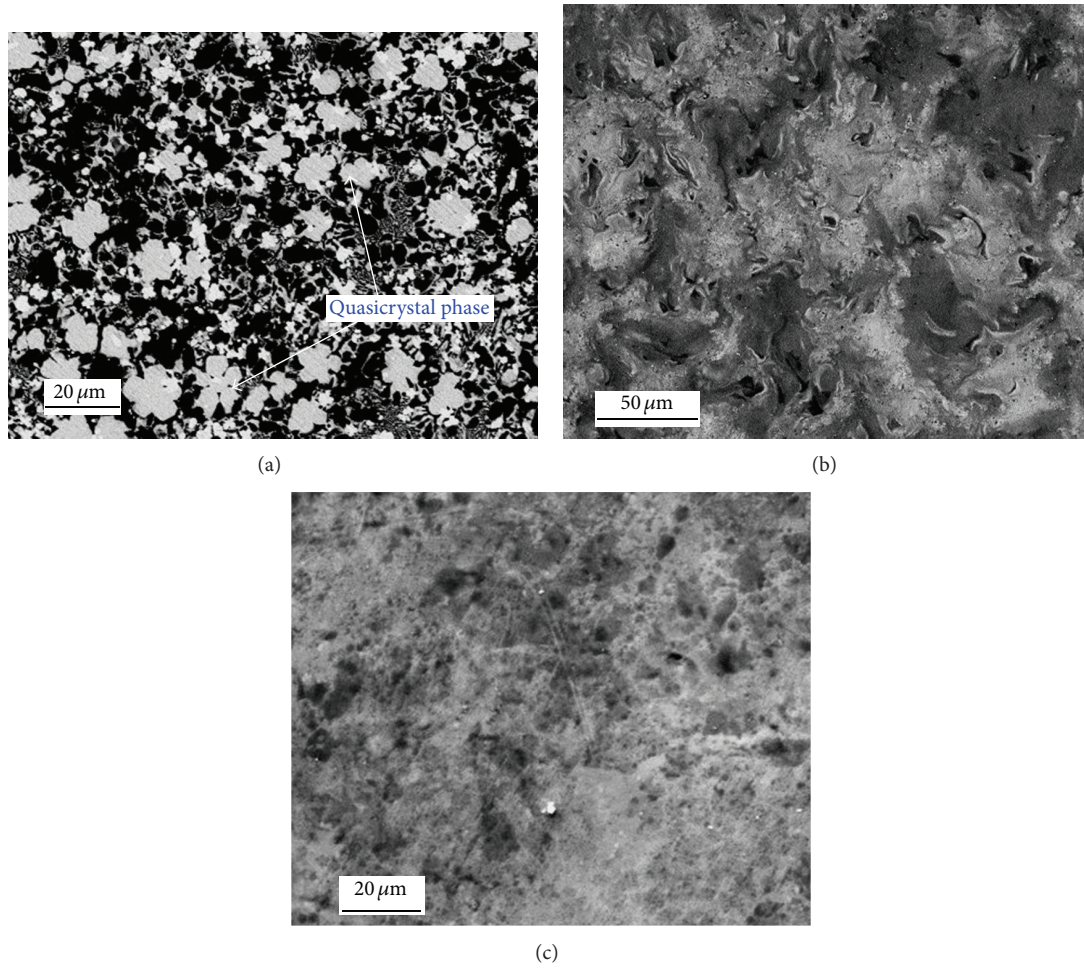


FIGURE 3: Surface SEM BSE images of  $Mg_{67}Zn_{30}Y_3$  quasicrystal alloy in initial state (a) and after HCPEB treatment for 2 pulses (b) and 15 pulses (c).

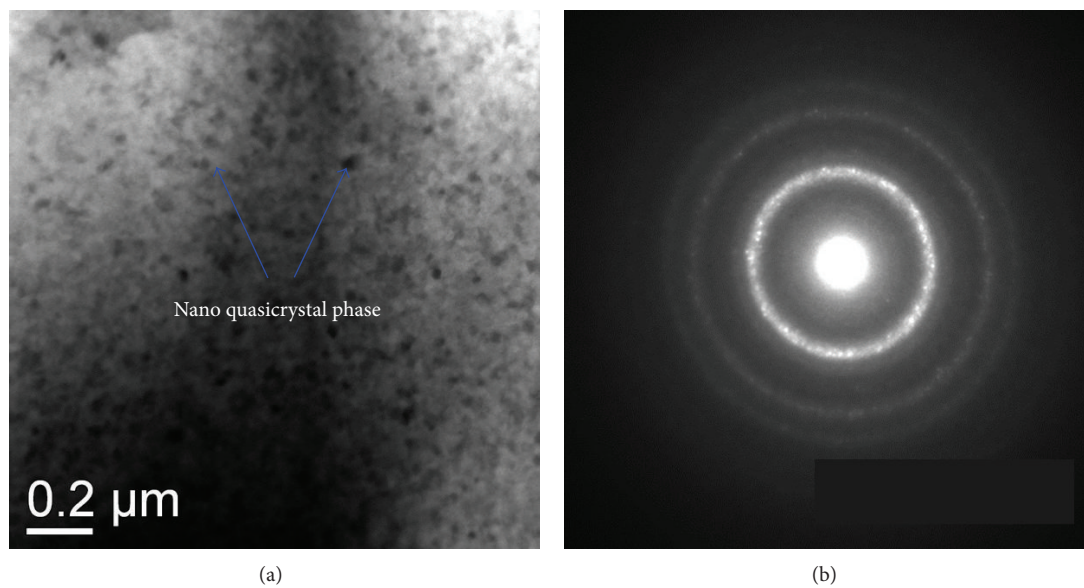


FIGURE 4: TEM bright field image of 10-pulse treated  $Mg_{67}Zn_{30}Y_3$  (a) and corresponding SAED pattern (b).

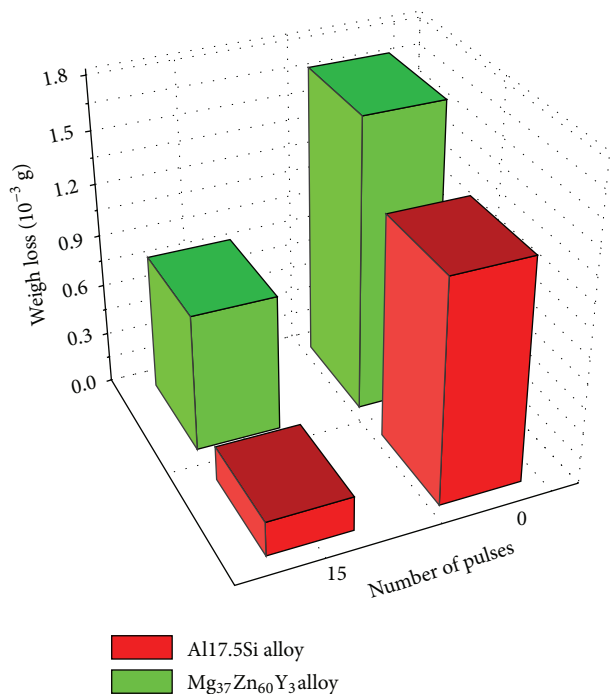


FIGURE 5: Weight loss of Al17.5Si and Mg<sub>37</sub>Zn<sub>60</sub>Y<sub>3</sub> alloys before and after HCPEB treatment.

resistance of Al-17.5Si and ZK60-1Y Mg<sub>67</sub>Zn<sub>30</sub>Y<sub>3</sub> quasicrystal alloys.

#### 4. Discussion

The nano primary Si phase in the hypereutectic Al-17.5Si alloy is formed during the rapid solidification of the HCPEB treatment. Therefore, several factors that affect the nucleation and the growth of the Si influence the formation of the nanostructure. Figure 2 presents the microstructure characteristics of the zone near the boundary between the Si-rich and Al-rich zones of the 100-pulse treated sample. The microstructures observed in Figure 2 suggest the following description of the HCPEB treatment process. First, in the heating and melting state, the Si element diffuses from the primary Si phase to the edge of the Si-rich zone; however, the Al element diffuses toward the opposite direction. Second, in the solidification state, the Si crystals nucleate from the supersaturated melted solution and grow into the undercooled melt of the environment. The Si crystals reject the Al until the local concentration is sufficient to nucleate the  $\alpha$ (Al) phase. The  $\alpha$ (Al) phase nucleates on the special crystal plane and surrounds the Si particles, thereby preventing the growth of the Si phase. With an increase in the number of pulses, the Si element continually diffuses from the coarse phase and forms a new nano-Si phase in the melted solution. Consequently, the size of the primary Si phase decreases, thereby forming an extremely fine nanodispersive Si phase after 100-pulsed treatment. Meanwhile, HCPEB irradiation exerts a similar effect on the refinement of the coarse petal-shaped quasicrystal phase (Mg<sub>3</sub>Zn<sub>6</sub>Y); after multiple-pulse

treatments, the size of the coarse quasicrystal phase reaches the 10 nm to 30 nm range by TEM analysis. Naturally, the fine primary Si phase and quasicrystal phase contributes to the enhanced tribological properties of hypereutectic Al17.5Si alloy and quasicrystal alloy Mg<sub>67</sub>Zn<sub>30</sub>Y<sub>3</sub>.

#### 5. Conclusions

This study demonstrates that the surface nanocrystallization of the primary Si phase in hypereutectic Al17.5Si alloy and quasicrystal phase (Mg<sub>3</sub>Zn<sub>6</sub>Y) in quasicrystal alloy (Mg<sub>67</sub>Zn<sub>30</sub>Y<sub>3</sub>) is induced by HCPEB irradiation. In both cases, nanograined primary phases are formed on the materials after a sufficient number of pulses. The results indicate a strong potential for surface nanocrystallization of the coarse primary phase in alloys treated by HCPEB, and the nanocrystallization surfaces of the two alloys exhibit very high wear resistance compared with that of initial samples. The mechanisms were identified to produce nanostructures from the melted liquid by taking advantage of the rapid thermal cycle and the diffusion of alloying elements, as well as the heterogeneous nucleation generated by the HCPEB process.

#### Acknowledgments

This study is supported by the Natural Science Foundation of Shenyang City (F12-277-1-55) and the Program for Excellent Talents in Liaoning Province (LJQ2012021). The authors gratefully acknowledge the help of Dr Yi Hao and Shiwei Li.

#### References

- [1] N. R. Tao, M. L. Sui, J. Lu, and K. Lua, "Surface nanocrystallization of iron induced by ultrasonic shot peening," *Nanostructured Materials*, vol. 11, no. 4, pp. 433–440, 1999.
- [2] K. Lu and J. Lu, "Surface nanocrystallization (SNC) of metallic materials—presentation of the concept behind a new approach," *Journal of Materials Science and Technology*, vol. 15, no. 3, pp. 193–197, 1999.
- [3] C. Suryanarayana, "Nanocrystalline materials," *International Materials Reviews*, vol. 40, no. 2, pp. 41–64, 1995.
- [4] B. Gao, S. Hao, J. Zou, W. Wu, G. Tu, and C. Dong, "Effect of high current pulsed electron beam treatment on surface microstructure and wear and corrosion resistance of an AZ91HP magnesium alloy," *Surface and Coatings Technology*, vol. 201, no. 14, pp. 6297–6303, 2007.
- [5] Y. Hao, B. Gao, G. F. Tu, S. W. Li, S. Z. Hao, and C. Dong, "Surface modification of Al-20Si alloy by high current pulsed electron beam," *Applied Surface Science*, vol. 257, no. 9, pp. 3913–3919, 2011.
- [6] J. X. Zou, K. M. Zhang, S. Z. Hao, C. Dong, and T. Grosdidier, "Mechanisms of hardening, wear and corrosion improvement of 316 L stainless steel by low energy high current pulsed electron beam surface treatment," *Thin Solid Films*, vol. 519, no. 4, pp. 1404–1415, 2010.
- [7] Y. Qin, C. Dong, Z. F. Song et al., "Deep modification of materials by thermal stress wave generated by irradiation of high-current pulsed electron beams," *Journal of Vacuum Science & Technology A*, vol. 23, pp. 430–435, 2009.

- [8] S. Hao, B. Gao, A. Wu et al., "Surface modification of steels and magnesium alloy by high current pulsed electron beam," *Nuclear Instruments and Methods in Physics Research B*, vol. 240, no. 3, pp. 646–652, 2005.
- [9] Q. F. Guan, H. Zou, G. T. Zou et al., "Surface nanostructure and amorphous state of a low carbon steel induced by high-current pulsed electron beam," *Surface and Coatings Technology*, vol. 196, no. 1–3, pp. 145–149, 2005.
- [10] Y. Hao, B. Gao, G. F. Tu, S. W. Li, C. Dong, and Z. G. Zhang, "Improved wear resistance of Al-15Si alloy with a high current pulsed electron beam treatment," *Nuclear Instruments and Methods in Physics Research B*, vol. 269, no. 13, pp. 1499–1505, 2011.
- [11] B. Gao, Y. Hao, G. F. Tu, and W. Y. Wu, "Study on nanostructures induced by high current pulsed electron beam treatment," *Journal of Nanomaterials*, vol. 2012, Article ID 480482, 5 pages, 2012.
- [12] K. M. Zhang, J. X. Zou, and T. Grosdidier, "Nanostructure formations and improvement in corrosion resistance of steels by means of pulsed electron beam surface treatment," *Journal of Nanomaterials*, vol. 2013, Article ID 78568, 8 pages, 2013.
- [13] A. P. Tsai, A. Niikura, A. Inoue, and T. Masumoto, "Stoichiometric icosahedral phase in the Zn-Mg-Y system," *Journal of Materials Research*, vol. 12, no. 6, pp. 1468–1471, 1997.
- [14] B. Gao, Y. Hao, G. F. Tu et al., "Surface modification of  $Mg_{67}-Zn_{30}-Y_3$  quasicrystal alloy by high current pulsed electron-beam," *Surface and Coatings Technology*. In press.